UNIVERSITY OF SOUTHAMPTON

FACULTY OF PHYSICAL SCIENCES AND ENGINEERING
Physics and Astronomy

Non-Linear Lensing in Optically-Pumped Semiconductor Lasers

by

Edward A. Shaw

Thesis for the degree of Doctor of Philosophy

June 2018

To Ruth, Tony and Claire

UNIVERSITY OF SOUTHAMPTON

ABSTRACT

FACULTY OF PHYSICAL SCIENCES AND ENGINEERING
Physics and Astronomy

Doctor of Philosophy

NON-LINEAR LENSING IN OPTICALLY-PUMPED SEMICONDUCTOR LASERS

by Edward A. Shaw

Optically pumped semiconductor lasers (OPSLs) are a versatile family of lasers offering wavelength flexibility, high beam quality and multi-Watt level output powers. SESAM modelocked OPSLs can produce near transform limited femtosecond pulses at Gigahertz repetition rates. The performance of modelocked OPSLs is limited by the speed of the response of the SESAM and its resistance to damage. This thesis explores the potential for SESAM-free modelocking of OPSLs through the utilisation of a non-linear lens in the semiconductor gain structure.

The thesis presents two strands of research: experimental and computational. The non-linear lens is measured using a reflection z-scan technique. A computational model of a modelocked OPSL is developed to explore the transient dynamics of lasing onset and to test the temporal stability of the modelocked pulse. This thesis demonstrates that understanding the nature of the non-linear lens unlocks the potential to explore the possibility of improving laser performance in modelocked OPSLs.

Contents

Declaration of Authorship

I, Edward A. Shaw , declare that the thesis entitled *Non-Linear Lensing in Optically-Pumped Semiconductor Lasers* and the work presented in the thesis are both my own, and have been generated by me as the result of my own original research. I confirm that:

- this work was done wholly or mainly while in candidature for a research degree at this University;
- where any part of this thesis has previously been submitted for a degree or any other qualification at this University or any other institution, this has been clearly stated;
- where I have consulted the published work of others, this is always clearly attributed;
- where I have quoted from the work of others, the source is always given. With the exception of such quotations, this thesis is entirely my own work;
- I have acknowledged all main sources of help;
- where the thesis is based on work done by myself jointly with others, I have made clear exactly what was done by others and what I have contributed myself;
- parts of this work have been published as: Shaw, E. *et. al.* Proc. SPIE (2015), Quarterman, A *et. al.* Proc. CLEO Europe (2015), Shaw, E. *et. al.* Proc. SPIE (2016) and Shaw, E. *et. al.* IEEE Photonics Technology Letters (2016).

Signed:...

Date:..

Acknowledgements

I would like to thank Anne Tropper for her wisdom, support and endless encouragement throughout my PhD. I thank Keith Wilcox for his alignment wizardry, for teaching me the value of intuition and for giving me the opportunity to study for a PhD.

I would like to thank Adrian Quarterman for introducing me to the wonderful world of z-scans and for accompanying me in the lab for our first measurements of the non-linear lens; Robin Head for his wise words and support; Andy Turnbull for his technical knowledge and programming expertise; and to Olly Morris, Theo Chen-Sverre and Jonothan Woods for our many incitefull and informative conversations in the office and in the lab.

Thanks to Alessia Pasquazi and Marco Peccianti for welcoming me as a guest in their lab and supporting me through my experimental work at the University of Sussex.

I would like to thank the technical team in the electrical and mechanical workshops for keeping our labs running. Special thanks to Mark Scully for introducing me to metal working and for being patient as I found my way, I will always use the skills I have learned. Special thanks also to Damon Grimsey who's CAD/CAM skills equipped my lab bench with the vital components necessary to make my experimental work successful.

Thanks to Sanja, Mark and Paul for their support and encouragement as I found my feet with teaching.

Most importantly I give thanks to my family to whom I dedicate this thesis, without your love and support none of this would have been possible.

Thank you all so much.

Chapter 1

Introduction

The last few decades have seen significant advances in laser technology. Whilst early lasers were limited by their constant power output, the development of modelocking, in which the intracavity conditions of the laser are engineered to favour pulsed operation, enabled the production of high peak powers and expanded the potential uses of the technology. modelocked ultrafast lasers have demonstrated their utility in numerous fields due to three main advantages: their short pulse duration, high peak power, and broad optical bandwidth. Pulsed lasers have found uses in biomedical imaging and treatment, micro-machining, and metrology. They are continuing to expand their scientific and technological applications. Within this category, optically pumped semiconductor lasers (OPSLs) are potentially advantageous over solid state lasers due to their ease of operating at very high repetition rates, a direct result of the short upper state lifetime of semiconductor gain.

OPSLs combine the wavelength flexibility of semiconductors with the high beam quality of an external cavity. They can be passively modelocked through the inclusion of a saturable absorber in the laser cavity; typically, a semiconductor saturable absorber mirror (SESAM). SESAM modelocked OPSLs are capable of producing sub 200 fs pulses at Gigahertz repetition rates. However, their performance is limited by the speed of response of the SESAM and its resistance to damage. This thesis seeks to establish whether a non-linear lens in the semiconductor gain structure could be utilised to improve the performance of SESAM modelocked OPSLs, or achieve modelocking without a SESAM in the cavity. The potential for higher power and shorter pulses would considerably expand the scientific and industrial applications of OPSLs.

The work in this thesis was motivated by reports of OPSLs that modelock without a saturable absorber in the cavity, so-called self-modelocked (SML) OPSLs. However, these reports have presented laser performance without explaining fully the physical mechanism by which the pulses are created. Significantly, these reports lack complete characterisation of the observed pulsation.

This thesis focuses on the presence of a non-linear lens in the semi-conductor gain structure. There are two reasons that could explain why a non-linear lens has not been observed in early research into SESAM modelocked OPSLs. Firstly, SESAM modelocking does not require a critically aligned cavity, which means that typical OPSL cavities are designed to be a long way from the edge of the stability limit. In a non-critical cavity, a non-linear lens has less impact on the intracavity beam and would be less likely to affect the laser dynamics. Secondly, developments in wafer processing over the last decade have led to significant increases in power from the gain chips. As a non-linear lens is a power-dependent phenomenon, the increased power makes this research possible in ways it was not before.

In this thesis, I present two parallel strands of research undertaken to investigate the nature of the non-linear lens: experimental and computational.

Experimentally, I measured the lensing effect in an OPSL gain structure in order to establish the potential perturbation of the intracavity laser mode. This technique was developed in three stages: the first two measured the same gain structure, and the third developed the technique further using a different gain structure. The first two experiments were limited by equipment: the laser used to probe the gain structure was not powerful enough to match the intracavity power of the OPSL without significant modifications to the setup. The third perfected the technique, but a mechanical failure meant that the final set of results was more a proof of principle rather than a definitive characterisation of the lens.

The computational side of the thesis recreated the model based on the published work of Sieber et al. The model was developed to simulate a full-cavity round trip of the laser. By doing so, it enabled us to investigate transient dynamics in the build up from noise that have been experimentally observed, both in modelocked OPSLs and other ultrafast lasers. The high-frequency resolution of this improved model enables it to be used to robustly test the temporal stability of an optical pulse within the cavity. The model has been normalised to facilitate large-scale exploration of parameter space. This development has the potential to influence future laser design, and identify avenues for the improvement of laser performance. Finally, the model has been adapted to show the potential for an intensity-dependent lens and a hard aperture to achieve SESAM-free modelocking.

While the combination of these two research strands has not yet provided definitive answers to the question of whether non-linear lensing can be utilised to improve laser performance, it has developed important tools that could yet provide those answers. The experiments conducted were not able to establish a cavity design that could achieve stable, self-starting modelocking without a SESAM in the cavity. However, the computational modelling was able to show the potential pulse-shortening effect of a non-linear lens, and point to how it might be used in combination with a saturable absorber to achieve high power pulses in modelocked OPSLs.

This thesis is organised into five chapters.

In chapter 2 I introduce the design of OPSL gain and absorber structures and describe characterisation techniques used to measure their macroscopic parameters. I outline the theory of cavity design for modelocked operation and present typical cavities used in SESAM modelocked OPSLs and those used in reports of SML-OPSLs.

In chapter 3 I report the first measurements of the non-linear lens in an OPSL gain structure probed at a wavelength on resonance with the quantum well emission of the gain structure.

In chapter 4, the reflection z-scan technique is developed to use a CMOS sensor to measure the change in beam size. This technique is used to explore the wavelength dependency of the non-linear lens in an OPSL gain structure.

In chapter 5, I introduce modelling of ML-OPSLs capable of exploring the effects of macroscopic laser parameters on modelocked pulse characteristics. This recreates the model published by Sieber et al, expands it to simulate a full-cavity round trip, normalises it, and adds a non-linear lensing effect. It demonstrates the potential to increase the power in a SESAM ML-OPSL by introducing a hard aperture into the cavity.

This thesis demonstrates that understanding the nature of the non-linear lens unlocks the potential to explore the possibility of improving laser performance in modelocked OPSLs. By utilising both experimentation and computational modelling, it is possible to provide a more structured approach to the development of these lasers and their future application.

Chapter 2

Optically-Pumped Semiconductor Lasers (OPSLs)

2.1 Introduction

Optically-Pumped Semiconductor Lasers (OPSLs) also known as Vertical-External-Cavity Surface-Emitting Lasers (VECSELs) or Semiconductor Disk Lasers (SDLs) combine the wavelength versatility of semiconductors with design flexibility and high beam quality from an external cavity. Modelocked (ML) OPSLs can provide near transform limited sub-picosecond pulses at Gigahertz repetition rates.

Optically pumping the semiconductor gain structure removes the need to compromise between optical quality and electrical impedance which is an inherent trade-off with electrically pumped semiconductor lasers. Fibre-coupled diode lasers provide low cost pump light with high electrical to optical conversion efficiency and are able to provide uniform excitation across a large mode area.

The external cavity enables high quality single mode operation with M^2 close to 1 [1, 2]. The external cavity provides the flexibility to include intracavity elements such as: etalons for wavelength stabilisation and tuning [3]; birefringent filters for polarisation control; non-linear crystals for intracavity frequency doubling [4]; and saturable-absorbers for modelocking [5, 6].

OPSLs have been demonstrated at wavelengths ranging from 440 nm [7] to 5 µm [8], using a variety of semiconductor materials. With the development of thermal management techniques, through wafer processing and the utilisation of diamond or silicon carbide heat spreaders, record output powers have been achieved. In modelocked operation, multi-Watt level output powers have been achieved with sub-picosecond pulse duration and gigahertz repetition rates [9, 10]. In continuous wave operation, powers of up to 20 W have been demonstrated in single mode operation [1] and 106 W in multimode operation [11].

Optically pumped semiconductor lasers can be modelocked through the inclusion of a semiconductor saturable absorber mirror (SESAM) within the cavity [5, 6]. SESAMs provide saturable absorption through the incorporation of quantum wells (QWs) [12] or quantum dots (QDs) within their design [13]. Modelocked OPSLs have also been demonstrated utilising graphene as an absorbing layer in a so-called GSAM [14]. A saturable absorber element has also been included in the gain chip enabling modelocking of a simple two-mirror cavity, giving rise to the modelocked-integrated external-cavity surface-emitting-laser (MIXSEL) [15].

In recent years there have been reports of modelocked OPSLs that do not have a saturable absorber element in the cavity [16, 17, 18, 19, 20, 21, 22, 23, 24]. The authors offer different explanations as to why the observed pulsation occurs, some suggest that non-linear lensing is responsible and others speculate that under-pumped QWs in the gain structure act as a saturable absorber.

Reports of self modelocking have provided the motivation for the work in this thesis. We seek to experimentally measure the non-linear lens in an OPSL gain structure and to explore the effect of the measured lens could have on a critical cavity.

2.2 Modelocking

Modelocking (ML) of lasers is a technique used to control the phases of a lasers cavity modes to create a pulsed output. Modelocking of lasers falls into two categories: active and passive modelocking. In actively modelocked lasers the cavity loss is controlled externally to the laser. Passive modelocking utilises non-linear behaviours inherent to the laser components to modulate the cavity loss. Passively modelocked lasers have the advantage of being able to operate much faster than actively modelocked laser, exceeding the speed limitations of electronic circuitry.

Passive modelocking can be divided into fast saturable absorber modelocking and slow saturable absorber modelocking.

In fast saturable absorber modelocking, the loss is related to the intensity profile of the pulse. An example of fast saturable absorber modelocking is Kerr lens modelocking (KLM) in which instantaneous changes in the refractive index of a non-linear material are used to induce loss [25]. KLM has produced pulses as short as a few cycles of the optical carrier wave [26, 27]. In a KLM laser, the cavity is designed so that the higher the intracavity power the smaller the beam diameter at a waist in the cavity. The beam is attenuated by closing an aperture or a slit to occlude the edge of the beam, a hard aperture. The loss within the cavity is power dependent, higher powered light is attenuated less by the aperture due to the reduction in beam diameter caused by the Kerr lens. Alternatively the pump spot can be used as a soft aperture, with smaller diameter, higher power beam experiencing more gain/less loss due to better mode-matching with the pump beam. A lower power intracavity beam experiences higher losses than higher power light. Cavities are most sensitive to non-linear lensing when they are at the edge of stability [28].

In all lasers the gain is saturable. Over the time scale of the pulse interacting with the gain medium, the stored energy is depleted and the gain applied to the pulse reduces. In slow saturable absorber modelocking, the absorption of the pulse is a saturable effect. Energy that is absorbed from the leading edge of the of the pulse saturates the loss.

The saturation energy of the absorber must be lower than that of the gain so that the energy dynamics in the cavity favour pulsed operation.

SESAMs provide a source of saturable absorption in the laser cavity, enabling self starting modelocked operation. In the early stages of operation, the power in the cavity builds up from spontaneous emission from the gain. Due to the random phase differences between the spectral components noise spikes occur. Modelocking starts when a noise spike is able to saturate the absorption and is attenuated less. As this noise spike grows in energy, it extracts more energy from the gain reducing the gain available for other noise within the cavity. As the noise spike grows into a pulse, noise within the cavity is suppressed due to saturation of the gain by the pulse.

In an OPSL, utilising a NL lens in the gain structure as a modelocking mechanism has the potential to be advantageous over modelocking with a SESAM. SESAMs are susceptible to damage in an OPSL cavity both because of the technical challenges involved in thermal management and because they are typically subjected to higher intracavity fluences compared to the gain chip. Modulation of the intracavity loss may also be faster utilising a non-linear lens.

Hybrid schemes for modelocking have been demonstrated in which SESAMs are used for initial pulse formation and to make the laser self starting, once the pulse has been formed a secondary pulse shaping mechanism takes over. An example of such a hybrid system is SESAM stabilised soliton modelocking in thin disk lasers [29]. It is possible for the SESAM to play a role in both to starting and stabilising the modelocked pulses.

To optimise the performance of the laser and to achieve the shortest pulses directly from the cavity it is necessary to control dispersion. In an ideal laser the output pulses would be transform limited, having no internal phase relation between the cavity modes. The phase delay of each optical component in the laser cavity either must be designed to be as close to zero as possible or such that the phase delay from each of the optical components combines to give a net phase delay for a round trip of the cavity that is close to zero. In some lasers, a dispersion controlling element may be added to the cavity in addition to the gain, absorber, output coupler and other cavity mirrors. Whilst OPSLs are low gain lasers, it is preferable to optimise the design of the individual components to minimise dispersion, avoiding the insertion loss of adding an additional component to control dispersion.

Multi-Watt level output powers have been achieved with SESAM modelocked OPSLs [30]. The highest peak power has been achieved with 400 fs pulses generated in a 1.67 GHz cavity emitting 3.3 W of average output power [9]. Higher pulse energy has been produced by another OPSL with a longer pulse duration of 682 fs in a 1.67 GHz cavity emitting 5.1 W of average output power [10]. The shortest pulses emitted directly from a fundamentally modelocked cavity are 107 fs pulses from a 5.1 GHz cavity with 3 mW of average output power [31]. Sub 100 fs pulses have been produced at 100 mW of average output power using compresion external to the laser cavity [32].

2.3 OPSL Gain Structure Design

OPSL gain structures are multilayer semiconductor structures often referred to as gain samples or gain chips. Gain structures are active mirrors providing high reflectivity to the laser mode as well as amplification through the incorporation of quantum wells (QWs) or quantum dots (QDs). A wide range of materials systems are used to cover the spectral range from 440 nm to 5000 nm [7, 8]. This chapter will discuss the design of OPSL gain structures for operation around 1 µm using indium gallium arsenide (InGaAs) QWs or QDs embedded in gallium arsenide (GaAs). This material system is capable of covering a wavelength range from ~950 nm to ~1100 nm.

Structures can vary greatly in the thickness, composition and number of layers and are tailored to the application the laser is being designed for. Gain structures for high powered continuous wave operation have different design characteristics to those designed for ultrafast modelocking. Structures are epitaxially grown by either molecular beam epitaxy (MBE), metal-organic vapour phase epitaxy (MOVPE) or metal-organic chemical vapour deposition (MOCVD) onto a GaAs substrate. The GaAs substrate has a high thermal impedance and can be limiting factor maximising output powers. The substrate can be removed through wet chemical etching before a gain chip is bonded to a CVD diamond or Silicon Dioxide heat spreader, a process referred to as flip-chip bonding [33].

Full details of the processing applied to gain chip described in section 2.3.5 can be found in the published work of Borgentun *et.al.* [34].

Gain structures consist of three main elements: a distributed Bragg reflector (DBR), an active region and a window layer.

2.3.1 Distributed Bragg Reflector (DBR)

The DBR consists of alternating high/low refractive index layers, each a quarter wavelength optical thickness, providing high reflectance for the intracavity beam. A typical DBR consists of 27.5 $\lambda/2$ pairs providing greater than 99 % reflectivity. For processed samples, the total number of DBR pairs can be reduced as the gold-indium solder used to bond the processed gain chip to the heat spreader provides sufficient reflectivity to compensate for the missing layers. OPSLs operating at around 1 µm typically use aluminium-gallium arsenide (AlGaAs) as the high index material and gallium arsenide (GaAs) for the low index material.

2.3.2 Active Region

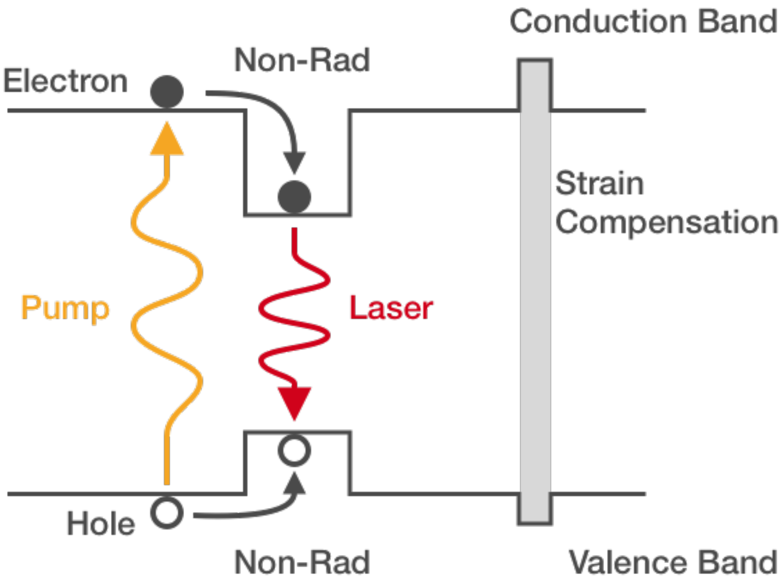

Figure 2.1: Schematic representation of the energy bands in a semiconductor quantum well (QW) (not to scale). Pump photons are absorbed in the bulk region between the QWs exciting an electron from the valence band to the conduction band. The excited electron leaves behind a hole which other electrons in the valence band can move into; this hole acts like a carrier. Electrons and holes are captured in the potential of the QW releasing the energy difference between the two levels non-radiatively. Carriers recombine in the QW releasing photons at the laser wavelength. Strain compensation layers are added to reduce the overall strain within the structure and reduce the chances of lattice dislocations.

Within bulk semiconductor material, quantum wells (QWs) or quantum dots (QDs) provide laser gain. The QW or QD material is GaAs doped with In which lowers the band-gap energy: a schematic of a QW is shown in fig. 2.1. Varying the indium percentage tunes the peak emission wavelength of the QW.

Pump photons are absorbed in the bulk region between the QWs, exciting an electron from the valence band to the conduction band. The excited electron leaves behind a hole which other electrons in the valence band can move into, this hole acts like a carrier. Electrons and holes are captured in the confining potential of the QW, releasing the energy corresponding to the difference between the two levels non-radiatively. Carriers recombine in the QW releasing photons at the laser wavelength.

The energy lost to the lattice as the carriers are captured by the QW is referred to as the quantum defect. Reducing the quantum defect increases the efficiency of the structure and reduces the heat deposited into the sample through pumping, however it also reduces the potential of the well. Carriers with lots of kinetic energy can escape from the well, a process colloquially referred to as boil-out. The rate of carriers escaping increases with temperature. At high pump powers, carriers escaping the QW leads to a process called thermal roll-over which causes lasing to stop.

Quantum wells are compressively strained due to lattice mismatching between GaAs and InGaAs. Phosphorus can be added to the bulk material for strain compensation, either as a uniform doping of the barriers or as distinct layers decreasing global strain of the lattice. Strain compensation reduces the chance of localised lattice dislocations which appear as dark lines in the gain structure which do not emit light. Adding phosphorus to GaAs increases the band gap energy and acts as a potential barrier, thus strain compensation layers should not be placed adjacent to the QWs as they would inhibit carrier capture.

The length of the active region is an integer multiple of $\lambda/2$, with QWs or QD layers positioned at the antinodes of the standing wave formed in the microcavity between the DBR and the window layer.

2.3.3 Carrier Confinement/ Window Layer

The window layer confines carriers within the active region and can be as simple as a single layer of a material with a higher band gap energy than the barrier material and thick enough to prevent carriers tunnelling from the active region to the front surface of the structure where they can recombine. A capping layer can be added to prevent oxidation of the front surface.

The thickness of the window layer controls the E-field intensity on the front of the gain chip and correspondingly the strength of the E-field that is coupled into the microcavity. The length of the microcavity, and the position of the quantum wells within it, changes the strength of the E-field on the quantum wells. The wavelength dependence of the average E-field on the QW acts as a spectral filter on the QW gain.

Additional layers can be added to the front surface of the gain structure to adjust the group delay dispersion. Extra semiconductor layers epitaxially grown on top of the window layer or dielectric materials can be added during post-growth processing.

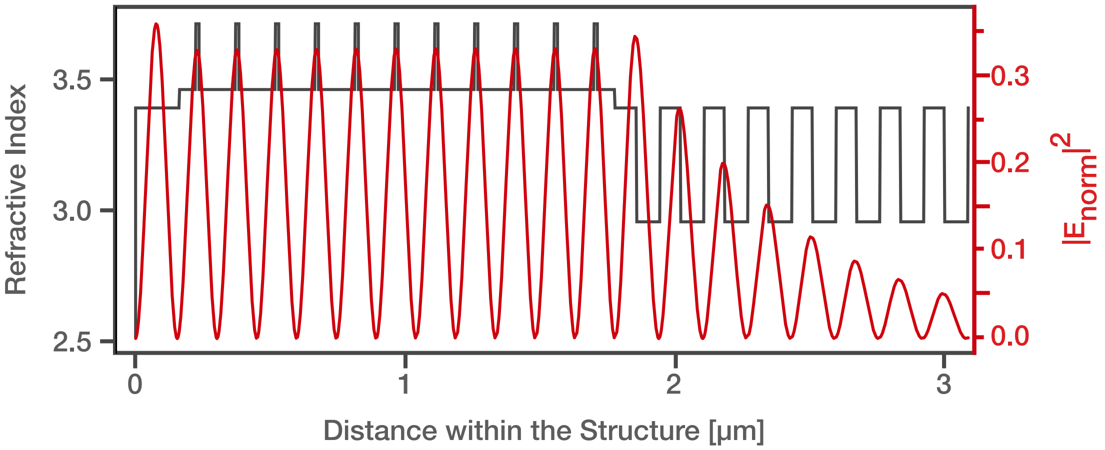

Figure 2.2: Schematic of an 11 quantum well RPG gain structure grown by Marburg University, Germany. In a modification to the RPG design, the window layer has been etched to a quarter wavelength thickness at a wavelength of 1035 nm to make the structure antiresonant. 11 InGaAs quantum wells (QW) are positioned with one QW per antinode of the E-Field standing wave. The material between the QWs is GaAsP, with a low phosphorous concentration to compensate for the compressive strain of the QWs. The sample is completed by an $InGaP_{0.5}$ window layer. The DBR consists of 22 pairs of AlAs/GaAs quarter wave layers with a centre wavelength of 1035 nm. The structure is flip-chip bonded onto a 300-micron thick CVD diamond. The diamond acts as a heat spreader which is mounted onto a Peltier controlled copper heat sink. The emitted centre wavelength ranged between 1025 nm and 1040 nm, when lasing in CW operation with a 20 degree heat sink temperature.

2.3.4 Periodic Gain (PG)

Periodic gain structures are designed to have a narrow bandwidth for high power CW operation. A resonant microcavity centres a peak of a Fabry-Perot etalon on the design wavelength, maximising spectral filtering of the gain. A single QW is placed at each anti-node of the standing wave formed inside the microcavity. A long microcavity makes room for more QWs to provide additional gain as well as enhancing the strength of the gain filtering from the etalon. Development of this design has led to record CW output powers [11].

The gain structure shown in fig. 2.2 is an RPG design on which additional wet chemical etching has been performed to thin the window layer to a thickness of $\lambda/4$. The resulting gain structure is anti-resonant. 11 InGaAs quantum wells (QW) are positioned with one QW per antinode of the E-Field standing wave. The material between the QWs is GaAsP, with a low phosphorous concentration to compensate for the compressive strain

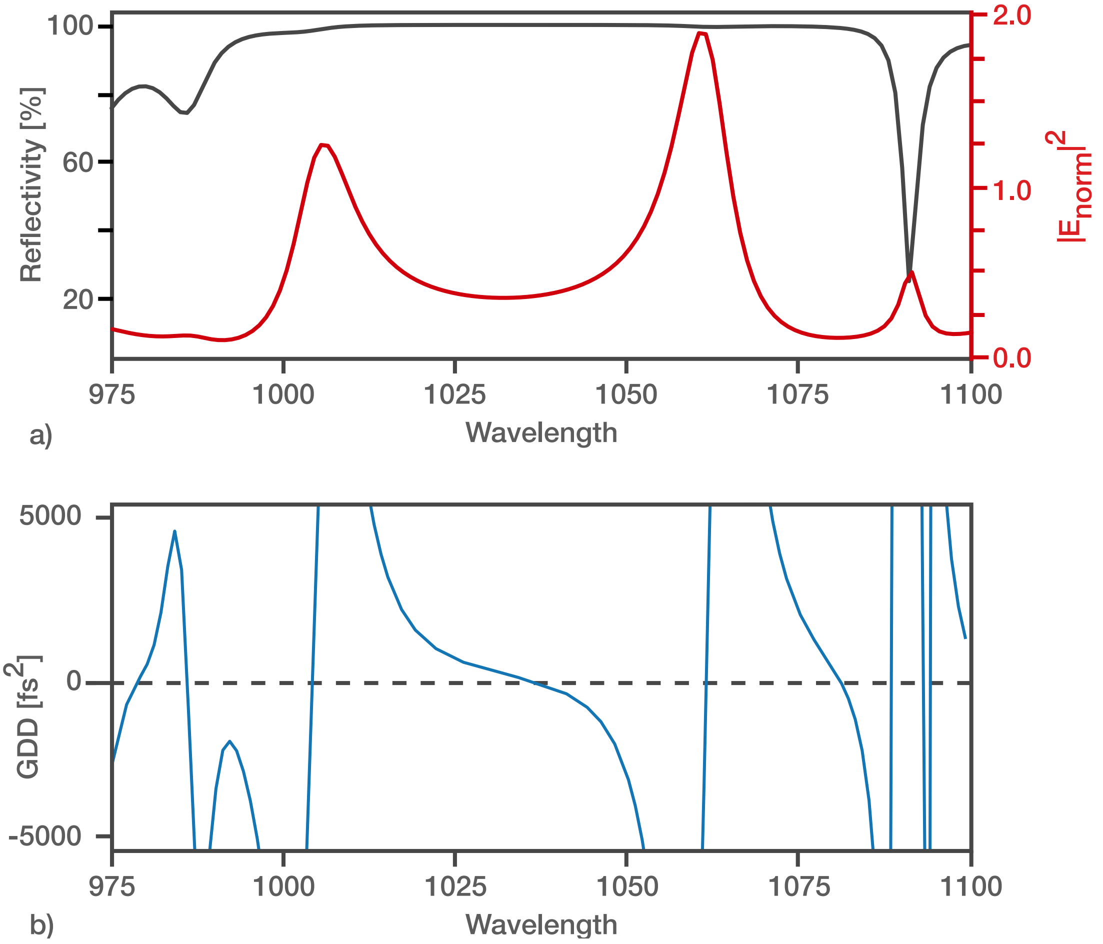

Figure 2.3: Theoretically calculated strength of (a) the E-field standing wave on the QWs and (b) the group delay dispersion (GDD) of the Marburg gain structure described in fig. 2.2

of the QWs. The sample is completed by an $InGaP_{0.5}$ window layer. The DBR consists of 22 pairs of AlAs/GaAs quarter wave layers with a centre wavelength of 1035 nm. The structure is flip-chip bonded onto a 300-micron thick CVD diamond. The diamond acts as a heat spreader which is mounted onto a Peltier controlled copper heat sink. The average strength of the E-field on the QWs and the group delay dispersion (GDD) can be theoretically calculated as a function of wavelength [35, 36]. The GDD and the average E-field on the QWs for the 11 QW Marburg gain structure is shown in fig. 2.3.

The emitted centre wavelength ranged between 1025 nm and 1040 nm, when lasing in CW operation with a 20 degree heat sink temperature.

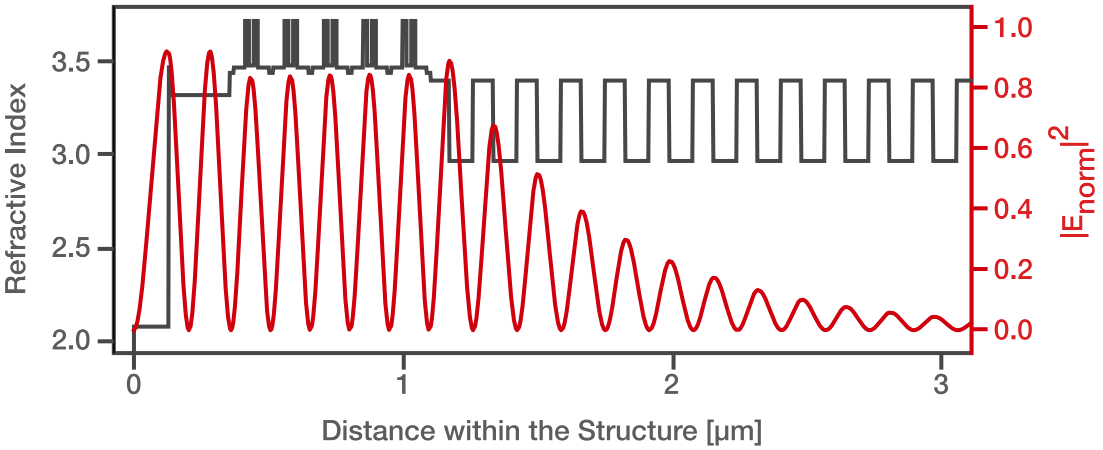

Figure 2.4: Schematic of a 5 double quantum well, short microcavity, anti-resonant gain structure grown by molecular beam epitaxy (MBE) Ulm University, Germany. The semiconductor base structure is resonant which is then coated with a single-layer dielectric coating to make the structure anti-resonant and to control the GDD of the sample. The dielectric material used on this sample was Aluminium Oxide (Al_2O_3).

2.3.5 Anti-Resonant Short-Micro-Cavity Double-Quantum-Well Gain

Anti-resonant short-microcavity double QW gain samples are designed to have a broad gain bandwidth for modelocked operation. Shortening the microcavity broadens the range of wavelengths which interact with the QWs, maximising the gain bandwidth. The short microcavity has correspondingly fewer antinodes of the intracavity standing wave at which to place QWs or QD layers. If a single QW were to be placed at each antinode in the same manner as the RPG structure, a shorter microcavity would have correspondingly lower gain. Placing two QWs at each antinode increases the gain of the sample. An example double QW structure is shown in fig. 2.4 with 5 pairs of QWs at each anti-node of the E-field standing wave in the micro cavity, grown at Ulm University in Germany.

An anti-resonant short microcavity also has a dispersion profile that is flat over a larger range of wavelengths. The breadth of the E-field interaction with the gain and the GDD profile favours the production of broader spectra and correspondingly shorter pulses when modelocked. The GDD and the average E-field on the QWs for the 5 double QW gain structure from Ulm University is shown in fig. 2.5.

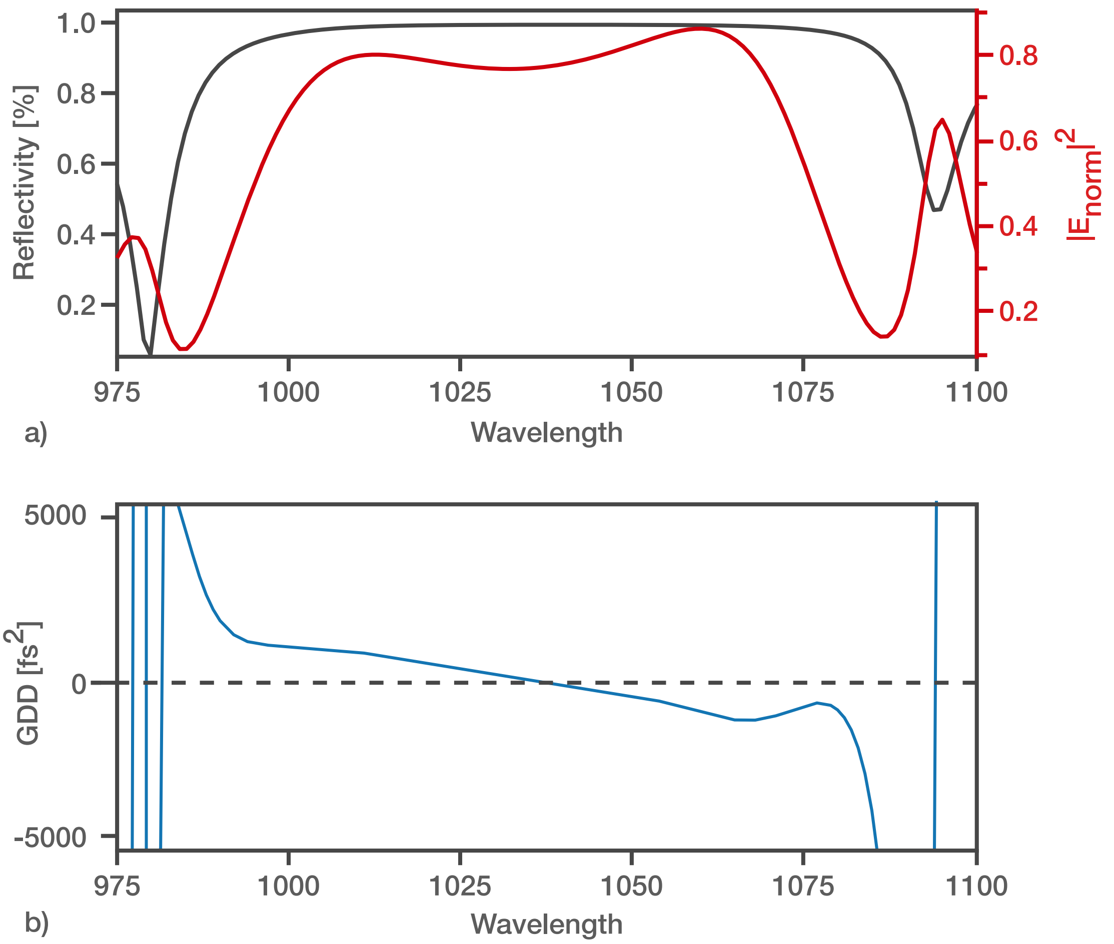

Figure 2.5: Theoretically calculated strength of (a) the E-field standing wave on the Quantum wells and (b) the group delay dispersion (GDD) of the 5 double quantum well gain structure described in fig. 2.4

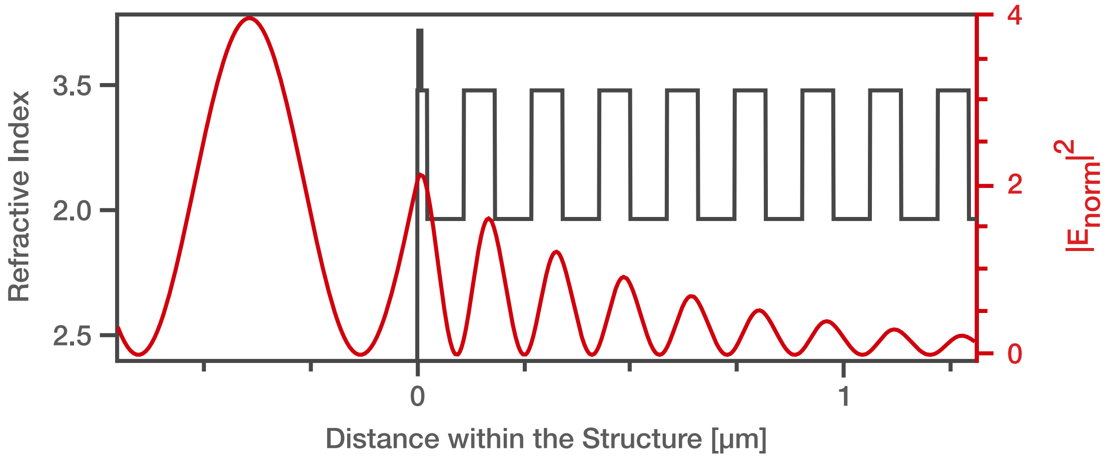

Figure 2.6: Schematic of a fast-surface recombination SESAM, grown by molecular beam epitaxy (MBE) at Cambridge University, UK.

2.4 Surface-Recombination SESAM

Semiconductor saturable absorber mirrors consist of a DBR to reflect the laser mode and an absorbing layer grown on top, as shown schematically in fig. 2.6. Surface-recombination SESAMs have a single quantum well (QW) a few nanometres beneath the front surface of the structure to act as the absorbing layer. The close proximity of the QW to the surface allows the carriers to tunnel to the surface to recombine. The thickness of the spacing layer between the quantum well and the first layer of the DBR determines the strength of the E-field on the QW and controls the modulation depth of the SESAM. For a single QW absorption layer, increasing the module depth reduces the saturation fluence.

The E-field on the QW and the GDD of the structure can be calculated for the SESAM in the same way as for a gain structure. The average E-field on the QW and the GDD of a fast surface recombination SESAM is shown in fig. 2.7.

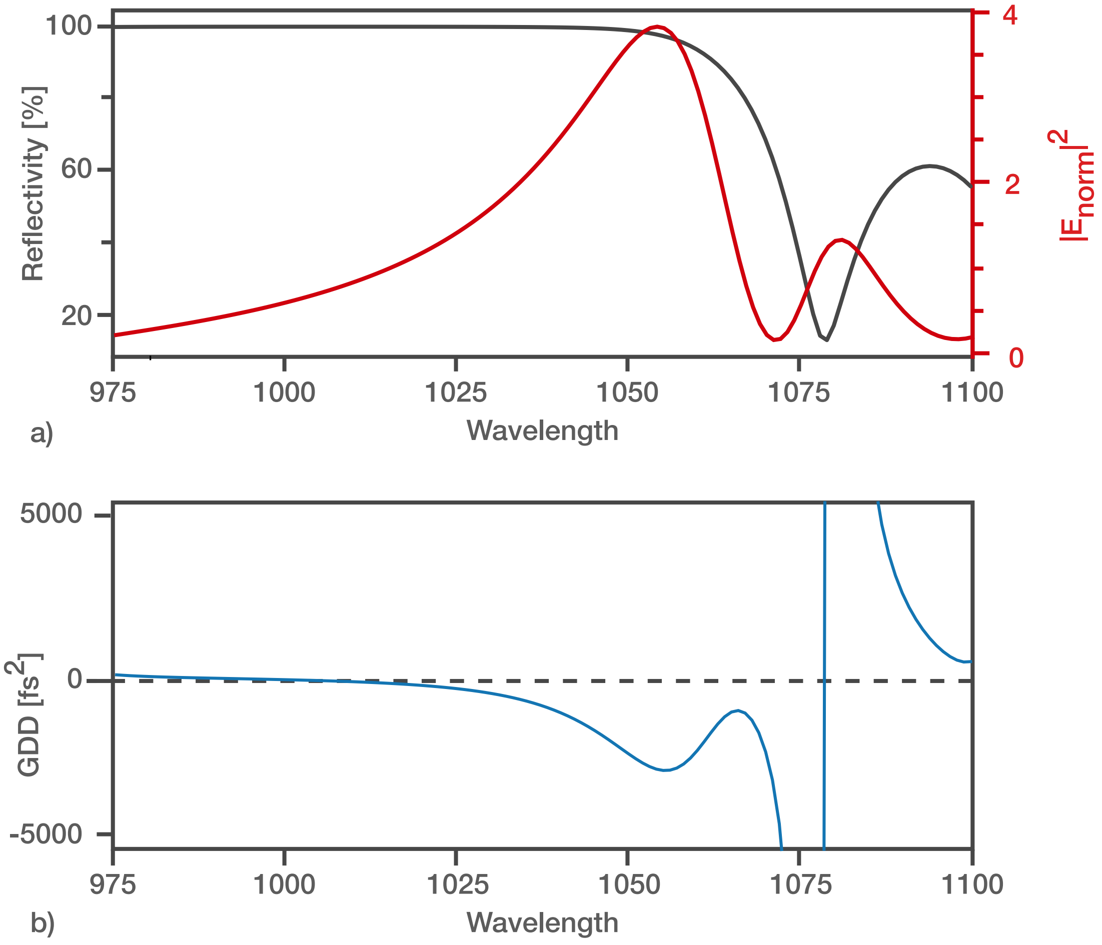

Figure 2.7: Theoretically calculated strength of (a) the E-field standing wave on the Quantum wells and (b) the group delay dispersion (GDD) a fast-surface recombination SESAM, grown by molecular beam epitaxy (MBE) at Cambridge University, UK. The structure of the SESAM is shown in fig. 2.6

2.5 Characterisation

Both gain and absorber structures can be characterised in terms of macroscopic parameters that can be experimentally measured. These parameters can be used to influence cavity design and in computational modelling of a ML-OPSL using the characterised component. Gain and absorber structures are characterised according to their small signal gain/loss, gain/loss saturation, temporal recovery and dispersion.

2.5.1 Reflectivity

Linear reflectivity measures the small signal gain/absorption of a semiconductor multilayer structure [37]. The probe light must be of sufficiently low power so that the gain or absorption is not saturated. Reflectivity measurements can either be made with a broadband light source or with a broadly wavelength-tunable CW laser. The system is calibrated using a broadband high-reflectivity laser mirror. Figure 2.8 shows linear reflectivity measurements of the 5 double-quantum-well anti-resonant gain structure described in fig. 2.4.

Reflectivity measurements can be used to determine the small signal gain and the gain bandwidth of gain samples, the modulation depth of the SESAM and the non-saturable losses of both components.

2.5.2 Dispersion

In addition to calculating the group delay dispersion of an optically reflective structure, the GDD can be measured using a white light interferometer [38]. The sample is illuminated with a broadband optical light source and the relative phase shift between wavelengths is measured. White light interferometers are commercially available and are able to measure group delay dispersion down to a resolution of $5\,\mathrm{fs}^2$.

The semiconductor multilayer structures can be altered by adjusting the thickness, number and composition of the layers. The GDD can be tuned by changing the design wavelength of the DBR and by adding additional semiconductor layers to the front surface

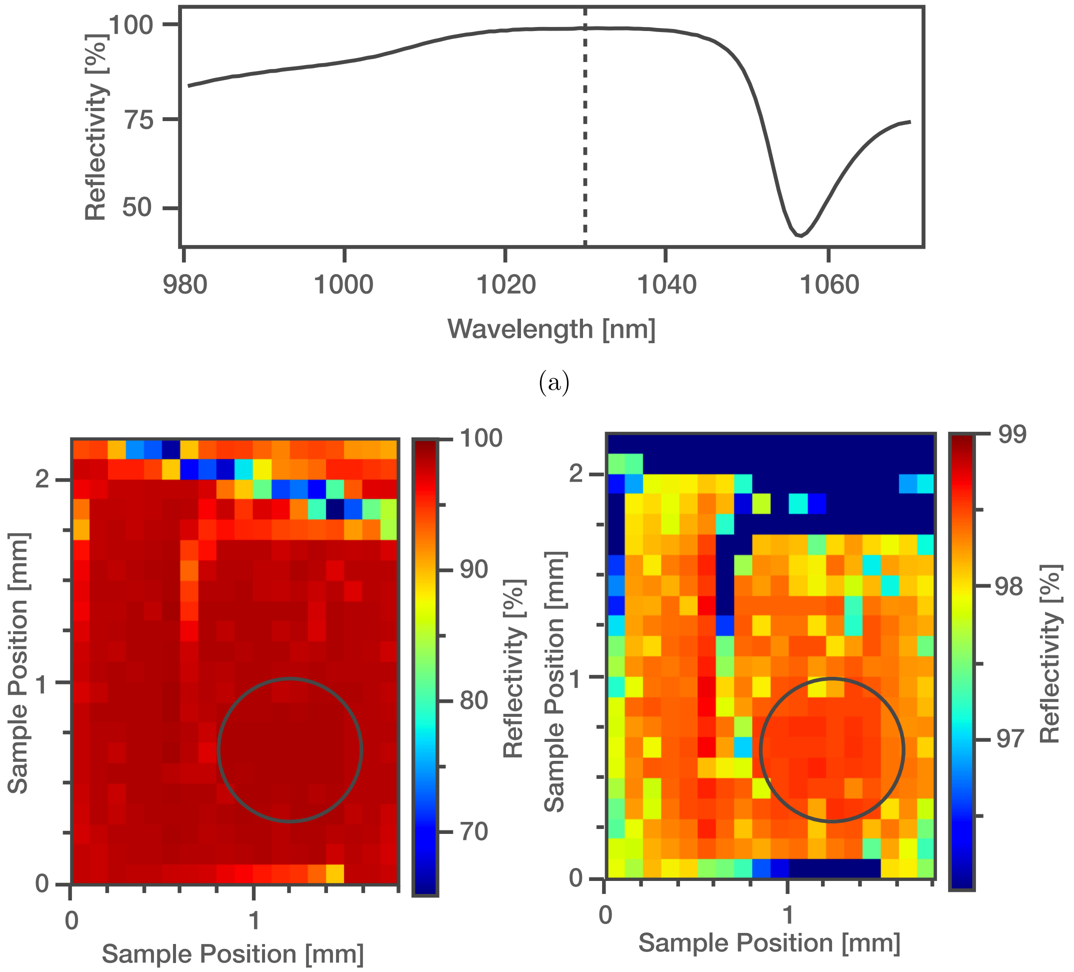

(a)

(b)

(c)

Figure 2.8: Reflectivity of the 5 double-quantum-well anti-resonant gain structure described in fig. 2.4. The sample was probed by a wavelength-tunable continuous-wave Ti:Sapphire laser. The setup is calibrated using a broadband high reflectivity laser mirror. The dip in reflectivity on the right-hand side of the graph marks the edge of the distributed Bragg reflector (DBR) reflection band. The reduction in reflectivity below 1010 nm is due to absorption in the quantum well (QW). The short wavelength edge of the DBR is not visible as it is outside of the tuning range of the probe laser. The reflectivity of a 1030 nm beam across the sample is plotted twice: subfigure b shows the entire reflectivity range with the colour scale spanning from 100 % down to the lowest measured reflectivity; in subfigure c, the range of values represented by the colour scale has been narrowed to create higher contrast. The circle marked on the sample maps represents the position of a 400 µm diameter pump spot used in later experiments with this chip and is the spot that is probed in subfigure a. The diagonal line of low reflectivity visible at the top of fig. 2.8b is a crack in the sample. The region above the crack has a lower measured reflectivity, clearly visible in fig. 2.8c due to the slight change in angle of the chip due to the crack.

of the sample. Dielectric dispersion controlling layers can be also be deposited onto the front of the sample. The GDD of the samples used in this thesis have not been measured directly.

2.5.3 Saturation Fluence

Saturation fluence is defined in terms of the pulse fluence at which the gain or absorption of the semiconductor multilayer structure is reduced to $1/e$ of it's initial value. Pulse fluence, $\mathrm{F} = \frac{\mathrm{E}_{\mathrm{pulse}}}{w}$, where $\mathrm{E}_{\mathrm{pulse}}$ is the pulse energy and w is the $1/e^2$ width of the laser beam.

Saturation fluences are measured by varying the fluence incident on the sample and measuring changes in reflectivity [39]. The same technique can be used to measure both the saturation of the gain in the gain structure and the saturation of the absorption in the SESAM. Due to the recovery of the gain/absorber, saturation fluences have a dependency on the duration of the probe pulse. OPSL gain samples have been measured to have saturation fluences in the range of $30\,\mu\mathrm{J/cm}^2$ and $80\,\mu\mathrm{J/cm}^2$ [40]. Saturation of SESAMs used in OPSLs has been measured to be $5\,\mu\mathrm{J/cm}^2$ [41].

2.5.4 Recovery

It has been demonstrated through computer simulation that the speed of absorber recovery plays a critical role in creating short pulses [42]. Measurements of the recovery dynamics of a SESAM using a pump-probe experiment can be fitted well with a double exponential with a constant weighting between the two components [43].

The two stage recovery is related to intraband and interband effects within the semiconductor, fig. 2.9. Redistribution of carriers within a band due to carrier-carrier scattering occurs on a time scale of about 100 fs [42]. Intraband recombination between the bands within a SESAM occurs on a time-scale of 1 ps to 10 ps. The speed of this recovery is heavily influenced by the availability of defect sites within the structure. In fast surface recombination SESAMs, the close proximity of the quantum well to the front of the

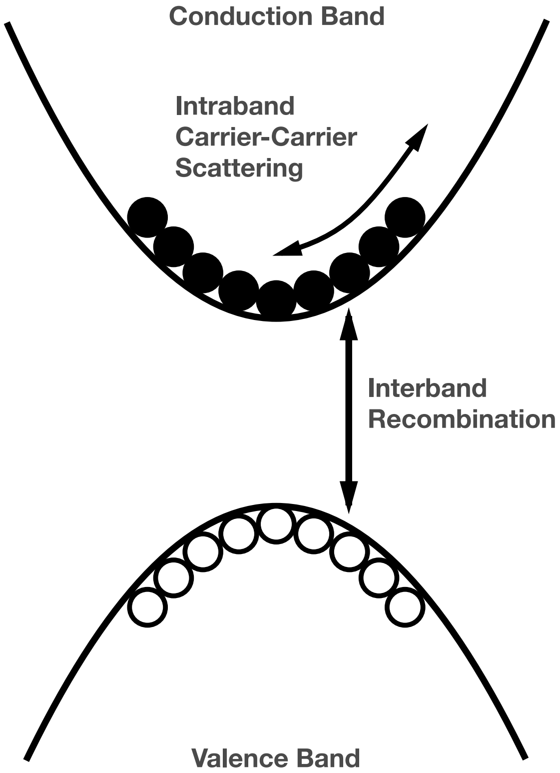

Figure 2.9: Parabolic band structure showing the physical mechanisms behind the two stage recovery in semiconductors. Carrier-carrier scattering is an intraband effect that redistributes carries within the band structure on a time scale of about 100 fs. The slow time component relates to interband recombination in SESAMs or absorption of pump light in gain structures.

structure allows carriers to tunnel to the surface where dangling arsenic bonds enable fast recovery.

We do not have accurate numbers for the fast recovery time of our fast surface recovery SESAMs. In pump probe recovery measurements, as τ_{fast} is reduced below the pulse duration of the probe pulse, the measured signal approaches the shape of an autocorrelation trace of the probe pulse. Measurements taken with a 1 ps pulse could not resolve the fast recovery time constant of a fast surface recombination SESAM, indicating that the fast recovery time constant is much less that 1 ps.

In gain samples, interband recovery takes the form of pump absorption into the barriers as well as carrier capture into the quantum wells. The rate of gain recovery from pumping is of the order of 1 ns and is dependant on the pump fluence and the internal structure of the microcavity. In situ probing of an OPSL gain structure has demonstrated that the OPSL gain structures exhibit a two-stage recovery process [44]. The in situ measurement technique directly measured the reflectivity of a gain structure as an optical element inside the cavity of a free-running OPSL. By using a probe laser with a lower repetition frequency than the OPSL being probed, an asynchronous optical probing (ASOPs) regime is achieved. There is currently no quantitative analysis from the experimental results to give a mathematical description of this recovery.

Microscopic modelling of OPSL gain structures also shows a two stage recovery. The incoming pulse burns a kinetic hole in the Fermi distribution of carriers within the gain. The size and shape of this hole depends on the pulse energy and the spectral profile of the pulse. The fast recovery is due to carrier-carrier scattering redistributing the carriers and refilling the hole. The slow component is the distribution recovering as pump light is absorbed.

2.6 Cavity Design

The cavity of an OPSL can be adapted to change the round trip time of the laser, the radii of the intracavity mode at the gain structure and at the saturable absorber and to include additional intracavity elements.

Due to the thickness of the semiconductor structures being very much less than the length of the cavity arms, OPSL cavities can be designed by using ray transfer matrices to calculate the profile of the intracavity beam.

The E-field within the cavity is defined as

$$E(x, y, z) = A(x, y, z) \exp(-ikz).$$

The amplitude of a fundamental mode Gaussian beam is given by

$$A(x, y, z) = \frac{A_0 w_0}{w} \exp\left[-\frac{x^2 + y^2}{w^2}\right],$$

where

$$w^2 = w_0^2 \left(1 + \frac{z^2}{z_0^2}\right).$$

z_0 is the Rayleigh range given by

$$z_0 = \frac{\pi w_0^2}{\lambda}.$$

The Rayleigh range is the distance over which the beam diverges so that the cross sectional area of the beam doubles. Due to the small thickness of the gain and absorber elements in an OPSL the Rayleigh range is not a critical cavity parameter. Gain and absorber components are considered insensitive to the divergence of the intracavity mode, they can be placed anywhere in a cavity and do not need to be placed at a beam waist.

For a given position within the cavity the fundamental profile of the intracavity beam is given by

$$A(x, y) = A_0 \exp\left[-\frac{(x - x_0)^2}{2w_x^2} - \frac{(y - y_0)^2}{2w_y^2}\right]. \tag{2.1}$$

Figure 2.10d shows the beam profile for an example beam as well as the variation of the beam's radius as a function of z about a focus.

2.6.1 Beam Propagation

Calculations for the beam size as it propagates and interacts with lenses and curved mirrors form the mathematical basis for cavity design and the analysis of non-linear lens measurements. Beam calculations in the form of ray transfer matrices and the Gaussian beam parameter are also utilised when modelling the effect of a non-linear lens in a OPSL in 5.

The complex beam parameter, $q(z)$, is used to describe the beam at a given point within the cavity and is a function of the radius of curvature of the beam front, R, and the radius of the beam, w:

$$\frac{1}{q(z)} = \frac{1}{\mathrm{R}(z)} - i\frac{\lambda}{\pi w^2(z)} \tag{2.2}$$

Propagation of a Gaussian beam between cavity elements is represented by

$$\begin{bmatrix} A & B \\ C & D \end{bmatrix} = \begin{bmatrix} 1 & d \\ 0 & 1 \end{bmatrix}$$

where d is the distance travelled in free space. Reflection from a curved mirror with radius of curvature R is treated as a thin lens, of focal length, $f = \frac{2}{\mathrm{R}}$, and is represented by the ABCD matrix

$$\begin{bmatrix} A & B \\ C & D \end{bmatrix} = \begin{bmatrix} 1 & 0 \\ -\frac{1}{f} & 1 \end{bmatrix}.$$

The Gaussian beam is propagated through the cavity using the equation

$$q' = \frac{Aq + B}{Cq + D}, \tag{2.3}$$

where q' is the new complex beam parameter and A, B, C and D are the matrix elements of the combined ABCD matrix representing the subsection of the cavity traversed by the beam.

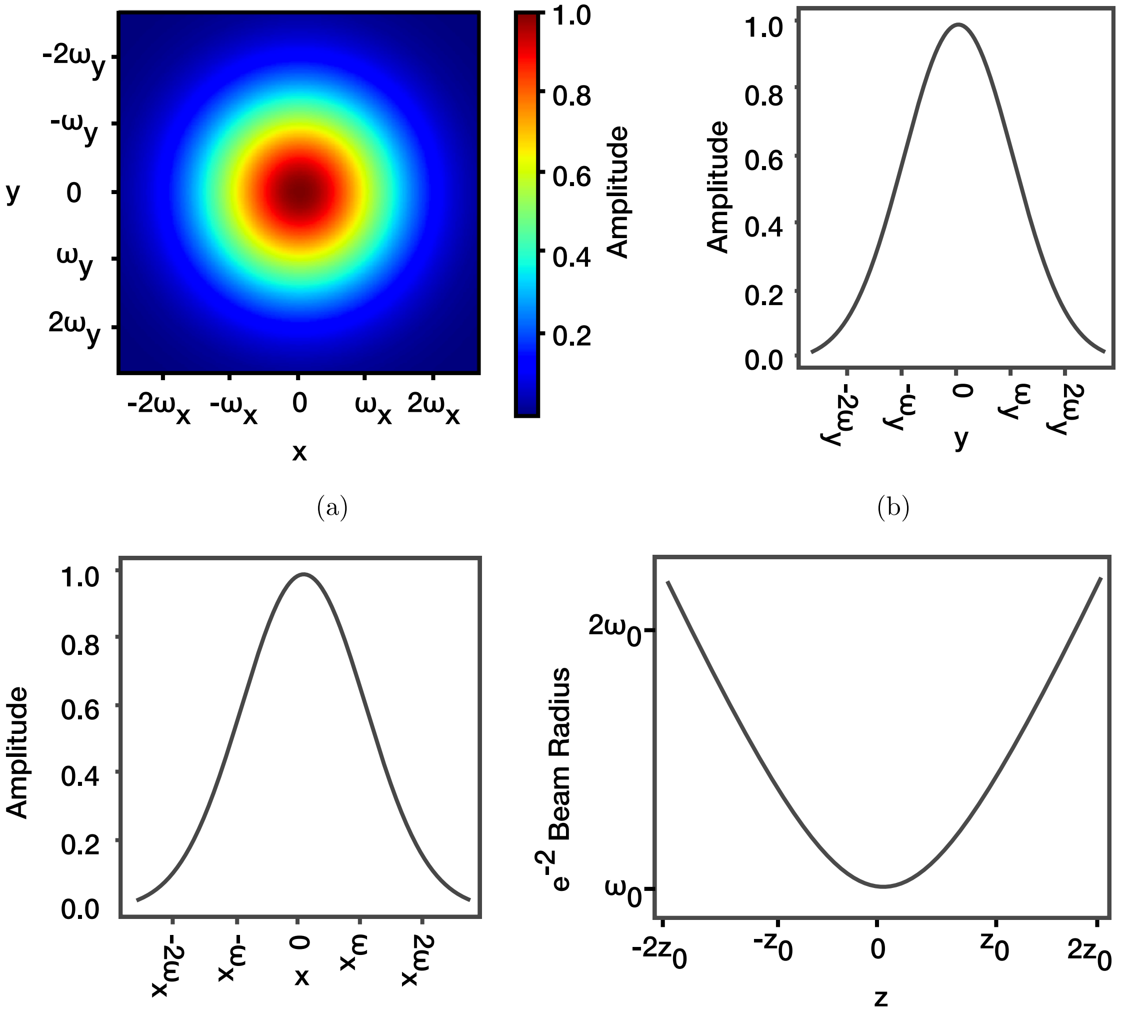

(a) (b)

(c) (d)

Figure 2.10: a) The amplitude profile of a TEM_{00} beam in the xy plane at a position z. b) Profile of the Gaussian beam along the x-axis. c) Profile of the Gaussian beam along the y-axis. d) Propagation of a Gaussian TEM_{00} beam along the z-axis through a focus at z= 0. Beam radius, $\omega(\mathrm{z})$, as a function of the axial propagation distance z about a focus at z= 0. Beam radius at the focus, $\omega(0) = \omega_0$.

To calculate the intracavity mode of a laser, the ABCD matrices representing a full cavity round trip are multiplied together. A cavity is stable if

$$-1 \leq \frac{\mathrm{A}+\mathrm{D}}{2} \leq 1, \tag{2.4}$$

where A and D are matrix elements from the ABCD matrix representing a single cavity round trip.

The Rayleigh range is given by

$$z_0 = \sqrt{\frac{-\mathrm{B}}{\mathrm{C}}}. \tag{2.5}$$

2.6.2 OPSL Cavity Geometries

When designing an OPSL cavity, the cavity length and the area of the intracavity mode on the gain chip and the SESAM must be optimised. Changing the length of the cavity adjusts the recovery time of the gain and the absorption between interactions with the pulse. If the cavity is too long the laser will become susceptible to multi-pulsing instabilities. The saturation of the gain and the absorption are measured in terms of a saturation fluence for each of the cavity elements. Changing the radius of the intracavity beam at the gain sample and the SESAM changes the relative saturation energies between the two semiconductor chips. The saturation energies for the gain and absorber can be finely tuned by varying the ratio of the radii of the intracavity mode at the gain and the absorber.

Two cavity geometries that are commonly used when designing modelocked OPSLs are the V-Cavity and the Z-cavity, named after their respective shapes. The V-cavity, shown in fig. 2.11, is a hemispherical cavity formed between a curved output coupler and a flat cavity mirror or a SESAM. The gain chip acts as a flat intracavity fold mirror. The ratio between the radii at the gain and at the SESAM depends on the distance between the two cavity elements, the cavity length and the radius of curvature of the output coupler. V-cavities are simpler than Z-cavities and are correspondingly easier to align.

The Z-cavity, shown in fig. 2.12, is a three mirror cavity with the gain acting as an additional flat fold mirror. The Z-cavity is more complicated than the V-cavity, having more cavity parameters that can be adjusted, which enables the area ratio to be adjusted over a greater range. Whilst V-cavities would typically have ratios between 1.5:1 and 4:1, Z-cavities can easily achieve area ratios above 10:1 and as low as 1:1.

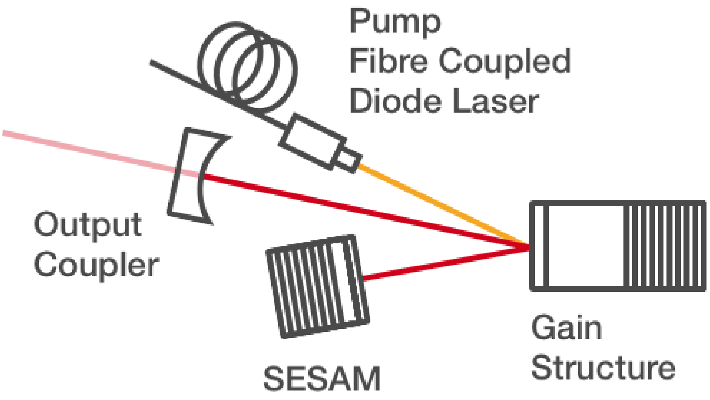

Figure 2.11: Schematic of a so-called V-cavity. This is a hemispherical cavity formed between a curved output coupler mirror and the SESAM. The gain structure is a flat fold mirror within the cavity. The area ratio between cavity mode at the SESAM and the gain structure can be adjusted by changing the position of the gain within the cavity as well as changing the overall cavity length and the radius of curvature of the fold mirror.

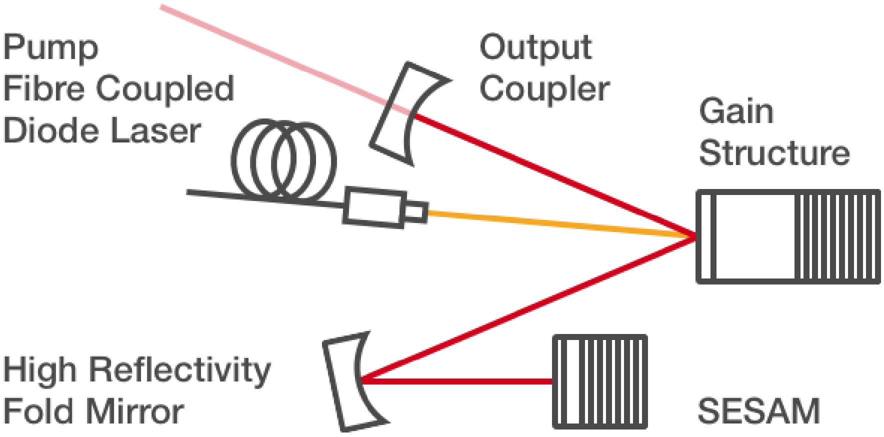

Figure 2.12: Schematic of a so-called Z-cavity. This cavity is like the V-cavity but with the addition of a curved fold mirror between the gain chip and the SESAM. This provides access to much larger range of area ratios. The area ratio can be adjusted by changing the relative lengths of the three cavity arms and the radii of curvature of the output coupler and the fold mirror.

2.7 Conclusion

In this chapter I have introduced the main principals behind the design of semiconductor multilayer structures for use in OPSLs. The mathematical descriptions for the propagation of Gaussian beams introduced here is utilised both in the analysis of non-linear lensing measurements in chapters 3 and 4 and in the computational modelling of OPSLs in chapter 5. The characterisation techniques define the macroscopic laser parameters that form the basis of the computational model in chapter 5. Cavity design is further considered in terms of the relative susceptibility of V-cavities and Z-cavities to a non-linear lens in section 5.5.

Chapter 3

Non-Linear Lensing in an OPSL Gain Structure

3.1 Introduction

Intensity induced changes in the refractive index, n, of an optical material can play an important role in the operation of ultrafast lasers. The dielectric polarisation, $P(t)$, of a material responds to the electric field, $E(t)$, by

$$P_j(t) = \epsilon_0 \left(\chi^{(1)}_{jk} E_k(t) + \chi^{(2)}_{jkl} E_k(t) E_l(t) + \chi^{(3)}_{jklm} E_k(t) E_l(t) E_m(t) + \dots \right). \tag{3.1}$$

ϵ_0 is the permittivity of free space, coefficients $\chi^{(n)}$ are the n-th order susceptibilities of the material and referred to as the coefficients of the n-th order non-linearity.

Gallium arsenide (GaAs) has a $\bar{4}3$m symmetry [45]. The GaAs substrates, upon which semiconductor multilayer structures are grown, are cut with (001) planes exposed. Normally incident light on (001) GaAs can only produce a $\chi^{(2)}$ polarisation vector oriented normal to the surface that does not effect the incident light.

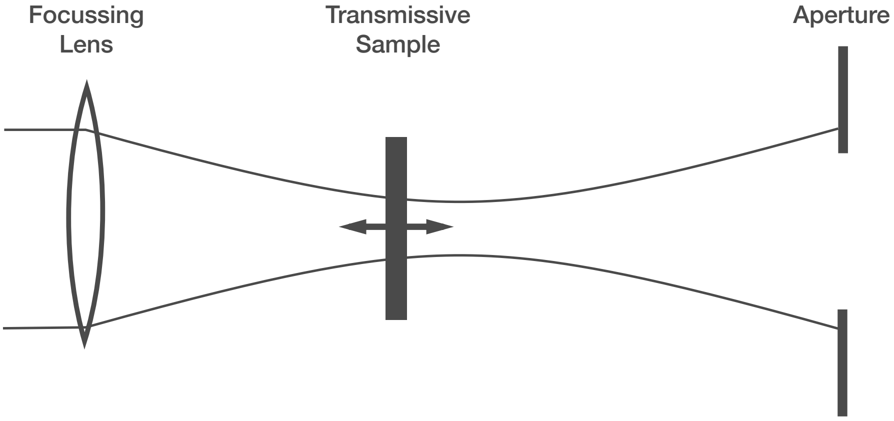

Figure 3.1: A schematic representation of the setup for a z-scan measurement of a transmissive sample. The sample is translated along the axis of a focussing Gaussian beam, termed the z axis. The transmission through a far field aperture is measured as a function of the sample position, z, to detect non-linear lensing in the sample.

When semiconductor multilayer structures grown on (001) GaAs substrates are illuminated with normally incident light, their refractive index can be written as

$$\mathrm{n} = \mathrm{n}_0 + \mathrm{n}_2\mathrm{I} + \ldots \tag{3.2}$$

where n_0 is the linear component of the refractive index and n_2 is a non-linear component of the refractive index which scales with the intensity of the incident light. We assume that even for small angles of incidence the contribution of $\chi^{(2)}$ effects is negligible. The value of n_2 in a dielectric can be positive or negative such that an incident Gaussian beam induces a converging or a diverging lens respectively.

Kerr lens modelocking (KLM) utilises the non-linear refractive index (n_2) of a material to achieve passive modelocking. In titanium sapphire lasers this effect has been used to produce pulses as short as a few cycles of the optical carrier wave [26, 27].

3.2 Z-Scan Measurements of Optical Non-Linearities

The value of n_2 in a dielectric material can be measured using a technique referred to as a z-scan [46], shown schematically in fig. 3.1. A transmissive sample is translated along the axis of propagation of a focussed Gaussian beam, termed the z-axis. Changes in intensity on the sample, due to the varying beam size, induce lensing of variable strength. The beam radius, $\omega_d(z)$, is measured at a distance, d, from the focus as a function of the position of the sample, z. Knowing the wavelength, λ and the focussed spot size, ω_0, of the input beam and the change in beam size at the detection plane, $\Delta\omega_d(z)$, the strength of the lens can be determined as a function of the z position of the sample.

A z-scan measurement can be used to detect intensity dependant changes in both the absorption and the refraction of a sample. Measuring the power of the beam transmitted through the sample, non-linear absorption can be measured. Measuring the full power of the beam is referred to as an open scan. Closing an aperture on the beam and measuring the transmitted power can be used to determine the non-linear refractive index of the sample. Measuring the power transmitted through an aperture is referred to as a closed scan. For samples that exhibit both non-linear absorption and non-linear refraction both open and closed scans are required to isolate the value of non-linear refractive index.

Figure 3.2 shows simulated z-scan data for a negative Kerr lens in a thin sample. Figure 3.2 a) shows the variation in the beam diameter incident an the sample as a function of the sample position, z. Figure 3.2 b) shows the corresponding change in the beam size at a distance, d, from the focus of the probe beam. Figure 3.2 c) shows the normalised transmission through an aperture place at a distance d for which the nominal transmission is 50 % when no lens is present.

For small lenses and where the sample thickness is very much less than the Rayleigh range of the probe beam the optical thickness of the sample can be neglected. In this thin sample approximation the lens is modelled as a parabolic phase mask. For thicker samples it is necessary to model the beam propagation through the distributed lens in the sample and not to rely on the paraxial approximation which breaks down for large lenses [47]. Z-scan measurements have been used to determine the Kerr non-linearity of sapphire crystal which is a common gain material used in KLM lasers [48].

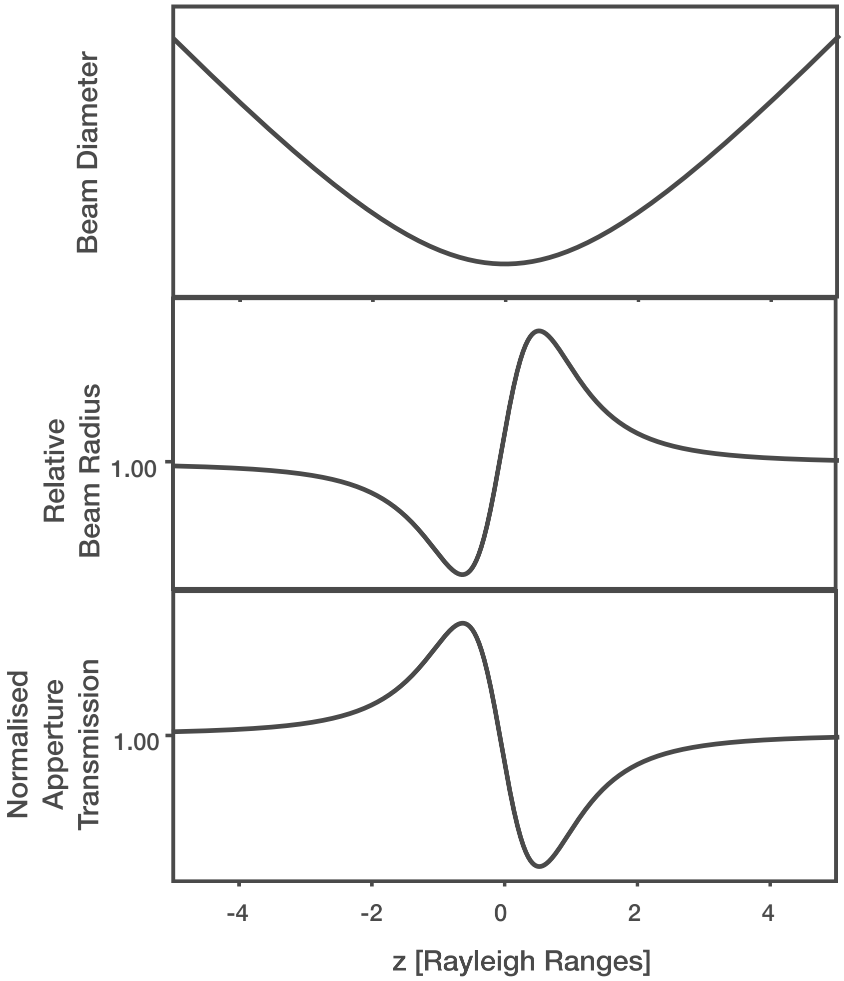

Figure 3.2: Simulated z-scan data showing the incident beam diameter as a function of the sample position z, the change in beam size at an aperture distance, d, from the focus of the probe beam and the transmission through an aperture that would transmit 50 % of the light if no lens was present in the sample.

3.3 Kerr Non-Linearity in Semiconductor Multilayer Structures

The non-linear response of semiconductors is highly dependent on the photon energy of the incident light as compared to the band gap energy of the semiconductor [49]. There are many different physical mechanisms that could affect lensing in the gain chip, including carrier effects and thermal effects, the strength of which are not well known and may occur on different time scales [50, 51]. Optical pulses which can vary in centre frequency, optical bandwidth, duration and energy may induce lenses of variable strength despite having the same peak intensity. The large variation in composition, thickness and number of layers makes modelling the non-linear response challenging.

The relative contribution to the non-linear lens from QWs and barriers is not well understood. The E-field standing wave formed by the microcavity (section 2.3.4) varies with wavelength, changing relative interaction between the barrier material and the quantum wells. The depth of penetration of the intracavity beam into the DBR also changes with wavelength.

Due to these wavelength dependent factors, when measuring the non-linear response of an OPSL gain structure one cannot determine a coefficient of non-linear refractive index of the material. Instead we seek to determine the effective non-linearity of the structure combined with its length, $n_2 l$ with units of $m^3\,W^{-1}$ which would be expected to be a function both of the probe pulse parameters as well as of the structure design parameters.

The value of n_2 in bulk GaAs has been measured to be $3 \times 10^{-13}\,cm^2\,W^{-1}$ at a wavelength of 1060 nm [52]. The non-linear refractive index of sapphire is three orders of magnitude lower than that of GaAs at $\sim 3 \times 10^{-16}\,cm^2\,W^{-1}$ at 1060 nm. Typical thickness of a sapphire crystal used as a laser component is measured in centimetres whereas a semiconductor MQW gain structure has a thickness of a few microns. For the same optical intensity the effective lens in a sample of GaAs of thickness comparable to an OPSL gain structure would be an order of magnitude smaller. Measuring the lens in a OPSL gain structure requires a sensitive measurement technique.

The first z-scan characterisation of an OPSL gain structure detected a non-linear lens that was dependant on incident pump power, changing from a negative lens in the unpumped gain structure and moving through zero to a positive lens with increasing pump power [53]. The wavelength of the probe laser was 1064 nm, outside the 1025 nm to 1040 nm range over which the gain chip was observed to lase. The pulse duration of the probe laser was 10 ps, more than an order of magnitude longer than the typical pulse duration of a femtosecond ML-OPSL. The value of n_2 measured in the unpumped sample was $(-1.5 \pm 0.2)\,cm^2\,W^{-1}$. When the gain structure was pumped the measured value of n_2 changed with pump intensity becoming positive at pump intensities above $50\,\mathrm{kW\,cm^{-2}}$.

3.4 Moving Lens Z-Scan Measurement of a Resonantly Excited Gain Chip

Initial experiments to measure the lens in an OPSL gain structure were made using an adapted z-scan technique, accommodating the reflecting nature of the multilayer semiconductor chip and using the apparatus available at the time. Rather than translating the sample along the axis of the probe beam, the focussing lens was translated with respect to the sample. The angle at which the probe beam was incident upon the sample was sufficient to prevent the reflected beam from being occluded by the mount holding the focussing lens.

The OPSL gain structure being tested was the same sample measured in reference 53, described in detail in section 2.3.4. The probe laser used in these experiments was an ytterbium:glass laser producing 230 fs FWHM pulses with a Gaussian temporal profile at 63.4 MHz and with a centre wavelength of 1035 nm. The available average power was 130 mW at the sample. The M^2 value was less than 1.1 on both axes. The probe laser operates at a wavelength at which the gain chip had been observed to lase and at a pulse duration at which OPSLs can operate.

The pulse energy is 2 nJ at an average power of 130 mW. We compare this to a 1 W, 1 GHz, 1 ps, laser with 1 % output coupling as a rough guide to the intracavity pulse fluence on the gain chip. These comparative values were chosen to match representative performance for high power OPSLs. Average powers of 1 W are routinely achievable with processed gain samples. For high power performance the repetition rate is lowered, 1 GHz is approximately the limit at which OPSLs reliably operate in a fundamental modelocking regime, free from multi pulsing instabilities. OPSL pulses in the region of 1 ps duration have the highest pulse energies. The intracavity pulse energy of such a laser would be 100 nJ. A common radius of the intracavity mode at the gain chip is 200 µm. For a 100 nJ pulse energy, this corresponds to an intracavity pulse fluence of $80\,\mu\mathrm{J\,cm^{-2}}$. To achieve the same pulse fluences with a 2 nJ pulse we require a spot size of 28 µm.

Initial attempts to measure a non-linear lens in a gain chip were not successful in measuring a lens. Shorter and shorter focal length lenses were used to reduce the size of the focussed spot and increase the peak fluence of the probe beam. To detect lensing in the sample an 8 mm focal length moulded glass aspheric lens (Thorlabs A240TM-B), producing a focussed spot of diameter 5 µm, was needed.

The high divergence of the beam required the angle of incidence to be 40° or greater to prevent the reflected beam being occluded by the lens mount. In an OPSL cavity the fold angle on the gain is minimised to optimise the interaction with a circular pump spot. An angle of incidence of 40° is not representative of an OPSL cavity. Instead the set up was aligned at normal incidence with the reflected beam coupled back through the focussing lens, as shown in fig. 3.3. With this alignment the reflected beam was collimated when the sample was at the focus, position $z = 0$.

A Faraday isolator was used to prevent the reflected beam being coupled back into the cavity of the probe laser. The isolator was used in conjunction with a half-wave-plate to attenuate the beam. A 92:8 pellicle beam splitter picked off a small amount of the probe beam whilst allowing the majority of the probe light through to interact with the sample. A photodiode power meter (Thorlabs S120C) measured the pick-off power. Before aligning the sample, the ratio between the power transmitted through the focussing lens and the power measured by the pick-off power meter was recorded. The ratio could then be used to determine the power incident upon the sample during the experiment. The sample is aligned so that the reflected beam is collinear with the incident beam. The reflected beam from the sample is reflected from the 92:8 beam splitter into the detection arm of the setup.

In the detection arm of the setup, a 50:50 pellicle splits the beam to measure open and closed scans simultaneously. Measuring both scans simultaneously removes the need to correct for fluctuations in probe power. The pick off power is monitored throughout to ensure that the laser is working as expected but the data is not used in extraction of the lens strength.

Work in this section was presented at SPIE 2015 [54]

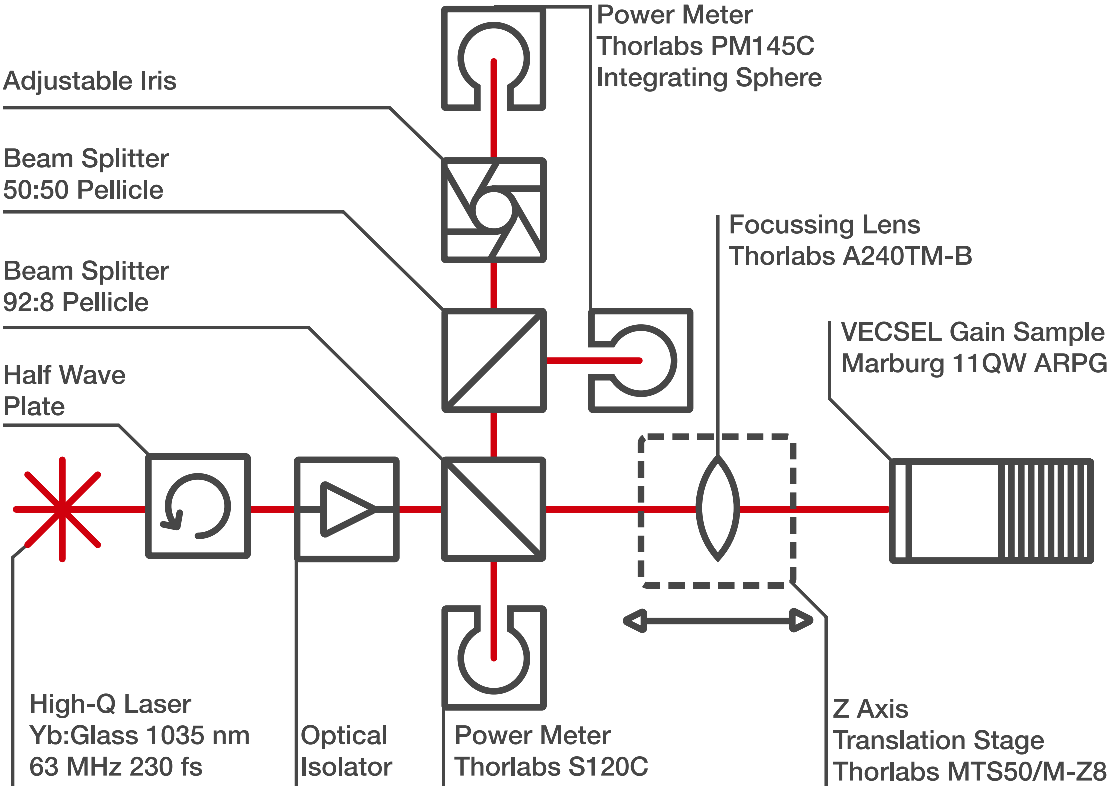

Figure 3.3: Schematic of the moving lens z-scan set experimental setup. The probe laser used is a modelocked Yb:glass laser producing 230 fs FWHM pulses with a Gaussian temporal profile at 63.4 MHz. The average power available at the sample was 130 mW. A half-wave-plate and optical isolator in combination control the probe power and prevent the reflected beam coupling back into the probe laser. A 92:8 pellicle beam splitter acts as a pick off to monitor the probe power and redirects the beam reflected from the sample into the detection arm of the experiment. An 8 mm aspheric lens mounted on a computer controlled translation stage controls the beam size incident on the sample. In the detection arm, a 50:50 pellicle beam splitter enables the full power of the beam (open scan) and the power transmitted through an aperture (closed scan) to be measured simultaneously.

Once aligned the system was tested for vibrational ring by taking repeated measurements but changing the delay, implemented in software, between completion of the stage move command and the power meter reading. The noise on the closed scan was analysed as this was the most susceptible to changes in the beam pointing. A delay of 100 µs was chosen, as increasing the delay beyond this value gave no measurable decrease in the noise measured: this is the point at which the vibrational noise introduced by moving the stage was less than the intensity noise from the laser and other vibration in the setup.

3.4.1 Results

Measurements were taken with the moving lens z-scan setup of the 11QW ARPG gain structure grown by Marburg University, Germany, detailed in section 2.3.4. The open scan data shows a reduction in reflected power centred on $z = 0$ where the probe fluence is highest; this is caused by non-linear absorption in the gain structure, fig. 3.4a. The closed scan data showing transmission through an aperture shows a large dynamic range due to the beam reflected from the sample coupling back through the lens, fig. 3.4b. The 10 mW result shows no deviation from the expected curve.

To extract the change in transmission due to non-linear lensing the closed scan data is divided by the open scan data, shown in fig. 3.5a. The background slope is then removed by dividing by the 10 mW data in which no lensing is observed, fig. 3.5b. The resultant curves have the characteristic shape of a z-scan response, demonstrating the presence of a non-linear lens in the sample.

The linearity of the way in which the peaks and the troughs in transmission vary with incident probe power are characteristic of an intensity-dependent lens. The linear variation of the change in transmission is a feature of z-scan theory based on third order non-linearities, suggesting that the non-linear lensing detected in the semiconductor gain sample is dominated by $\chi^{(3)}$ effects. Due to the changes in the setup from a traditional z-scan, it is not possible to apply existing z-scan theory to extract a value of $\chi^{(3)}$ for the sample.

3.4.2 Conclusion

The extracted z-scan data demonstrates the existence of a measurable lens in the OPSL gain structure. Moving the focussing lens exacerbates beam walk and makes the setup very sensitive to beam walk due to drift in the optical mounts. Frequent realignment of the setup is required.

The normalising technique used to obtain the z-scan curve is not a mathematically rigorous approach to extract values of lens strength. A more appropriate method to

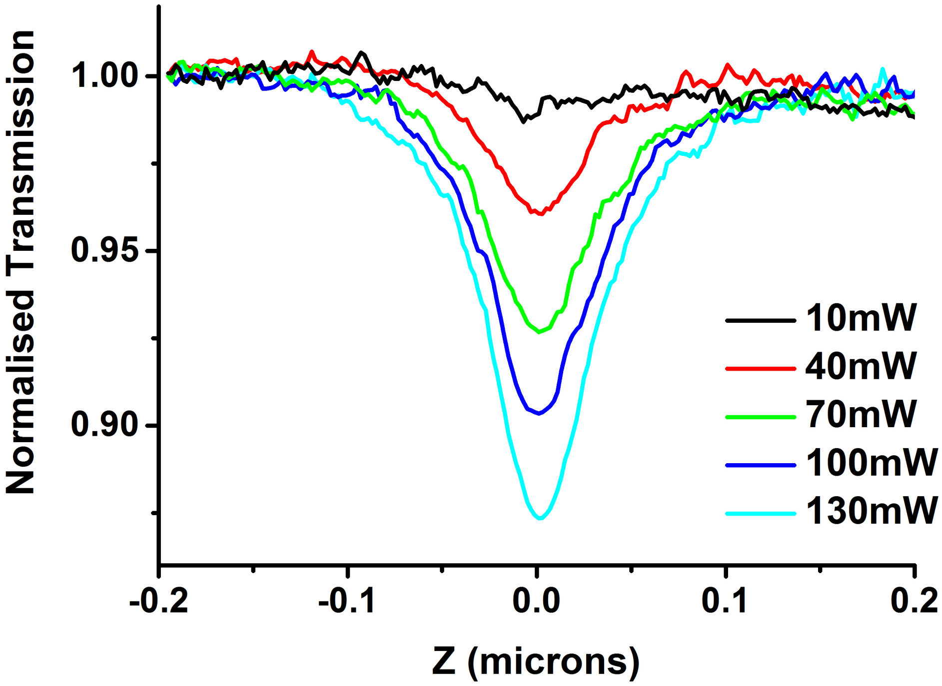

(a)

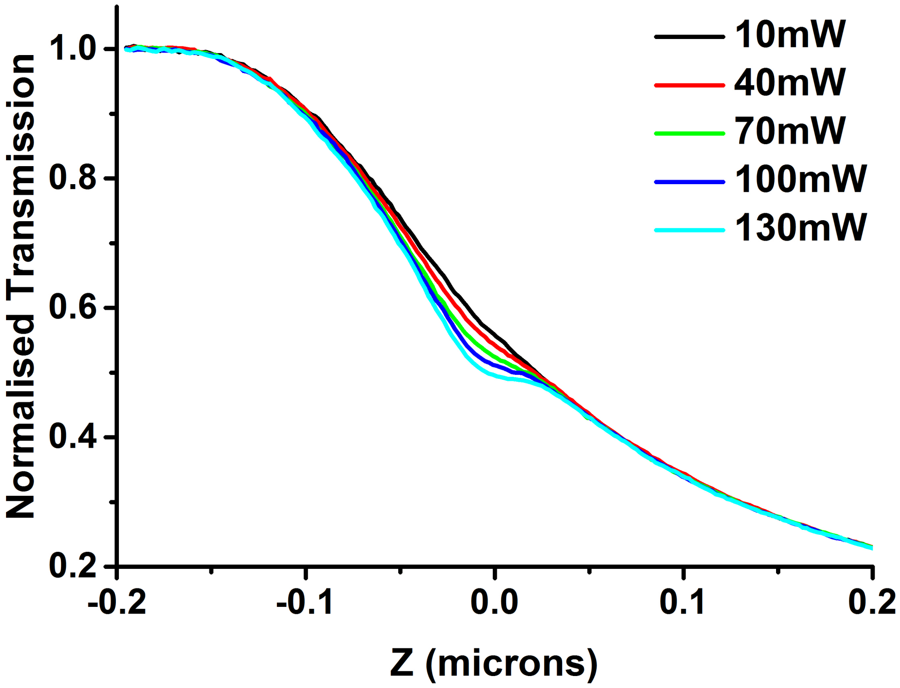

(b)

Figure 3.4: a) “Open” scan and b) closed scan data from moving lens z-scan measurements (fig. 3.3) of an 11QW ARPG Gain structure grown by Marburg University, Germany. Full details of the sample used can be found in section 2.3.4. The open scan data shows non-linear absorption centred on $z = 0$. The large dynamic range of the closed scan data is due to the reflected beam being coupled back through the focusing lens.

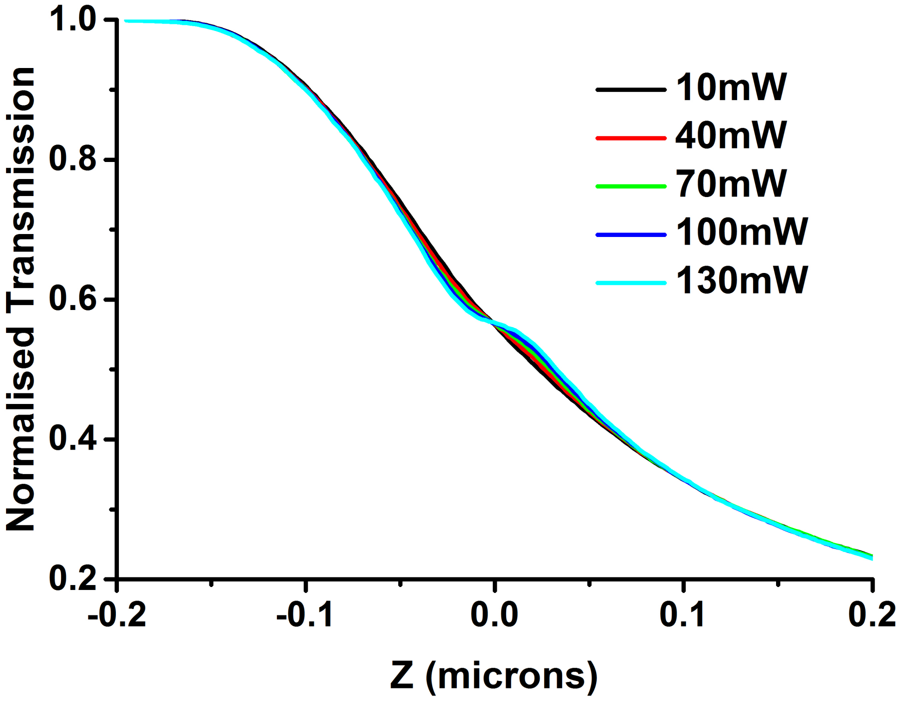

(a)

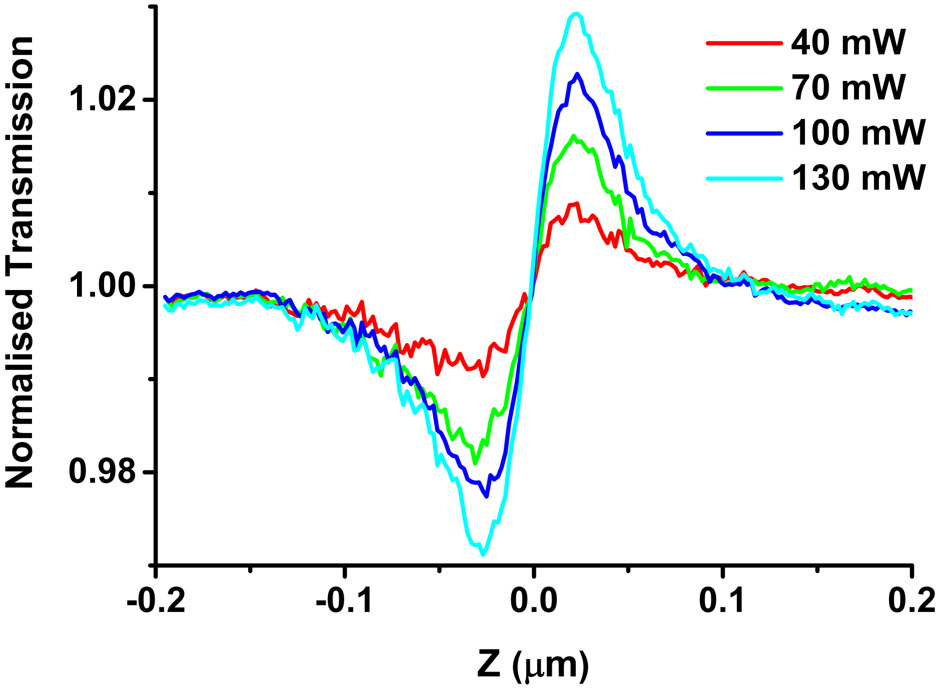

(b)

Figure 3.5: a) closed scan data divided by open scan data to remove the effects of non-linear absorption. b) The corrected data from a) is then divided through by the 10 mW data in which no lensing is observed to remove the sloped background to the data. The resultant curves have the characteristic shape of a z-scan response, demonstrating the presence of a non-linear lens in the sample.

measure the strength of the non linear lens would be to fit directly to the raw data. In practice, fitting to the raw data is problematic due to the large change in transmission in the absence of a non-linear lens. The change in the signal when a lens is present is a small feature on data that has a very large range of values. Extracting the lens strength by fitting to the power transmitted through an aperture would require very precise measurement of the distances between the optical components which are very sensitive fitting parameters if left to freely vary when fitting. As the purpose of these measurements was to verify the presence of a non-linear lens, the setup wasn't fully characterised before being broken down and re-engineered.

The identification of a measurable non-linear lens in an OPSL gain structure when probing on resonance with the quantum well emission is an important result. A better engineered approach to measuring the lens is detailed in section 3.5.

3.5 Reflection Z-Scan Measurement of a Resonantly Excited Gain Chip

The non-linear response of the OPSL gain chip was measured using a reflection z-scan, similar to the method demonstrated by Martinelli et. al. [49], shown in figure 3.8.

A custom breadboard was made on which to mount the gain sample being tested with a mirror to redirect reflected light from the sample parallel to the input beam. The sample and redirecting mirror are mounted together on a motorized translation stage to maintain a constant optical path length between the lens and the aperture.

The probe beam is focused onto the sample using an aspheric lens (Thorlabs A280TM-B), producing a focused spot radius of ∼5 µm. This spot size allows us to reach pulse fluences of up to 3 mJ cm^{-2} on the sample.

Collecting the whole beam onto a power meter (Thorlabs SC120) enables the detection of any change in intensity of the beam on reflection by the sample due to intensity dependent absorptions (open scan). Closing an aperture on the reflected beam causes the collected power to be dependent on any change in beam size due to non-linear lensing as well as intensity dependent absorptions (closed scan). When there is no lensing in the sample the measured transmission through the aperture will be constant.

Extracted z-scan curves, showing only the effect of non-linear lensing are obtained by dividing the power measured in the closed scan by the open scan for each point in z. The z-scan curves are then normalized so that for distances far away from the focus, z_0, there is no deviation from 1. The aperture size was set to give a 50 % transmission for large z magnitude, when no lensing effect is observed.

Measurements were performed for a range of incident probe powers up to the maximum average power of 140 mW. Adjustments to the incident beam path and the temperature control of the probe laser enabled the increase in the average power available at the sample. Below 30 mW the signal-to-noise ratio was too low for data extraction.

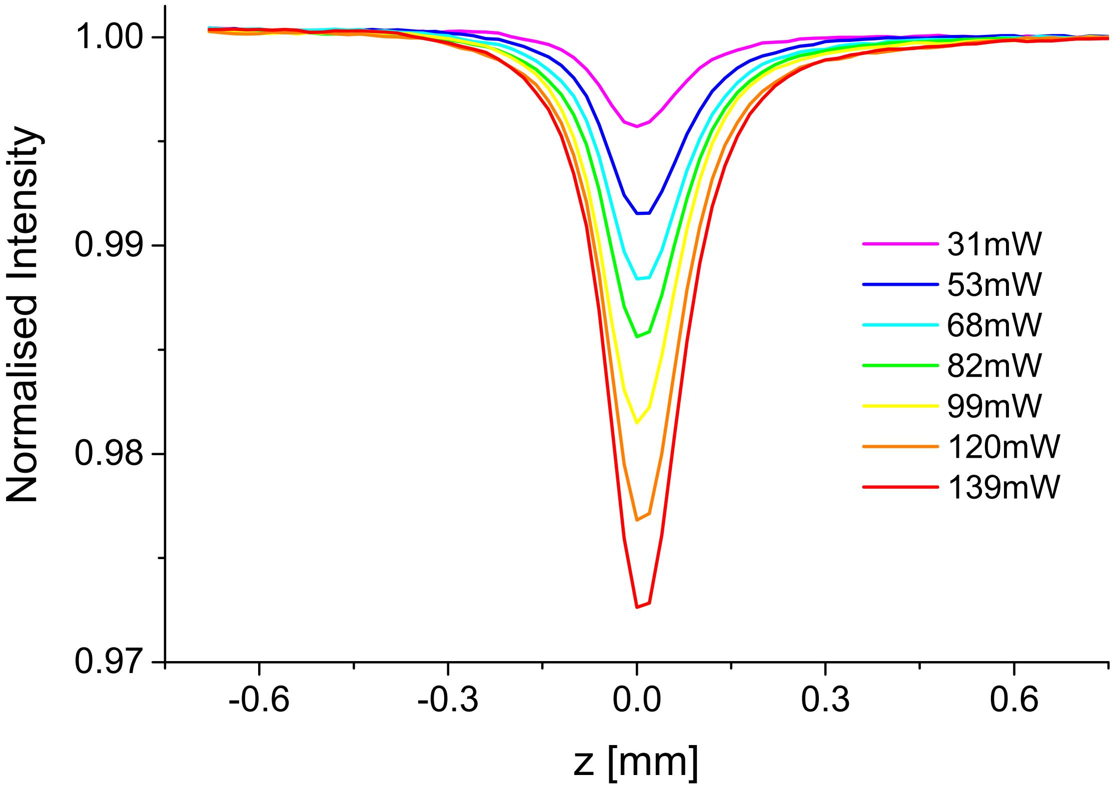

Figure 3.6: Normalised open scan data showing a large absorption feature, centred at z_0, that increases with increased average power of the pump beam.

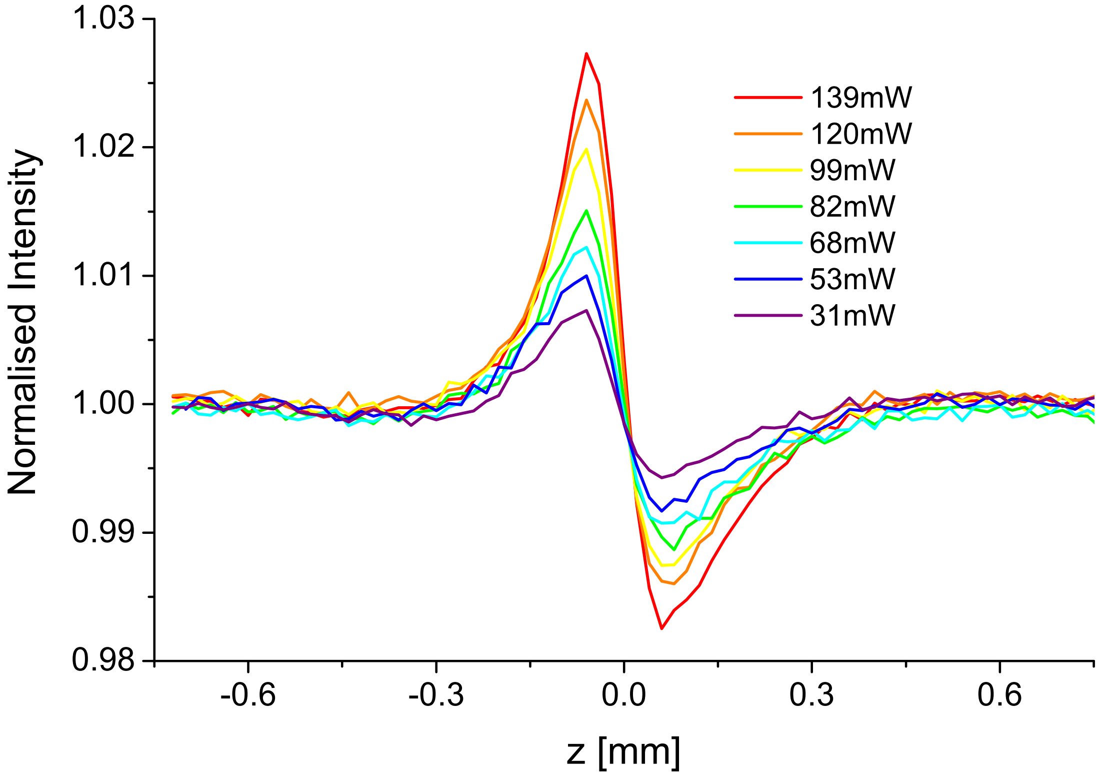

Figure 3.7: Normalised z-scan curves showing the deviation in transmission through an aperture as a result of non-linear lensing in the OPSL gain chip.

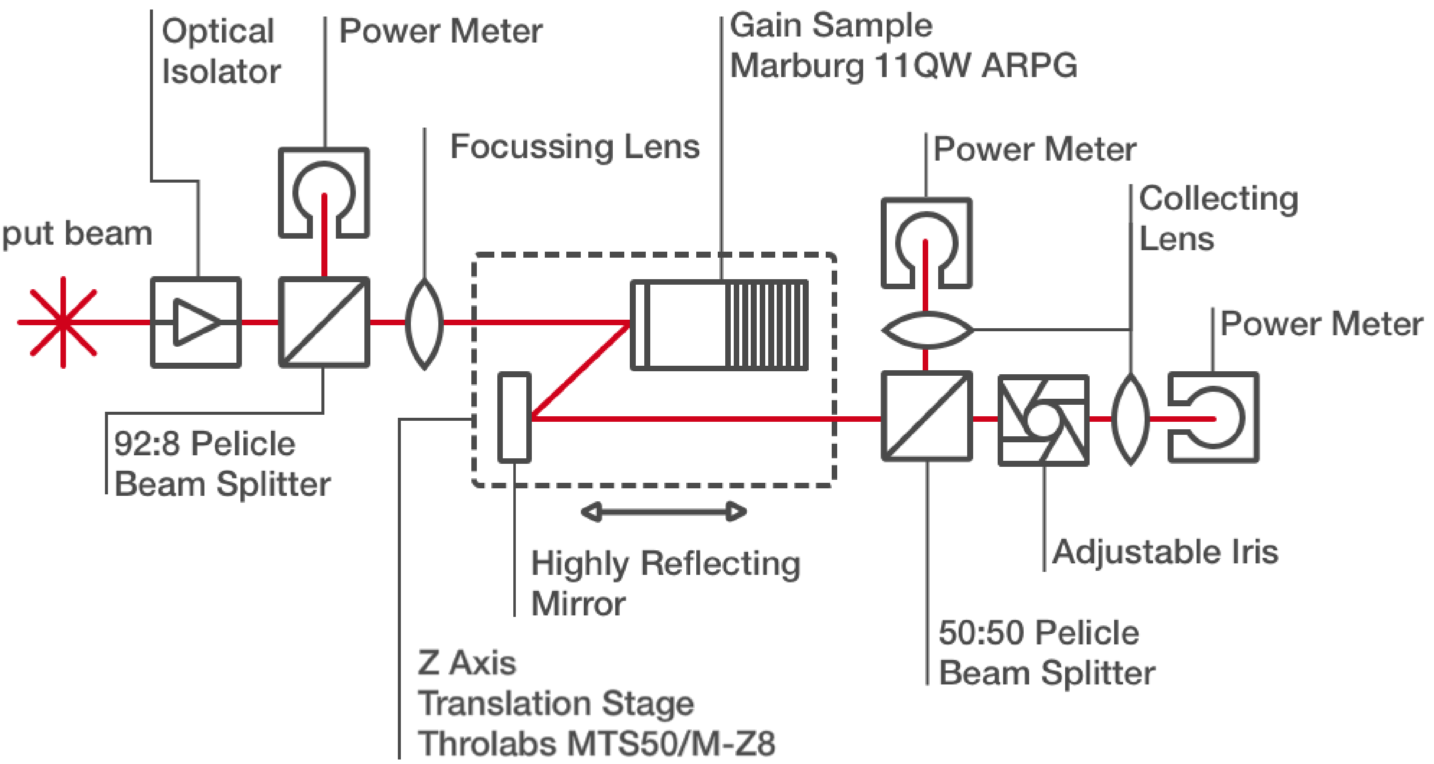

Figure 3.8: Schematic of the reflection z-scan setup. The incident intensity on the sample is varied by changing the position of the sample along the axis of the focusing probe beam (z-axis). Mounting the sample and a redirecting mirror on a translation stage maintains a constant optical path length to the aperture.

Open scans show a large absorption feature at the focus ($z = 0$) as shown in figure 3.6. The effect is likely to be dominated by two photon absorption (TPA).

The extracted z-scan curves for the various probe powers are shown in figure 3.7. The change in normalised intensity from a value of 1, about the z_0-position, is evidence of a non-linear lensing effect in the OPSL gain structure.

To extract a value for the lens strength, the data is fitted using the method described by Stryland et. al. for z-scan responses using Gaussian beams in which $\chi^{(3)}$ effects dominate [55]. Peak on-axis phase shift ($\Delta\Phi$), focused spot size (ω_0) and z_0 are left as free fitting parameters. An example fit is shown as the black line in figure 3.9.

The form of the theoretical z-scan curve differs from our data as the peak and trough deviate from the normalized transmission by different amounts. The source of this asymmetry in our data is unclear at present. Asymmetry leads to uncertainty in the extracted phase shifts. By fitting to only the peak or only the trough we achieve good fits to these sections of the data, providing upper and lower bounds to the extracted values, shown as the green and red curves in figure 3.9.

The extracted spot width was $(5.0 \pm 0.5)\,\mu\text{m}$ for all of the data analysed. The variation in the value of the zero offset between fits was much less than the step size of 20 μm.

The variation in extracted values of $\Delta\Phi$ with average probe power is shown in figure 3.10. The negative gradient of the change in $\Delta\Phi$ with incident power indicates that the sign of the lens is negative, acting to defocus the incident beam.

The linear trend of the change in peak on-axis phase shift suggests that the dominant mechanisms driving the changes in refractive index are due to third-order non-linear effects [55]. We calculate an effective n_2 value using equation 6 in reference 55. Fits to the peak and trough provide upper and lower bounds of $n_2 < -3 \times 10^{-13}\,\text{cm}^2\,\text{W}^{-1}$ and $n_2 > -6 \times 10^{-13}\,\text{cm}^2\,\text{W}^{-1}$ respectively.

The negative sign measured for n_2 corresponds to a defocussing lens, consistent with the observations reported for the same chip in Ref 53. The lens that we observe here is, however, weaker: reference 53 reports a value for n_2 of $(-1.5 \pm 0.2) \times 10^{-12}\,\text{cm}^2\,\text{W}^{-1}$.

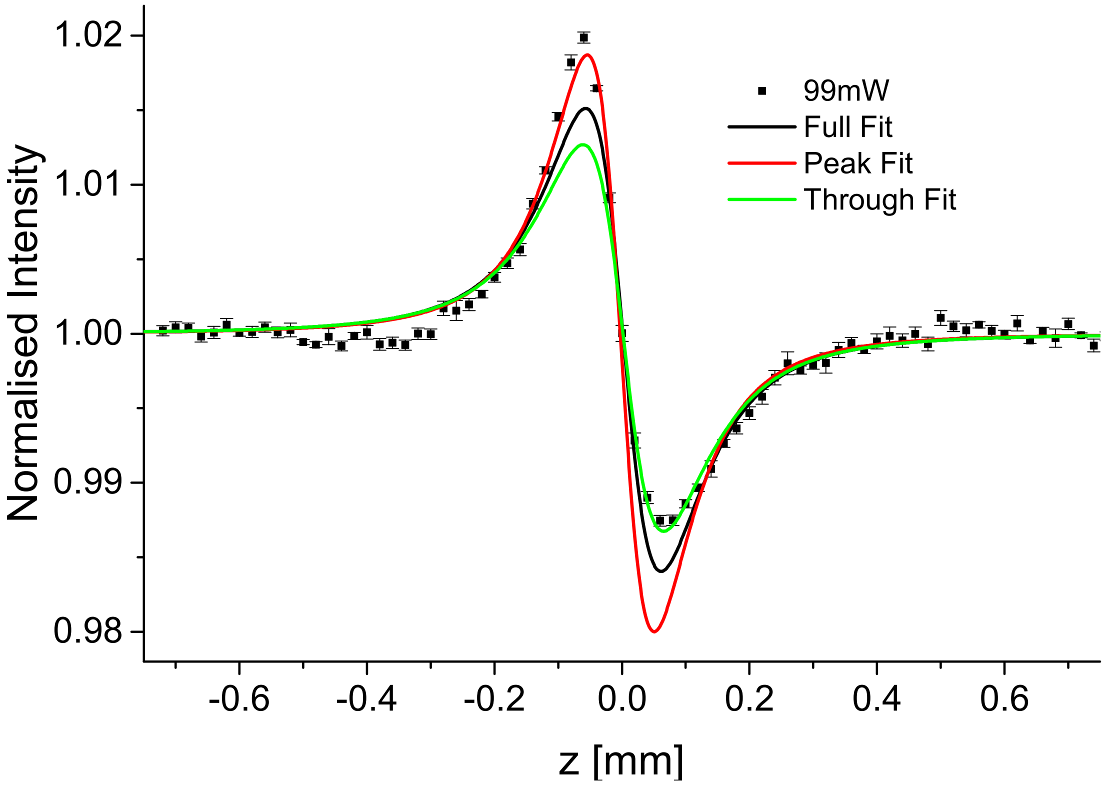

Figure 3.9: Fitted curves, calculated using the method described in Ref. [55], to the normalized z-scan response for 99 mW incident probe power. Fitting to the whole data set [black], fitting to the peak only [red] fitting to the trough only [green].

It therefore appears that the non-linear effect is weaker for 230 fs pulses at 1035 nm than for 10 ps pulses at 1064 nm. In both experiments, the temperature of the chip was maintained at 20°C.

The authors in reference 56 state that the value of n_2 for an OPSL gain structure is expected to be in the range from $-1 \times 10^{-13}\,\mathrm{cm}^2\,\mathrm{W}^{-1}$ to $-10 \times 10^{-13}\,\mathrm{cm}^2\,\mathrm{W}^{-1}$ based on a review of a number of experimental and theoretical publications [50, 51, 57, 52, 58]. A measured value of n_2 in bulk GaAs has been reported by reference 52 to be $-3 \times 10^{13}\,\mathrm{cm}^2\,\mathrm{W}^{-1}$ at a wavelength of 1060 nm.

Given the measurements here and those reported in reference 53 it is evident that there is a measurable non-linear refractive index in this OPSL gain structure.

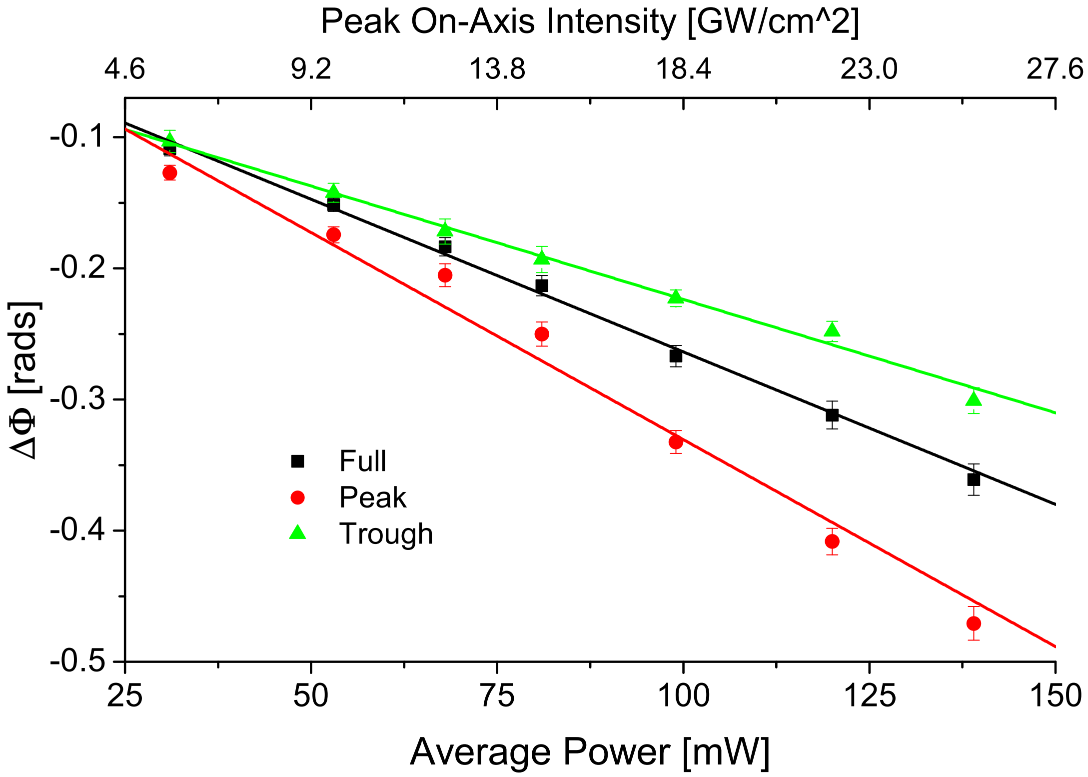

Figure 3.10: Peak on-axis phase shift ($\Delta\Phi$) extracted from fitting to the z-scan. The variation of $\Delta\Phi$ with peak on-axis intensity would be linear for non-linear lensing dominated by $\chi^{(3)}$ effects. Extracted phase shifts with linear fits are shown for fits to the whole curve [black], fits to the peak only [red], and fits to the trough only [green].

3.5.1 Conclusions

The non-linear lensing response of an optically pumped semiconductor laser (OPSL) gain structure has been characterised with a probe beam that has a centre wavelength, pulse duration and pulse fluence comparable with the intracavity field in a ML-OPSL.The phase shift is shown to vary linearly with incident power, consistent with a third order non-linearity. The value of n_2 is in the range of $-5.6 \times 10^{-13}\,\mathrm{cm}^2\,\mathrm{W}^{-1}$ to $-3.1 \times 10^{-13}\,\mathrm{cm}^2\,\mathrm{W}^{-1}$.

The limited power of the probe laser used constrained the geometry of the experiment to the point where it was not possible to pump the gain structure during the experiment. Pumping the gain chip during the z-scan is vital to match the intracavity conditions of the laser when measuring the non-linear lens.

The differences between the non-linear lens measured with a 10 ps pulse at 1064 nm and 200 kHz in reference 53 and that measured here with a 230 fs, 63 MHz at 1035 nm suggests a need for further investigation into the dependence of the lens strength on wavelength, peak power and pulse energy. These questions will be discussed further in the following chapter.

Chapter 4

Camera Reflection Z-Scans of a Pumped OPSL Gain Structure

4.1 Introduction

In this chapter we seek to generalise the extraction of the non-linear lens effects without assuming the nature of the lens. The assumptions of a thin sample and small non-linearity still hold for an OPSL gain structure allowing the experimental setup to be described by ray transfer matrices where the non-linear lens has an unknown focal length at each z position. If the input beam is well characterised, the lens strength at each z position can be extracted as a series of discrete data points and mapped to the beam parameters at that point in z. The lens strength can then be plotted as a function of any beam parameter that is also a function of z. In this way it's possible to isolate different lensing effects, for example separating a thermal lens from a non-linear lens.

Using a CMOS sensor the intensity profile of the beam can be directly measured [59]. Determining changes in beam size by measuring transmission through an aperture requires the assumption that both the beam and the lens are circularly symmetric. By using a camera we no longer need to make any assumptions about the geometry of the lens or the beam. Directly observing the beam assists in the alignment of the optical set-up and in detecting beam clipping which would manifest as fringes in the camera image.

4.2 Numerical Extraction of the Lens Strength

We assume that the lensing can be approximated to be a thin lens which allows the optical system to be described using ray transfer matrices. At the focus of the beam, the beam waist can be measured during initial set-up of the experiment and represented by the complex beam parameter (eq. (2.2)). The beam is then propagated a distance z to the sample. A lens at the sample acts on the beam with an unknown power K equal to the inverse of the focal length of the lens and measured in dioptres (m^{-1}).

Having measured the beam radius on the CMOS sensor, the strength of the lens can be calculated using the formula:

$$K = \frac{-zd - z_0^2 \pm \sqrt{(zd + z_0^2)^2 + (z^2 + z_0^2)(d^2 + z_0^2)(\Delta z - 1)}}{(d - z)(z^2 + z_0^2)}. \tag{4.1}$$

The full derivation of eq. (4.1) is detailed in appendix A.

The formula for the extracted lens strength has the complication that it gives two values for the lens strength at each point along the beams axis due to the use of the quadratic formula in the derivation. To test the extraction method we consider a sample with a negative Kerr lens and calculate the change in beam radius as a function of the position in z. Figure 4.1 shows the lens strength K(z) and the change in beam radius Δw(z).

Applying eq. (4.1) to the calculated change in beam radius Δw(z) gives two values for the lens strength depending on whether the terms inside the square root are added or subtracted. $K_{Extracted}$(z) is plotted in fig. 4.2. In order to calculate the point at which

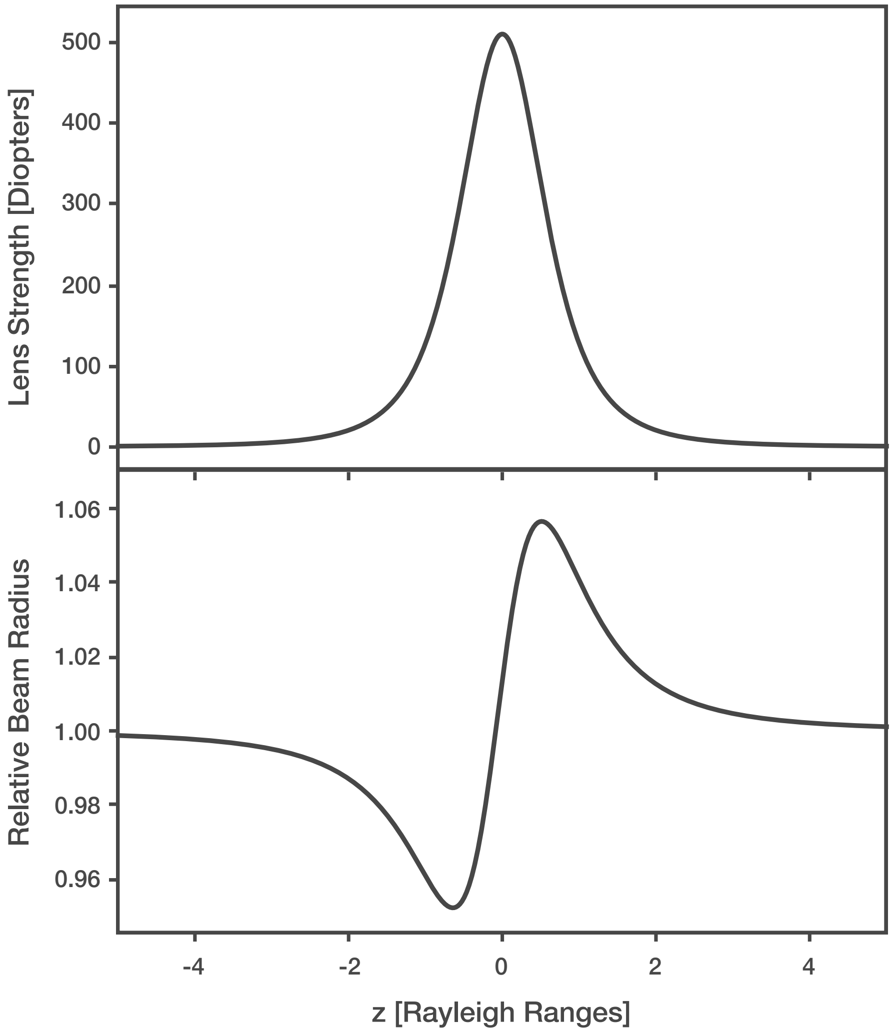

Figure 4.1: Calculated lens strength K(z) for a negative Kerr lens and the far field change in beam radius Δw(z).

we must transition from using the two versions of eq. (4.1), the value for which the terms inside the square root are equal to zero must be evaluated. The critical value of z, for which both versions of eq. (4.1) are equal, occurs when

$$\Delta \mathrm{z} = \frac{1-(zd+z_0^2)^2}{(d^2+z_0^2)(z^2+z_0^2)}, \tag{4.2}$$

where d is the distance from the focus to the measurement plane. Equation (4.2) is plotted in fig. 4.2.

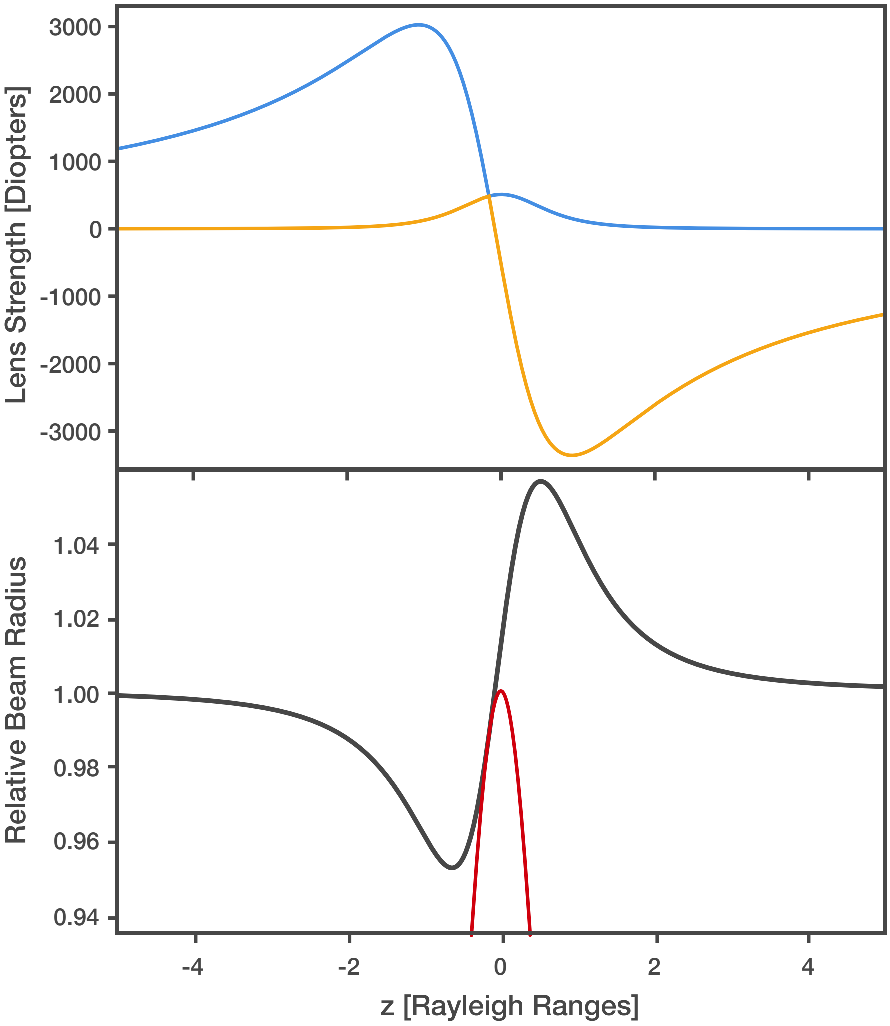

Figure 4.2: Extracted lens strength calculated using eq. (4.1). The critical value of z at which one must switch between the two versions of eq. (4.1) occurs when eq. (4.2) is satisfied, shown by the intersection of the two lines in the lower plot.

4.3 Experimental Design

The experimental set-up for the reflection z-scan measurements is shown in fig. 4.3. The setup is the same as described in fig. 3.8 in section 3.5 with the exception of the detection system after the reflection from the sample. A beam splitter diverts some of the beam to a power meter to monitor the power of the probe beam during the experiment.

The probe laser used was a Coherent Chameleon tunable modelocked Ti:sapphire laser, emitting 150 fs pulses at an 80 MHz repetition rate. The centre wavelength of the laser was broadly tunable from wavelengths that were shorter than the gain of the QW up to a wavelength of 1080 nm. Average powers of up to 500 mW were available at the sample. With the higher powers of the probe laser, the focussed spot size could be increased to 10 µm. A larger focussed spot size compared to the experiments described in section 3.5 enabled the distances between optical components to be increased due to the lower divergence of the probe beam. Increased distances between components enabled the sample to be pumped with an 808 nm fibre-coupled diode laser with a 400 nm diameter focussed spot size with a top-hat profile.

The object plane of the imaging system was experimentally measured. The camera, lens and attenuating optics were mounted on a linear translation stage. The camera was then advanced towards the redirecting mirror until defects on the surface of the gain sample came into focus. The object plane of the imaging system was then considered to be on the surface of the mirror. The camera was then wound back a known distance using the micrometer adjustment screw.

An example of an image of the beam and the extraction of the beam radius is shown in fig. 4.5. The spot was aligned to this point on the camera to avoid debris on the sensor. Two such scattering spots can be seen on the left-hand side of the image. These did not affect the fitting of a two-dimensional Gaussian profile to the beam image. Had a scattering spot interfered with the extraction of the beam parameters, a mask could be applied to remove the problematic pixels from the numerical fit.

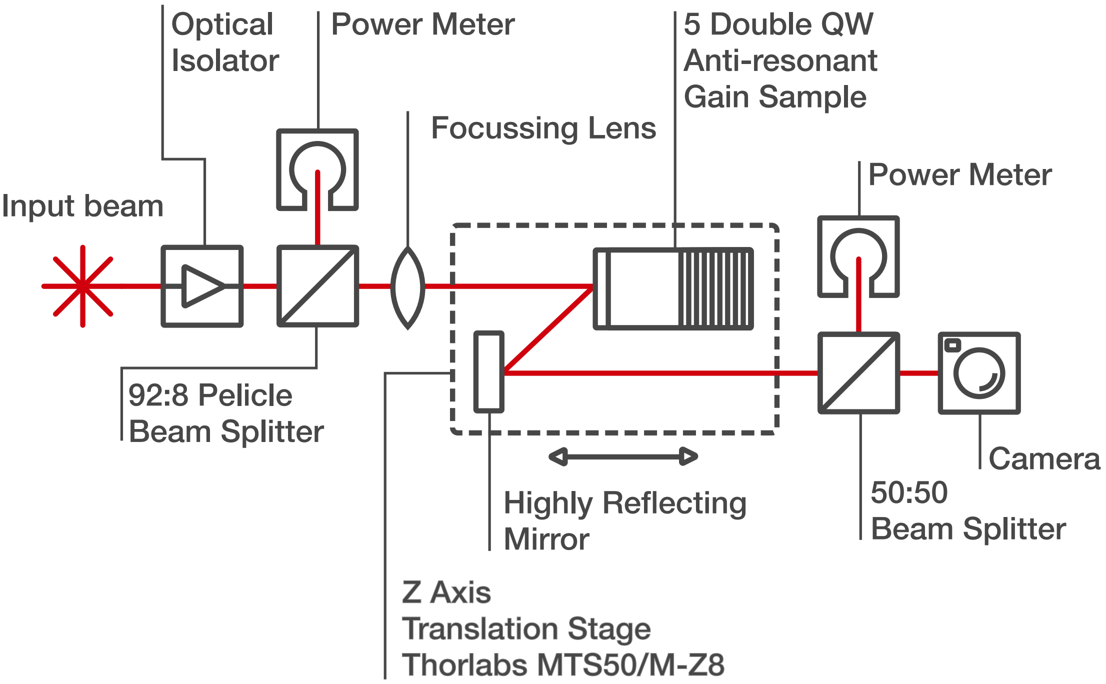

Figure 4.3: Schematic of the reflection z-scan setup. The incident intensity on the sample is varied by changing the position of the sample along the axis of the focusing probe beam (z-axis). Mounting the sample and a redirecting mirror on a translation stage maintains a constant optical path length to the aperture. The camera is detailed further in fig. 4.4.

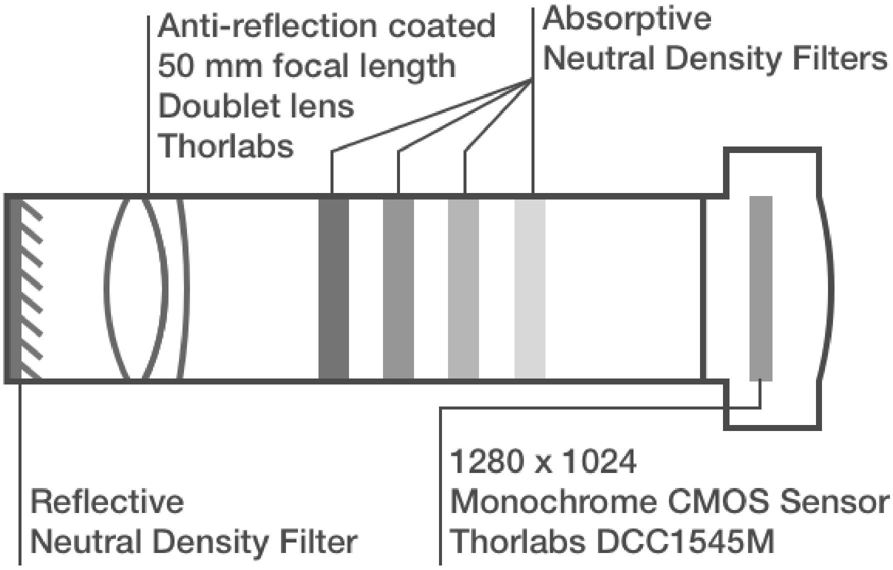

Figure 4.4: Schematic of the imaging system used. The beam was initially attenuated by a reflection neutral density (ND). A reflective filter was selected to avoid a thermal lens forming due to the large attenuation of the laser beam at the first filter. Subsequent attenuation used absorbative ND filters to avoid interference fringes from back reflections obscuring the image.

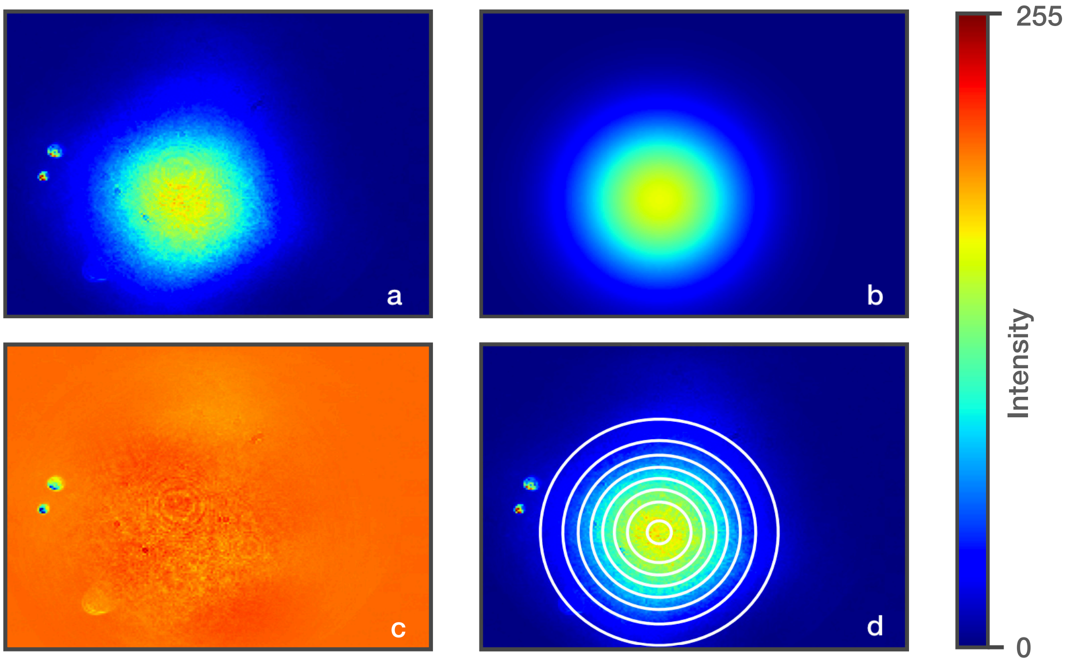

Figure 4.5: Numerical fitting to the beam images for the reflection z-scan measurements. All images are plotted on the same colour scale for comparison. a) The original image. Scattering spots are visible on the left-hand side of the image. b) The extracted beam shape from the regression algorithm. c) Residuals from the fitting algorithm, rescaled to increase the contrast in the colour map. d) Fitted Gaussian overlaid as a contour plot on the original image.

4.4 Results

Camera z-scan measurements were made of the 5 double QW gain sample described in section 2.3.5. The water chiller that was being used in the temperature control system was not functioning during data acquisition but the fault was not discovered at the time. As the temperature was not being stabilised, the temperature of the gain chip fluctuated during data acquisition. Thermal expansion of the optical mount holding the gain chip caused instability in the position of the sample. Realignment of the setup was required between every scan and as a result a constant distance between the focus of the probe beam and the camera was not maintained. The lens extraction formula described in section 4.2 could not be applied to the results, as the distance between components changed during the experiment.

Camera z-scan measurements were taken for a range of values of probe power, pump power and at centre wavelengths of 1010 nm and 1035 nm. The change in the beam radius at the camera is shown in fig. 4.6 for a z-scan with an average probe power of 150 mW and centre wavelengths of 1010 nm and 1035 nm without pump light. All of the results show a sloped background indicating a change in beam size that is not related to the non-linear lens. In z-scan measurements a lens of constant focal length in the sample will produce linear change in the beam size at the detection plane. The linear change in beam size creates a slope to the background of the measured non-linear lens response. In the case of an OPSL gain sample being measured, the lens of constant focal length is a thermal lens due to temperature gradients within the probe spot. The thermal lens is larger than would be expected under normal operating conditions due to poor extraction of heat from the sample that results from the malfunctioning temperature control system.

The shape of the variation in beam radius for the measurements at 1035 nm are qualitatively different. The 1035 nm results display features typical of z-scans for thick samples in that the peak and the trough in the variation in beam size is separated by a flat section. As the wavelength offset to the design wavelength of the DBR increases, the penetration into the DBR increases. This effectively increases length of the interaction

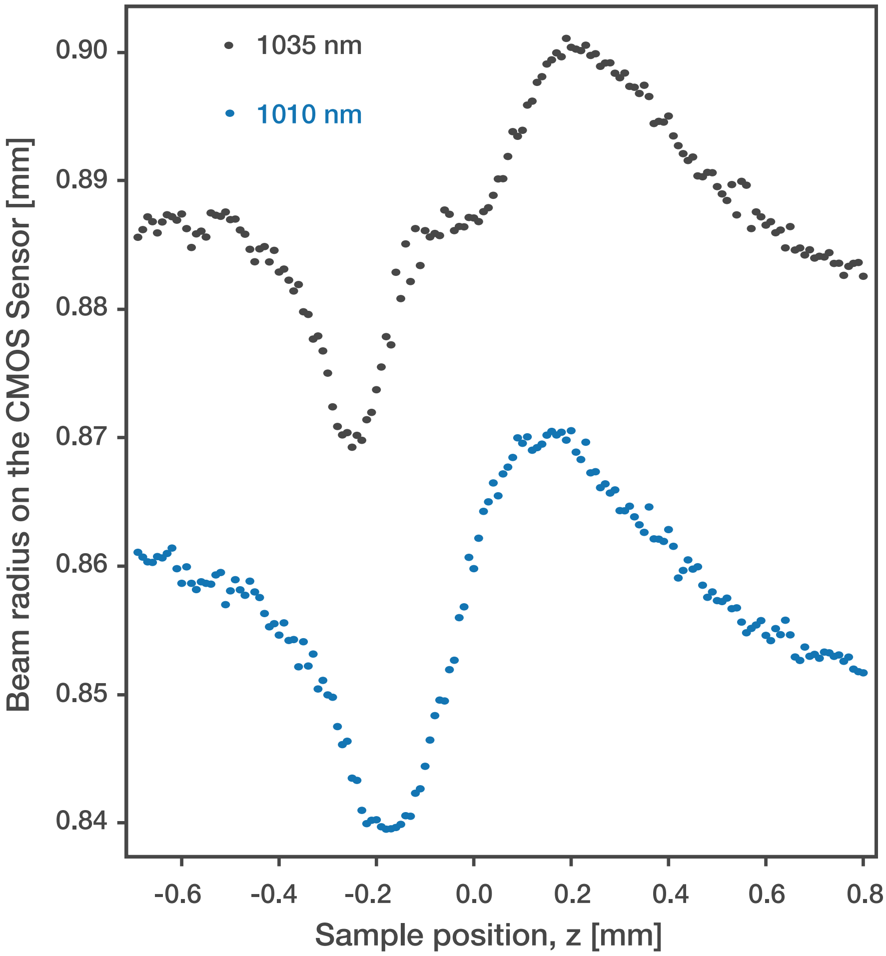

Figure 4.6: Camera z-scan measurements of a 5 double QW gain structure grown at Ulm University, Germany. The probe power used was 150 mW incident upon the sample at a centre wavelength of 1035 nm (Black) and 1010 nm (Blue).

of the incident light at 1035 nm as compared to 1010 nm light. This increased effective thickness of the sample could be sufficient for the thin lens approximation to break down.

Figure 4.7 shows a comparison between z-scans at 1010 nm, with 300 mW of average probe power and both with and without optical pumping of the sample. The increase in overall beam size for the pumped z-scan is due to movement of the optical components between scans. The pumped z-scan shows a steeper slope to the data indicating the presence of a stronger thermal lens as might be expected due to the additional thermal energy being deposited into the chip by the probe beam. The deviation in beam diameter due to the non-linear lens appears smaller in the pumped scan compared to the unpumped scan. Direct comparison between the scans is not possible due to the strong thermal lens and the overall change in beam sizes.

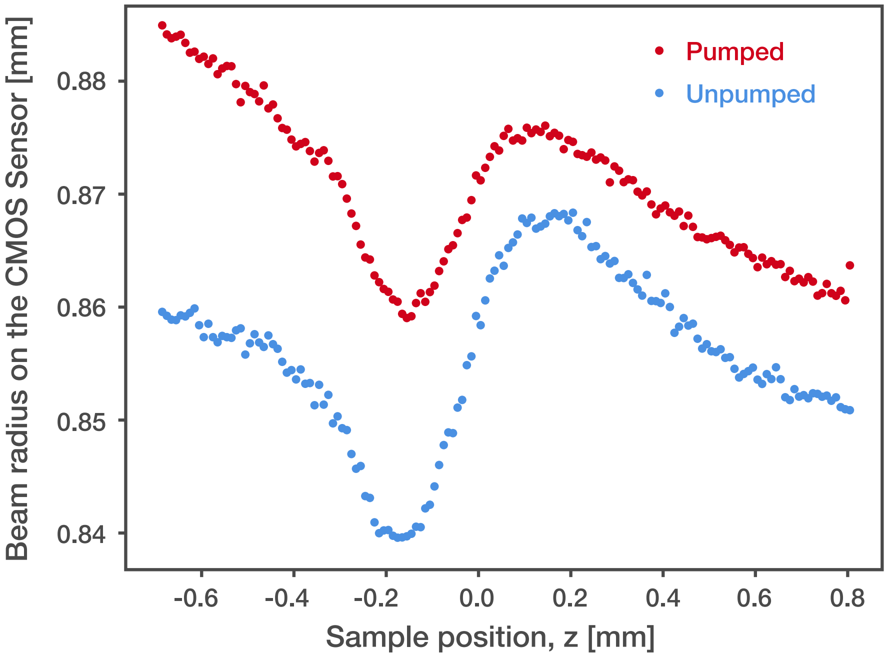

Figure 4.7: Camera z-scan measurements of a 5 double QW gain structure when unpumped (blue) and when pumped (red). The probe power used was 300 mW incident upon the sample at a centre wavelength of 1010 nm.

The 1010 nm z-scans are analysed using ray transfer matrices to represent the optical path between the focus of the probe beam and the camera. The lens within the gain structure is approximated by an intensity dependent Kerr lens and a thermal lens of fixed focal length. An example of a fitted change in beam radius is shown in fig. 4.8, for a z-scan with 300 mW of pump power incident on the gain sample and a centre wavelength of 1010 nm. The fitted line matches closely to the region of the measurements representing an increase in the beam radius. The region of the z-scan response in which the beam size is reduced does not match the theoretical response.

Similarities can be drawn between the deviation from the expected z-scan shape based on a Kerr lens of the measurements presented in section 3.5 and those shown in fig. 4.8. The peak in the graph from section 3.5 corresponds to an increase in the transmission through a circular aperture and therefore a reduction in beam size. When the beam size is reduced in both sets of measurements, the feature is both narrower and deviates further from the mean compared to what is predicted by a Kerr lensing response.

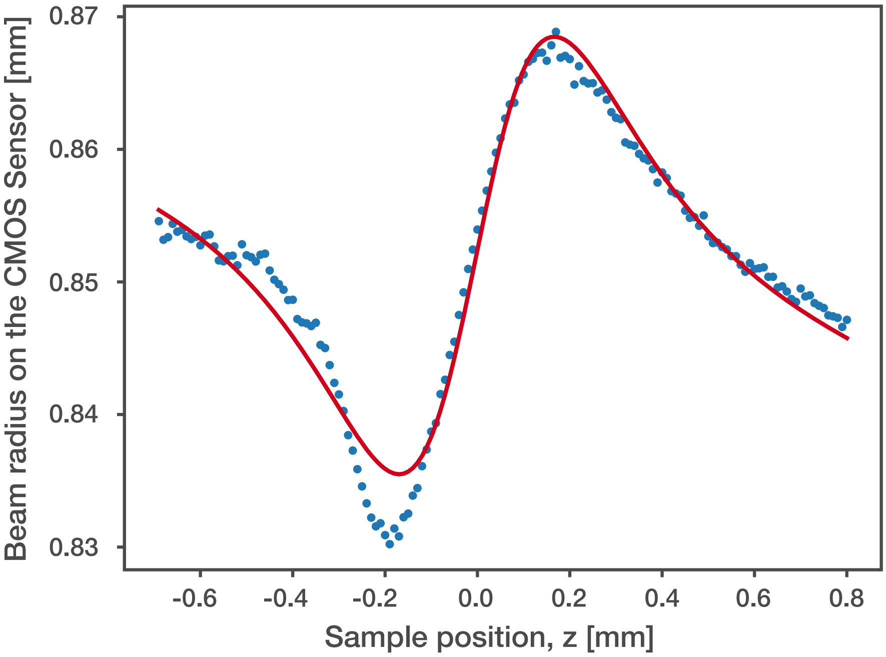

Figure 4.8: Change in beam radius on the CMOS sensor as a function of the position of the OPSL gain structure. The probe beam had an average power of 150 mW and a centre wavelength of 1010 nm. The sample was not pumped for this measurement. The response is fitted using ray transfer matrices to describe the optical path between the focus of the probe beam and the camera. The non-linear lens is described as an intensity dependent Kerr lens added to a thermal lens of fixed focal length.

4.5 Conclusions and Future Work

Due to the lack of effective thermal management of the sample during the experiment, the measurements of the non-linear lensing is not representative of laser operating conditions and therefore the strength of the non-linear lens cannot be quantified. A qualitative assessment of the change in measured beam radius at the camera shows that the z-scan response of the 5 double QW sample probed at a wavelength of 1010 nm is consistent with the measured response of the 11 QW periodic gain structure measured in section 3.5.

The use of a CMOS sensor over an aperture gives much greater confidence in the alignment of the measurement setup: if the beam is being occluded, diffraction fringes are visible in the image. The pointing of the beam can be monitored during the experiment by recording the centre of the beam on the CMOS sensor. Imaging the beam can be used to aid in the alignment of the experiment and to monitor the stability of the beam's pointing during data collection.

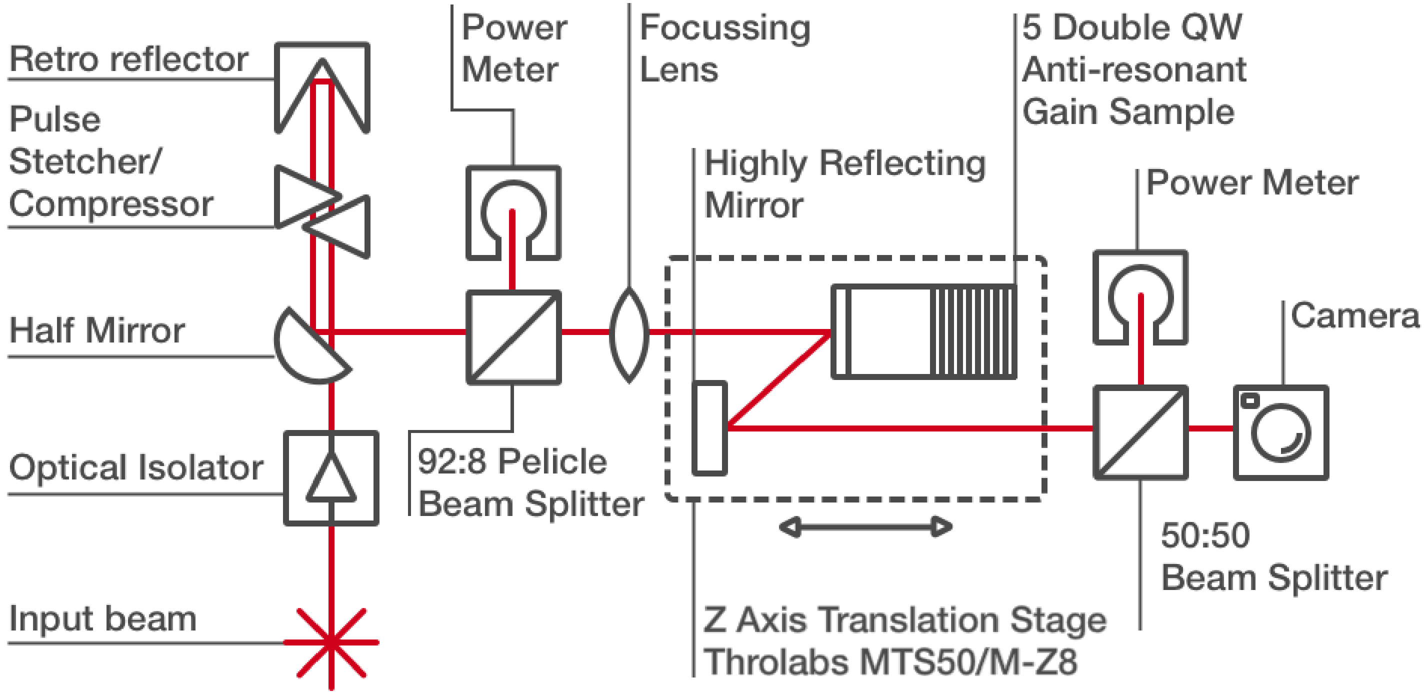

Figure 4.9: Schematic of the experimental setup with the addition of a grating pulse stretcher/compressor. This setup is capable of mapping the non-linear lensing in an OPSL gain structure as a function of the pulse energy, peak power, pulse duration and centre wavelength of the probe laser and of the pump intensity.

This experimental design can be further adapted by adding a pulse compressor/stretcher as shown in fig. 4.9. In addition to measuring the non-linear lensing response of the OPSL gain structure as a function of probe power, centre wavelength and pump intensity, changing the pulse duration as well as the probe power would enable the pulse energy and the peak power to be varied independently. A lens that was strongly dependent on the pulse energy of the probe beam would indicate that a large component of the lensing effect relates to carrier dynamics in the gain structure. Varying responses from pulses of the same energy but with different pulse durations would indicate the time dependence of the lensing effect.

Chapter 5

Modelling Pulse Formation in a Modelocked OPSL

5.1 Introduction

Modelling pulse propagation is an important tool to inform laser design in the pursuit of shorter pulses and higher peak powers. Described in this chapter is a model of pulse formation in an OPSL which is used to explore the sensitivity of an OPSL cavity to Kerr lensing. The model is derived from the work of Paschotta *et al.* and Sieber *et al.* who published validation of the same numerical approach for 363 fs duration pulses [60, 61, 41]. In addition, the presented model can be used to explore the transient dynamics of pulse formation and the emergence of a stable ML pulse.

An alternative to the presented approach employs microscopic modelling and has been published by the groups of S. Koch and J. Maloney [62, 63]. Microscopic modelling simulates OPSL behaviour using many-body theory to describe carriers in the gain and the absorber. Microscopic models solve the semiconductor Bloch equations, by considering the Coulomb interactions between the carriers and propagating the E-field using Maxwell's wave equations. Many-body calculations are computationally intensive and require a supercomputer to run the code, taking days or weeks to simulate. The body of code for microscopic modelling has been developed over more than a decade and has been commercialised as a software product by the name of Simulase™ from Non-linear Control Strategies (NLCSTR). As such this knowledge base is not openly available to the research community, presenting a significant barrier to entry into this field of research.

The modelling presented in this chapter is based on the principles of Haus's theory of modelocking [64]. Processes such as gain, loss, saturable absorption and dispersion are all considered to impart small changes to the pulse during each cavity round trip. The operators describing interactions with the intra-cavity elements are derived from macroscopic parameters that can be experimentally measured or theoretically calculated. The model itself is non-spatial. Interactions with the gain structure and the SESAM are reduced to energy operators calculated using the spatial profile of the intra-cavity beam.

For pulses approaching 100 fs the work of Waldburger *et al*, using a similar model to the one presented here, diverges from experimental results [32]. This would suggest that, on time scales approaching 100 fs, one or more assumptions in the model break down. Reports of self-modelocked (SML) OPSLs present pulse durations ∼500 fs therefore comparisons can be made between simulations and reported results as the time scales of the pulses are greater than 100 fs.

The parametrised model presented here can be used effectively in both the exploration of potential designs for self-modelocked OPSLs, and the investigation of how a non-linear lens in the gain structure could affect the operation of SESAM modelocked OPSLs.

5.2 Modelling with a Small Pulse-Centered Temporal-Window

In order to describe the E-field of the laser pulse numerically, we use an array of discrete data points. The data points representing the E-field are evenly spaced in time and cover a time period that is a fraction of the round trip time of the cavity. The time period over which the E-field is simulated is referred to as the time window of the simulation. By simulating only the time around the laser pulse, we save computation time by not processing data for the time within the cavity when there are no features of interest. Within the simulated window, time is measured relative to the peak of the intra-cavity pulse and outside of the window the intracavity power is assumed to be zero.

Some interactions between the pulse and the gain or the absorber are most easily described in terms of time. Other effects relate to how different wavelengths of light interact with the semiconductor structures within the cavity. The spectral components of the pulse are calculated based on the variation of the E-field in time using Discrete Fourier Transforms (DFTs). Computationally, the E-field amplitudes are transformed between the time and frequency domains using the Fast Fourier Transform (FFT) algorithm and its inverse the iFFT. For a given array size N, shortening the time window increases the temporal resolution but also expands the frequency window, lowering the spectral resolution, as is typical with FFT driven computation.

As gain and absorption are considered to make small changes to the pulse upon each round trip, the order in which operators are applied becomes arbitrary. Operators do not need to mimic the series of interactions that the pulse makes in a single round trip of the cavity and can instead be applied in the order that is most efficient programmatically. Therefore, operators are grouped so that only a single FFT and iFFT are required per round trip.

The recovery of the gain and the absorption in time are most easily described in the time domain. As the gain and absorption is applied in the time domain the operators are based solely on energy dynamics in the cavity, photons in the cavity are effectively considered to be colourless. The spectral filtering effects of the gain are not easily described in the time domain: the E-field is therefore transformed into the frequency domain where a spectral filter is applied as a frequency operator. The effects of dispersion within the cavity are applied in the frequency domain before the E-field is transformed back into the time domain ready to simulate the next round trip.

The round trip time is calculated from the repetition frequency f_{rep}. When modelling pulses of duration less than 1 ps, a window of duration of 10 ps is used. For a 1 GHz cavity a 10 ps simulation window represents one hundredth of the cavity round trip time. Dispersion and the effects of saturable gain and absorption cause the pulse to shift in time within the temporal window. Re-centring the pulse in the time window prevents the pulse from hitting the edge of the window and introducing numerical artefacts from the fast Fourier transforms.

The model is set up to simulate a typical OPSL V or Z-cavity, as detailed in section 2.6.2, with two interactions with the gain and one interaction with the SESAM per cavity round trip. Outside of the time window the intra cavity power is assumed to be zero, allowing gain recovery to be calculated analytically. The delay between sequential interactions with the gain is calculated from the position of the gain structure within the cavity. Dispersion and the saturation energies of the gain and the absorber are considered to be constant during the formation of the pulse.

The model has been written in the Python programming language (version 3.6) using the numerical programming library NumPy.

5.2.1 Temporal and Spectral Arrays

The mathematical treatment of the pulse uses the slowly varying envelope approximation [41, 61, 60].

$$E(t) = \Re\left\{\mathrm{A(t)}\exp(-i\omega_c t)\right\}$$

where E is the electric field strength of the intracavity beam, A(t) represents the time varying envelope of the pulse and w_c is the carrier, or central, frequency of the laser. The power inside the cavity is defined as

$$P(t) = |\mathrm{A(t)}|^2. \tag{5.1}$$

Operators are applied to an array of amplitudes with N elements, either A(t) or $\tilde{\mathrm{A}}(f)$ depending on the operator where

$$\tilde{\mathrm{A}}(f) = \mathrm{FFT}\,(\mathrm{A(t)}) \tag{5.2}$$

and

$$\mathrm{A}(t) = \mathrm{iFFT}\left(\tilde{\mathrm{A}}(f)\right). \tag{5.3}$$

For efficient computation of the FFTs, the number of array points, $\mathrm{N} = 2^n$ where n is an integer.

A window size W denotes a temporal window from $\frac{-W}{2}$ to $\frac{W}{2}$. Given an array with number of points N, the temporal resolution is defined by

$$\Delta t = \frac{W}{N}. \tag{5.4}$$

The corresponding frequency window ranges from $\frac{-N}{2W}$ to $\frac{N}{2W}$ relative to the peak gain of the laser, f_c, with a frequency resolution, defined by

$$\Delta f = \frac{1}{W}. \tag{5.5}$$

Pulses are considered to be sampled sufficiently if 20 points cover the steady state temporal and spectral profiles [61, 41].

5.2.2 Gain and Absorption Operators

Interaction with the gain and the saturable absorber is numerically defined by a saturation fluence and with one and two temporal recovery coefficients respectively. For the specific laser cavity being modelled, the radius of the intracavity pulse at the gain and the absorber are used to calculate the respective saturation energies. Gain is initially equal to the small signal gain, g_{ss}, and absorption to the modulation depth of the absorber, $-\Delta\mathrm{R}$. Details of how these values are experimentally measured can be found in section 2.5.1.

On short timescales, the exponential recovery can be approximated to be linear as the energy recovered in time Δt is small compared to the saturation energy, $E_{\mathrm{sat,g}}$. At each time step the gain is reduced due to energy being extracted from the carrier population and then recovers with time constant τ_{gain} according to the differential equation

$$\frac{dg(t)}{dt} = -g(t).\frac{P(t)}{E_{\mathrm{sat},g}} + \frac{g_{ss} - g(t)}{\tau_{\mathrm{gain}}}. \tag{5.6}$$

For $\Delta t \ll \tau_{\mathrm{gain}}$,

$$g(t+\Delta t) = g(t) + \Delta t\left(\frac{g_{ss} - g(t)}{\tau_{\mathrm{gain}}} - \frac{g(t)P(t)}{E_{\mathrm{sat},g}}\right). \tag{5.7}$$

Between interactions with the time window the gain recovers exponentially over time T:

$$g(t+T) = g_{\mathrm{ss}} + (g(t) - g_{\mathrm{ss}})\exp(-T/\tau_g). \tag{5.8}$$

The saturation of the semiconductor gain implies a change in the real part of the refractive index [41]. A phase shift of $\Delta\phi$ is applied in proportion to the gain at each point in time given by

$$\Delta\phi(t) = -\frac{\alpha_g(t)}{2}, \tag{5.9}$$

where α_g is the Linewidth Enhancement Factor (LEF) for the gain.

A single interaction with the gain chip is calculated by multiplying the array of temporal amplitudes, A(t) by

$$\exp\left[\frac{g(t)}{2}\left(1-i\alpha_g\right)\right]. \tag{5.10}$$

In the SESAM the two stage recovery relates to a double exponential decay of a single body of carriers. On short timescales (i.e. on the order of the time step Δt) the two components can be calculated independently as the energy recovered in time Δt is much smaller than the saturation energy, $E_{\mathrm{sat,a}}$. The two recovery processes are weighted by a constant, s, where $0 \leq s \leq 1$. An interaction with the absorber is described by the differential equation

$$\frac{dq(t)}{dt} = -q(t).\frac{P(t)}{E_{\mathrm{sat},a}} + \frac{\mathrm{s}\left(\Delta\mathrm{R}-q(t)\right)}{\tau_{\mathrm{slow}}} + \frac{\left(1-\mathrm{s}\right)\left(\Delta\mathrm{R}-q(t)\right)}{\tau_{\mathrm{fast}}}. \tag{5.11}$$

For $\Delta t \ll \tau_{\mathrm{fast}}$,

$$q(t+\Delta t) = q(t) + \Delta t\left(-q(t).\frac{P(t)}{E_{\mathrm{sat},a}} + \frac{\mathrm{s}\left(\Delta\mathrm{R}-q(t)\right)}{\tau_{\mathrm{slow}}} + \frac{\left(1-\mathrm{s}\right)\left(\Delta\mathrm{R}-q(t)\right)}{\tau_{\mathrm{fast}}}\right). \tag{5.12}$$

The phase shift associated with the saturable absorption in the SESAM is

$$\Delta\phi(t) = -\frac{\alpha_q(t)}{2}. \tag{5.13}$$

The effect of a single interaction with the SESAM is calculated by multiplying the array of temporal amplitudes, A(t) by

$$\exp\left[\frac{q(t)}{2}\left(1-i\alpha_q\right)\right]. \tag{5.14}$$

5.2.3 Spectral Filtering

Owing to the finite gain bandwidth observed in real lasers, an amplitude filter must be imposed upon the spectrum. We model this as a parabola centred in wavelength on the peak in the small signal gain. The amplitude filter is normalised so that it does not amplify the pulse. In this way the amplification of the gain, and its spectral filtering due to the gain bandwidth, are applied as separate operators. The normalised amplitude filter, $\mathcal{F}_{\mathrm{norm}}$, is a parabolic function taking the form

$$\mathcal{F}_{\mathrm{norm}}(\lambda) = 1 - \left(\frac{\lambda - \lambda_c}{\Delta\lambda}\right)^2, \tag{5.15}$$

where $\Delta\lambda$ is the normalised filter width and

$$\lambda = \frac{c}{f}.$$

The normalised power filter is then

$$\mathcal{F}^2_{\mathrm{norm}}(\lambda) = \left(1 - \left(\frac{\lambda - \lambda_c}{\Delta\lambda}\right)^2\right)^2.$$

The power filter must be matched to the peak and width of the measured spectral gain.

$$\mathcal{F}^2(\lambda) = (1 + g_{ss}) \times \left(1 - \left(\frac{\lambda - \lambda_c}{\Delta\lambda}\right)^2\right)^2.$$

The power filter, $\mathcal{F}^2(\lambda) = 1 + \frac{g_{ss}}{2}$ when $\lambda = \lambda_c \pm \frac{\lambda_{\mathrm{FWHM}}}{2}$, hence

$$1 + \frac{g_{ss}}{2} = (1 + g_{ss}) \times \left(1 - \left(\frac{\lambda_{\mathrm{FWHM}}}{2 \times \Delta\lambda}\right)^2\right)^2$$

and therefore

$$\Delta\lambda = \frac{\lambda_{\mathrm{FWHM}}}{2 \times \sqrt{1 - \sqrt{\frac{1 + \frac{g_{ss}}{2}}{1 + g_{ss}}}}}. \tag{5.16}$$

Combining eq. (5.15) and eq. (5.16) we get the equation of the spectral filter. Spectral filtering is assumed to be constant during pulse formation. Each round trip $\tilde{A}(f)$ is multiplied by $F_{\text{norm}}(f)$ twice, once for each gain pass.

5.2.4 Dispersion

Chromatic dispersion is defined by the Taylor expansion of the wavenumber $k(w)$ about a central frequency w_0,

$$k(w) = k_0 + \frac{\partial k}{\partial w}(w - w_0) + \frac{1}{2}\frac{\partial^2 k}{\partial w^2}(w - w_0)^2 + \frac{1}{6}\frac{\partial^3 k}{\partial w^3}(w - w_0)^3 + \ldots \tag{5.17}$$

The quadratic term, $\frac{\partial^2 k}{\partial w^2}$ represents second order dispersion or Group Delay Dispersion (GDD) and the cubic term, $\frac{\partial^3 k}{\partial w^3}$ represents Third Order Dispersion (TOD).

Dispersion is considered to be constant throughout the pulse formation and is represented by a single value for GDD and TOD representing the total dispersion during a full round trip of the cavity. The phase change relative to the group velocity is calculated as a function of the relative frequency $f - f_c$

$$\Delta\phi(f) = \text{GDD} \times \frac{(2\pi(f - f_c))^2}{2} + \text{TOD} \times \frac{(2\pi(f - f_c))^3}{6}. \tag{5.18}$$

5.2.5 Noise

Noise in the model represents spontaneous emission from the gain. Implementing the noise only in a small pulse-centred temporal window does not represent the noise of the laser accurately.

As the spectral resolution of the simulation is set by the length of the time window, each point in the frequency array represents tens to hundreds of cavity modes. In the early stages of laser build-up it is beating between the frequency components that creates noise spikes due to the random phase. Pulse formation occurs when a noise spike is able to partially saturate the absorber and by doing so open up a window of net gain. Due to the low spectral resolution, the noise implemented in a small pulse-centred window cannot accurately replicate this process.

The laser power outside of the time window is zero. This is representative of real cavity conditions once the pulse energy is very much greater than the energy in the noise. This approximation breaks down in the early stages of build up from noise, before a pulse has formed, as the gain recovery is overestimated. Simulating the build up from noise does not provide a physically realistic pulse evolution and is insufficient evidence upon which to conclude that the laser is self-starting, as competition between noise spikes is not representative of the conditions inside of a real laser cavity.

One effect that can prevent a single pulse from propagating around the cavity in a fundamental modelocked regime is the formation of a secondary pulse. The laser operation will tend to favour two or more pulses within the cavity if it is more energy-efficient to have multiple pulses instead of one. The propensity of a laser to support more than one pulse within the cavity is referred to as a multi-pulsing instability. Multi-pulsing instabilities in OPSLs are thought to occur when the gain is left for too long between interactions with the pulse. Between interactions between the gain and the pulse, the gain recovers sufficiently to support a second pulse within the cavity. As noise is not simulated outside of the time window, the noise added to the cavity in each round trip will not destabilise the pulse. Expanding the temporal window to cover the entire round trip ($T = \frac{1}{f_{rep}}$) could provide an insight into pulse evolution from noise and pulse stability. This idea is discussed further in section 5.3.

The deficiencies in the representation of noise limit the ability of a small pulse-centred window to answer key questions about the pulse: does the set of parameters give rise to self-starting modelocking? Is the pulse temporally stable? And will multiple pulses form within the cavity?

It has been reported by Sieber *et al* that initiating a simulation with a pulse already in the cavity will reach the same steady state [41]. This is also found to be true for the implementation of the model presented here. When starting the simulation from a pulse, the steady state is reached after fewer round trips of the cavity.

Starting the simulation with a pulse in the cavity and not including noise in the simulation saves computation time. The small pulse-centred window model provides a quick numerical method to determine the steady state pulse characteristics for a given set of laser parameters.

5.2.6 Convergence Criteria

The goal of the model is to reach a steady state. The conditions with which the model determines whether a steady state has been reached are referred to as the convergence criteria. Convergence criteria are used to numerically determine whether the simulation has reached a steady state. Three pulse characteristics are checked: peak power, pulse energy and pulse duration. If the variance in all three characteristics over 3000 round trips is less than 0.5 % the simulation is deemed to return a steady state solution. To reduce computation time, pulse characteristics are measured every 10 round trips. The peak power is taken to be the maximum amplitude in the temporal array of amplitudes, A(t). Pulse energy is proportional to the sum of the temporal array of amplitudes, $\sum \mathrm{A(t)}$. Pulse duration is taken to be the full-width at half-maximum (FWHM) of the pulse in the time domain.

If the pulse does not reach a steady state after 10 000 round trips the simulation terminates. If there is not a steady state solution for the parameters being simulated, the pulse will collapse. If the time resolution is too low, numerical oscillations can cause the variance to remain higher than the convergence criteria after reaching steady state. An example of temporal oscillations is shown in fig. 5.1. Numerical oscillations greater than 0.5 % would prevent simulation reaching the convergence criteria despite having reached a steady state. Examining the evolution of the pulse characteristics can determine the reason that the simulation did not converge. Numerical oscillations can be removed by running the simulation again with a higher temporal resolution.

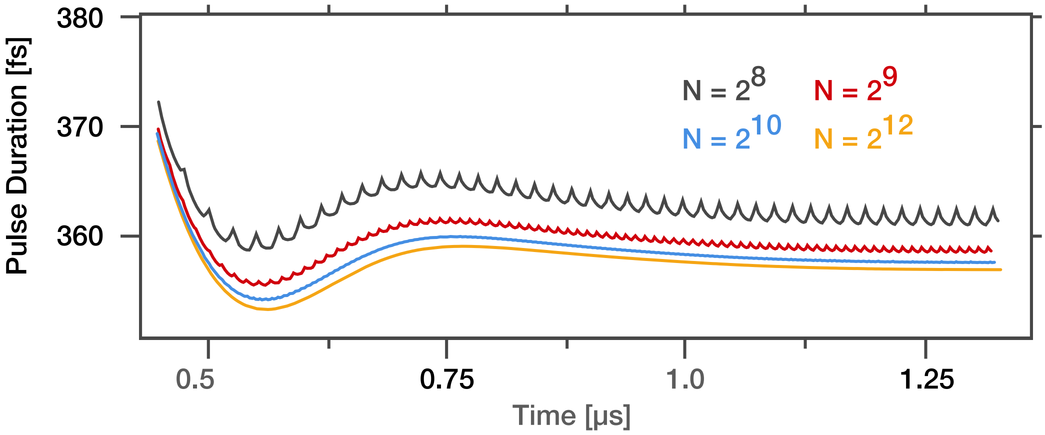

Figure 5.1: Evolution of the pulse duration as a function of time for simulations with varying numbers of points, N, in the temporal and spectral arrays. Oscillations in the steady state occur when Δt is not sufficiently less than the time constants of the gain and the absorber. Despite the oscillations all four simulations met the convergence criteria after about 5200 round trips.

5.2.7 Optimisation

Most of the operators in the model can be implemented as array operations using NumPy. As NumPy is written in the C programming language these functions are well optimised.

A For loop iterates over the temporal amplitudes and calculates the changes in gain or absorption at each time step once per interaction. Using a For loop is unavoidable as the gain calculation is causal: the gain at a moment in time relates to the value of the gain in the previous time step. To speed up these computations the code was partially compiled into the C programming language using Cython. This reduced the computation time to a maximum of ~10 s if the pulse did not converge.

Gain Parameters		SESAM Parameters		Cavity Parameters	
g_{ss}	5 %	ΔR	1.8 %	loss	0.8 %
$F_{\text{sat,g}}$	45 µJ/cm^2	$F_{\text{sat,q}}$	5 µJ/cm^2	oc	1 %
r	120 µm	r	120 µm	f_{rep}	3.97 GHz
α_g	3	α_q	2	GDD	50 fs^2
τ_{gain}	3 ns	τ_{slow}	9 ps	TOD	0 fs^3
λ_{FWHM}	26 nm	τ_{fast}	430 fs		
λ_c	966 nm	share	0.5		

Table 5.1: Simulation parameters taken from ref 41. These parameters are used in all simulations presented in this chapter unless otherwise specified.

5.2.8 Results

Initial simulations using the model were run on the same parameter set that was experimentally verified by Sieber *et al* [41]. The parameters used are listed in table 5.1. Unless otherwise stated, all other simulations are based on this set of laser parameters. These values have been chosen to enable the exploration of the parameter space around values for which the model has been experimentally verified.

In OPSLs the small signal gain, g_{ss}, for samples designed for modelocking is 2 % to 5 %. The total loss, including including output coupling, the absorbers saturable loss (modulation depth, ΔR) and other non-saturable losses, must be less than the small signal gain for the cavity to lase. Typically, non saturable losses are less than 1 %, saturable losses are 0.3 % to 1.5 % and output coupling is 0.1 % to 2 %. The saturation fluence of the gain, $F_{\text{sat,g}}$, has been measured to be from 30 µJ/cm^2 to 80 µJ/cm^2 [65]. The saturation fluence, $F_{\text{sat,q}}$, of the SESAM that uses a single quantum well as the absorber layer is inversely proportional to the modulation depth and can cover a wide range of values from 5 % to 50 %. Repetition rates, f_{rep}, can be as low as 100 MHz and as high as tens of gigahertz. Recovery times are not often measured and are not well documented in the literature. The gain recovery time, τ_{gain}, will be in the range of 2 ns to 4 ns. For the SESAM the fast recovery time, τ_{fast}, would be less than 1 ps and the slow recovery time, τ_{slow}, would be in the range of 1 ps to 10 ps with a share of 0.3 to 0.7. The total GDD of a laser cavity that has been optimised for low dispersion would be expected to be in the range $-500\,\mathrm{fs}^2$ to $500\,\mathrm{fs}^2$ with close to zero values of higher order dispersion. Values for the linewidth enhancement factors, α_g and α_q, are not measurable parameters between 1 to 10. The gain bandwidth, λ_{FWHM}, is in the range of 5 nm to 50 nm.

The simulation was run with array points $\mathrm{N} = 2^{12}$ and a window size of 8 ps giving a temporal resolution of ~2 fs. The simulation was initialised with a low-power, 1 ps pulse in the cavity.

The evolution of the pulse is shown in fig. 5.2. The temporal profile of the pulse, fig. 5.2a, remains centred at time t=0 by the recentring function, narrowing to its steady state value over approximately 2000 round trips or 0.5 µs of simulated time. The spectral profile broadens over the initial 500 ns, as seen in fig. 5.2b. As the peak power in the cavity rises, the spectral profile shifts to longer wavelengths due to the phase shifts associated with the gain and the absorption.

Temporal evolution of pulse energy, pulse duration and peak power is shown in fig. 5.3. The pulse energy quickly rises to its steady state. As the pulse energy rises there is little change in the pulse duration. As the rise of the pulse energy slows, the pulse duration starts to fall, the peak power increases and the position of the peak shifts to longer wavelengths as the energy is condensed in time. Both the pulse duration and the peak power overshoot their respective steady state values before settling on their final values.

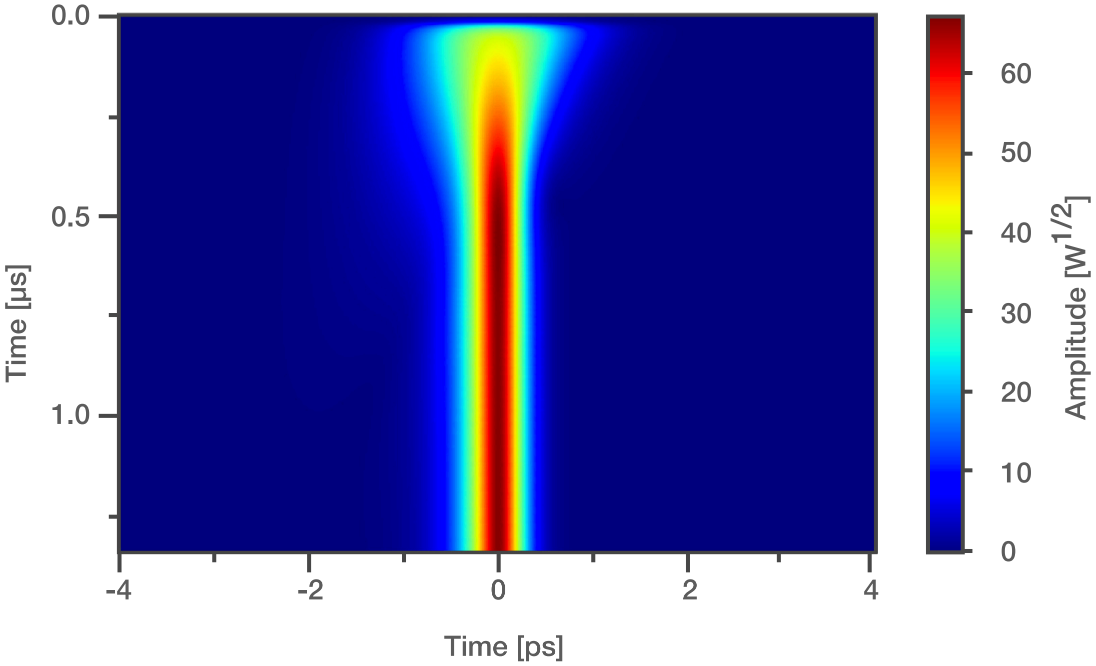

(a)

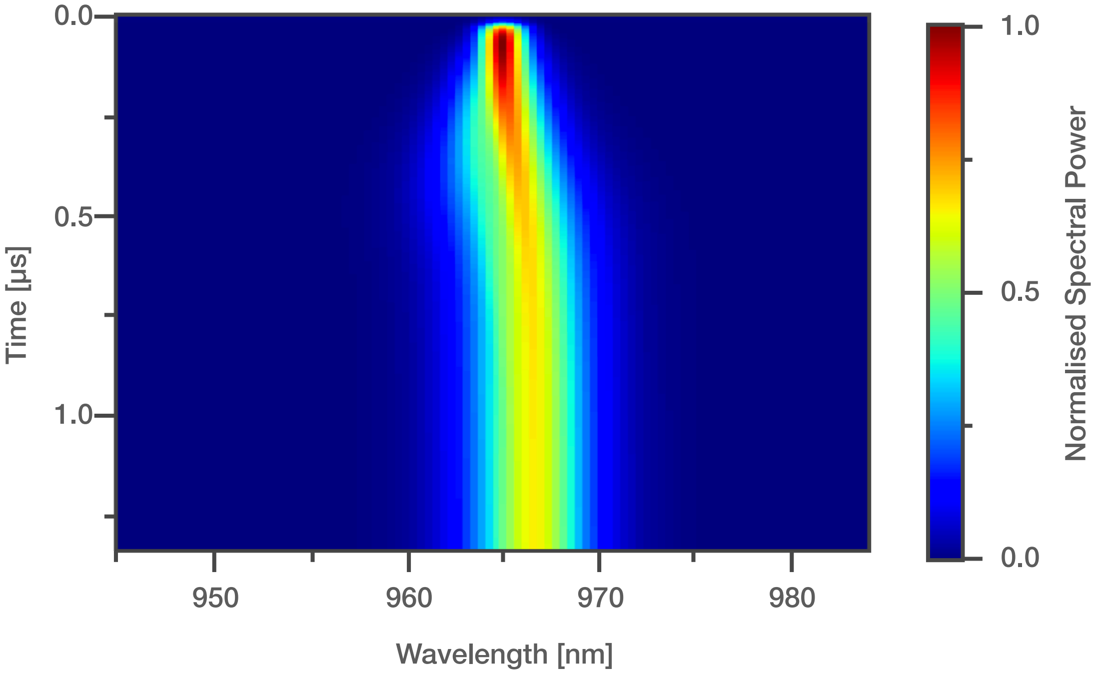

(b)

Figure 5.2: The evolution of (a) the temporal profile of the pulse and (b) the spectral profile of the pulse for a simulation of a laser with the parameters that are listed in table 5.1. The simulation was run with array points $N = 2^{12}$ and a window size of 8 ps giving a temporal resolution of 2 fs. The simulation was initialised with a 1 ps pulse in the cavity.

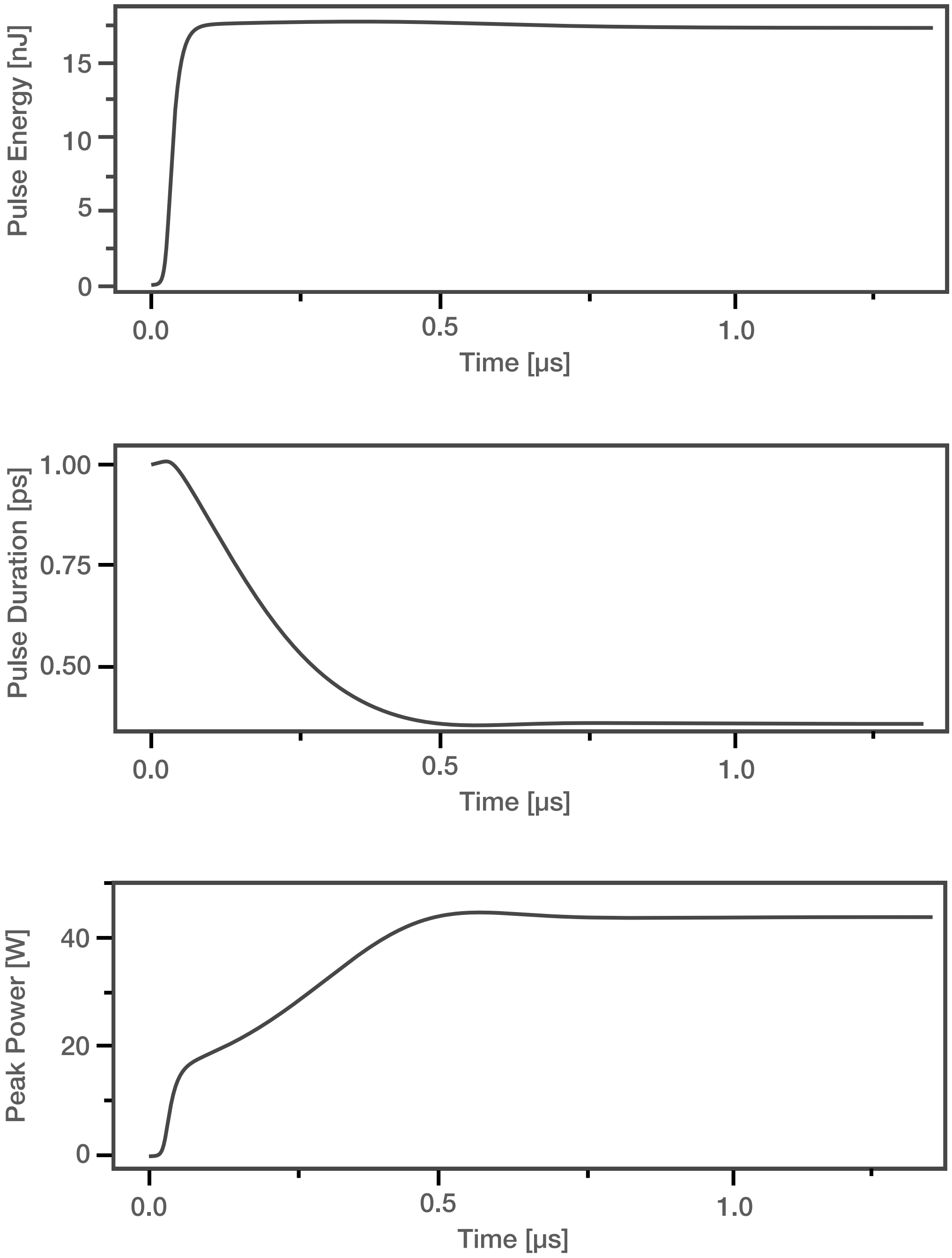

Figure 5.3: Temporal evolution of pulse energy, pulse duration and peak power for the laser parameters listed in table 5.1 with W = 8 ps and N = 2^{12}.

	ETH Experimental Data	ETH Simulation Results	Simulation Results
Pulse Duration [fs]	364	363	357
Spectral Width [nm]	3.04	3.06	3.20
Average Power [mW]	70	69	69
Transform Limit	1.13	1.15	1.17

Table 5.2: Pulse parameters published by Sieber *et al.* for both the experimentally measured and computationally simulated laser operation [41]. This is compared to the simulated pulse using the model described in this chapter. The pulse duration and the spectral width were taken to be the full-width at half-maximum (FWHM) with linear interpolation between data points. The resolution of the simulation and the numerical method for determining the pulse duration were not detailed in ref 41.

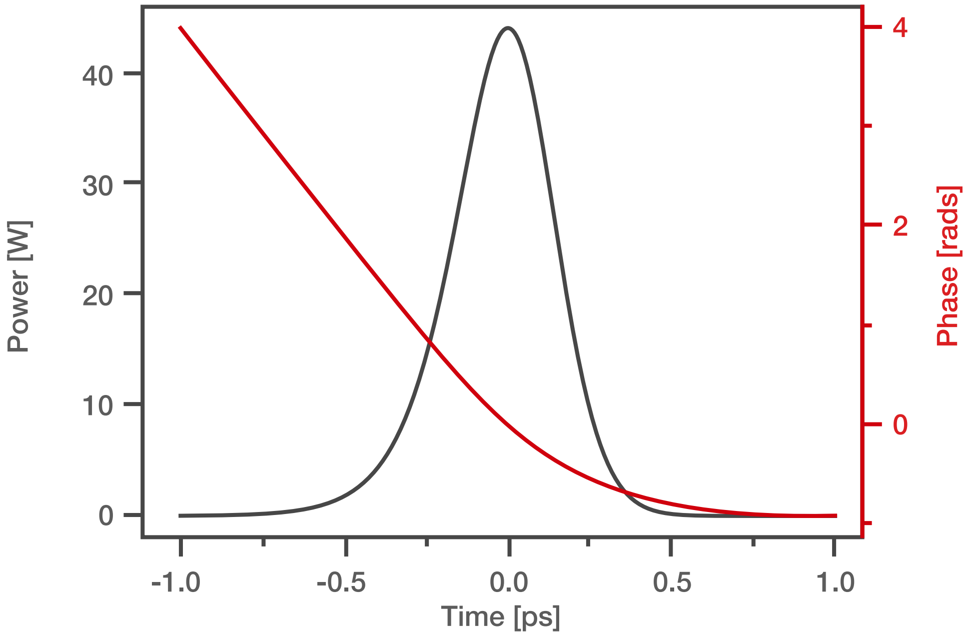

Figure 5.4: The steady state temporal profile of the pulse simulated using the parameters listed in table 5.1. The temporal phase of the pulse is shown in red.

The final temporal profile of the pulse, and its associated spectral phase, is shown in fig. 5.4. The characteristics of the steady state are listed in table 5.2 and compared to the published results of Sieber *et al.* Differences between the pulse characteristics published by Sieber et al and those presented here could be entirely explained by a difference in resolution (table 5.1). As demonstrated in fig. 5.1, increasing the resolution of the simulation reduces the fluctuations in the steady state values and also reduces the calculated pulse duration. The results presented here demonstrate that this model produces simulation results that are consistent with the published work of Sieber *et al.*

5.3 Full-Window Model

In order to address the limitations of a small pulse-centred window in representing laser noise in a physically realistic way, the temporal window is expanded to simulate an entire round trip of the laser cavity. In the full-window approach the time window is set by the cavity length and the boundary conditions are continuous. There is no longer a need to recentre the pulse each round trip as, if the pulse hits the edge of the time window, it reappears at the opposite end of the temporal array.

Sufficient temporal resolution is achieved by increasing the number of array points used to represent a single round trip. For a 1 GHz cavity, the number of points required to achieve a resolution below 10 fs is 2^{16} points. The increased array size significantly increases the computational load of the temporal operators for which iteration over the temporal array is unavoidable. Such simulations would not be practical to run without code acceleration. By compiling the code representing the temporal operators using cython, the computation time is reduced from tens of hours to tens of minutes on a standard desktop computer.

Increasing the time window by such an extent significantly increases the spectral resolution of the simulation to the point where the frequency array is modal, i.e. each point in the frequency array represents a single cavity mode.

All of the operators are unchanged from modelling a small pulse-centred window.

5.3.1 Results

The model was used to simulate the set of parameters listed in table 5.1. The temporal profile of the pulse after 30 000 round trips is compared to the temporal profile calculated using the small pulse-centred window in fig. 5.5. The temporal profile from the full window model (black) is slightly lower power than from the small window model (blue). This is to be expected as the addition of noise in the cavity will take away some of the energy from the pulse. The phases from both simulations match in the centre of the pulse where the amplitude is very much greater than the noise which has random phases. In the wings of the pulse the amplitude of the noise is proportionally greater and causes the phase profile from the full window simulation to diverge from the noise free small window simulation.

The evolution of the temporal and spectral profiles are shown in fig. 5.6 and fig. 5.7 respectively. The build up from noise exibits some of the characteristics of OPSL transient behavior that has been observed experimentally [66, 67]. The temporal evolution of the intracavity power is typical of a system with modes oscillating with random phases [28]. Once the pulse begins to form, the noise within the cavity is suppressed. The pulse travels backwards in time within the cavity. This time shift each round trip causes the repetition rate of the laser to deviate from the nominal value of f_{rep} predicted by dividing the speed of light by the round trip distance. The deviation in the repetition frequency of the laser compared to the nominal value is dominated by the temporal effects of the saturable gain and absorption. Gain acts to amplify the leading edge of the pulse more than the tail edge as the energy stored in the gain depletes on the time scale of the pulse. Conversely, the absorber attenuates the front edge of the pulse pushing the pulse backward in time. The net temporal shift applied to the pulse each round trip is determined by the relative recovery of the gain and the absorber between interactions with the pulse.

In the frequency domain, spectral condensation can be observed in the period before the pulse is formed. Statistical analysis has shown that a narrower spectrum is more likely to produce a noise spike capable of saturating the absorber and forming a pulse [28, 67]. As the pulse forms there is a frequency shift caused by the linewidth enhancement factors.

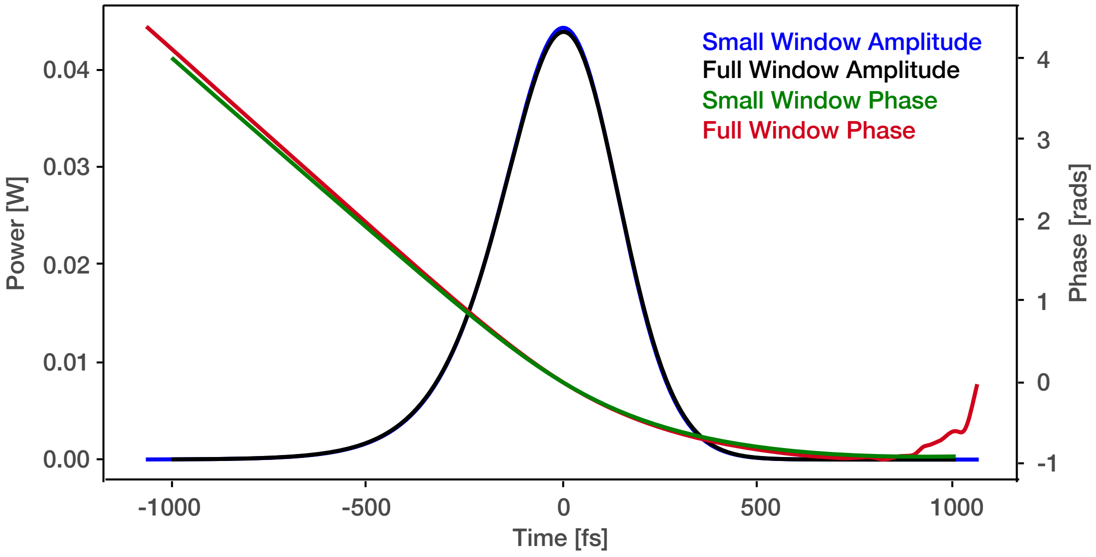

Figure 5.5: The temporal profile and phase of the pulse simulated in a time window equal to the round trip time of the cavity after 30 000 round trips (black and red respectively) compared to the steady state solution from fig. 5.4 (blue and green). The simulation parameters used for both simulations are listed in table 5.1.

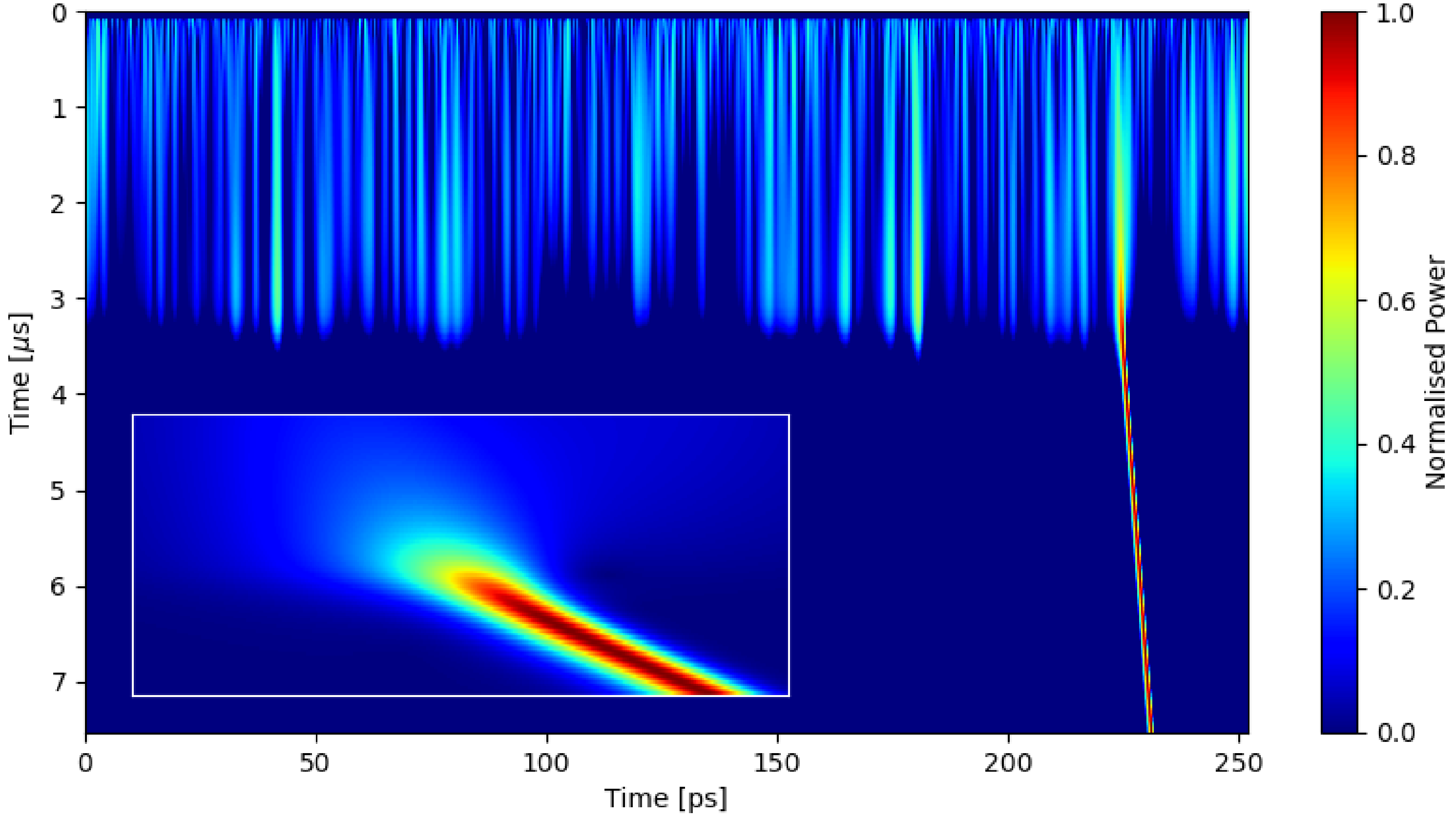

Figure 5.6: Full window simulation of the laser parameters listed in table 5.1. For ease of readability in a printed form $\log_{10}(A(t))$ is plotted. The oscillations in the early build up are tyical of a system of modes oscillating with random phases [28]. The “strobing” of the pulse is due to the rastering of the image when it is saved. A(t) around the emergence of the pulse is inset showing that a pulse with a smooth temporal profile is formed after ~3 µs.

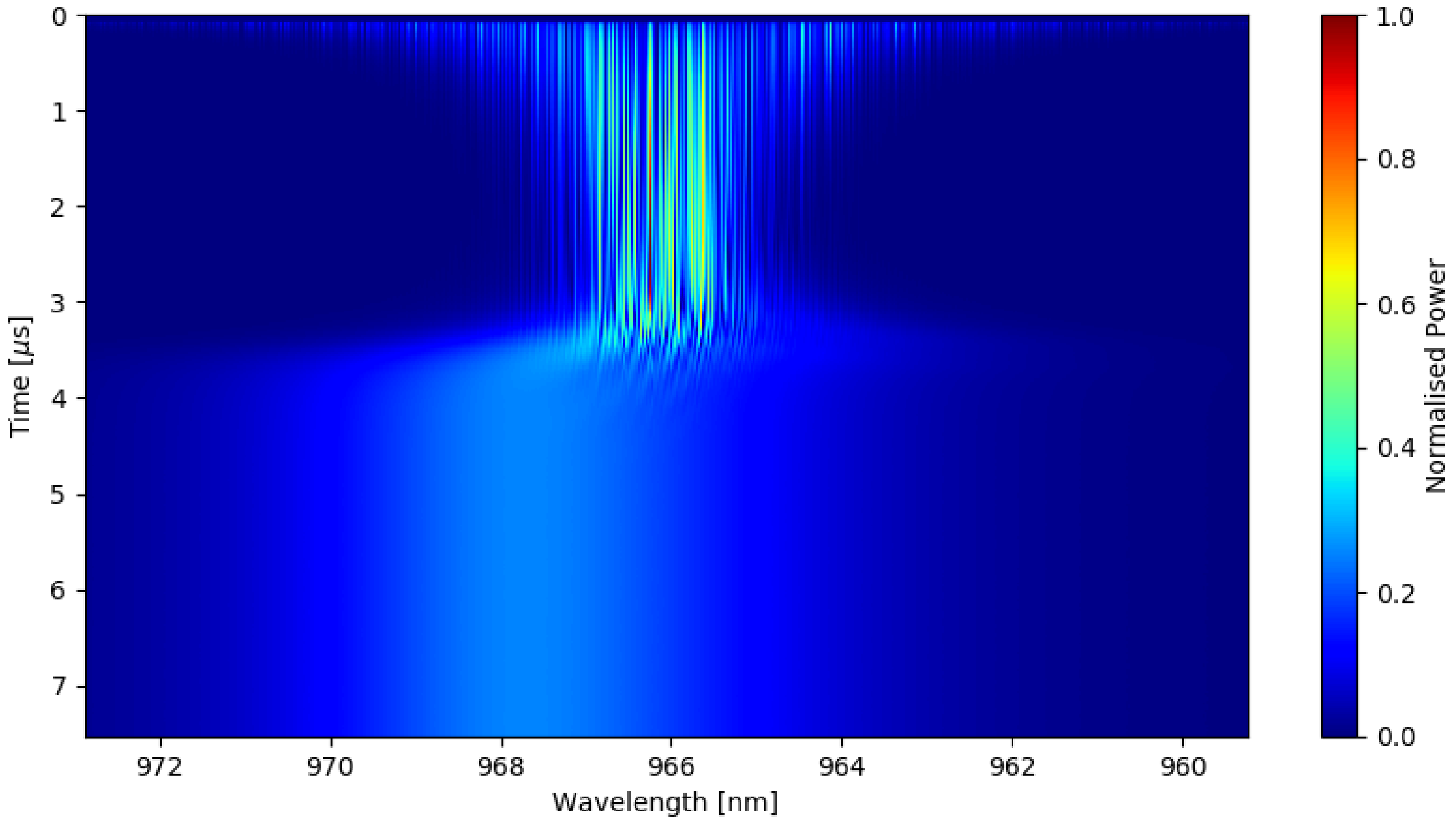

Figure 5.7: The spectral evolution of the laser parameters listed in table 5.1. The initial wide spectrum of the laser narrows over time due to the spectral filtering of the gain. As the spectrum narrows there is an increased chance of a noise spike saturating the absorber [28, 67]. As the pulse forms, the phase shifts relating to the gain and the absorption cause the a spectral shift to longer wavelength.

5.4 Normalised Model

The implementation of the model described in section 5.2 has 16 parameters. Exploring a 16 dimensional parameter space is computationally intensive: simulating just three values for each of the parameters would equate to over one hundred million parameter sets. To make the parameter space smaller, it is desirable to normalise the model, eliminating parameters wherever possible. To this end, three values can be normalised: energy, time and gain/loss. By relating all laser parameters to the gain, number of parameters can be reduced from 16 to 12.

Interactions with the gain and the SESAM in the cavity are calculated in terms of the respective saturation energy of each component. The saturation energies are calculated using the saturation fluence of each cavity element and the size of the cavity mode on the element. By iterating over saturation energies directly the model can be generalised, eliminating two parameters.

The saturation energy of the absorber and the energy within the cavity can be expressed relative to the saturation energy of the gain. The gain saturation energy is now taken to be unity, removing a parameter. In a similar way, the time coefficients for the SESAM recovery and the round-trip-time of the cavity can be expressed in terms of the gain recovery time, eliminating another parameter.

The gain and loss of the system can be generalised so that the total loss is stated as a fraction of the gain and the saturable loss as a fraction of the total loss.

The width of the gain filter depends on both the gain bandwidth and the small signal gain. For simplicity of covering the parameter space the filter width is entered as an independent variable.

To look for general trends, we can relax the convergence criteria and drop the temporal resolution to speed up run time. To simplify the reuse of previously calculated results, the parameter space is discretised. A resolution is applied to each parameter so that each scan is aligned to a 12 dimensional grid of points. Scan results are stored in an

SQlite database. In this way parameter scans can make use of previous simulations to improve efficiency.

Figure 5.8 shows the colour maps representing the relative change of the pulse duration, pulse energy, time bandwidth product, spectral width and peak power in normalised units as a function of the total loss as a fraction of the gain and the proportion of the loss which is saturable. The plots extend to the theoretical physical limit of loss being equal to the gain and for an idealised cavity in which there are no non-saturable losses.

Higher powers are achieved when the saturable loss is a larger proportion of the total losses in the cavity. Pulse energy is greatest with very low total losses, whereas peak power is maximised with a total loss that is between 0.2 and 0.4 times the gain. Pulse duration is inversely correlated with spectral width. For the shortest pulses and the widest spectra, the loss and the fractional saturable loss must be maximised with respect to the gain. Figure 5.8e shows that the variation in the time bandwidth product over the scan parameters is much more complex. The smallest time bandwidth products occur in an arced region near the top left-hand corner of the plot.

The normalised model provides a much more efficient method of identifying trends between the model parameters and the corresponding simulation results.

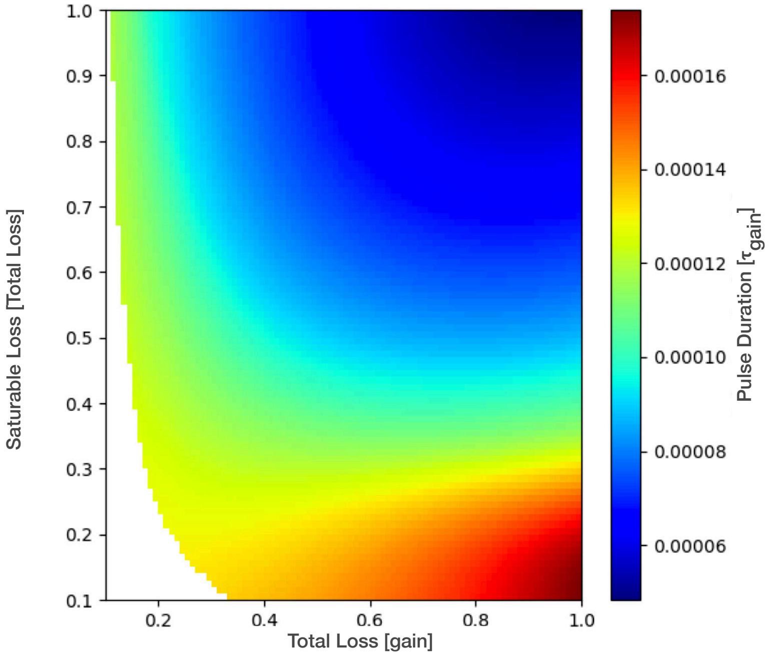

(a) Pulse duration expressed as a fraction of the gain recovery time.

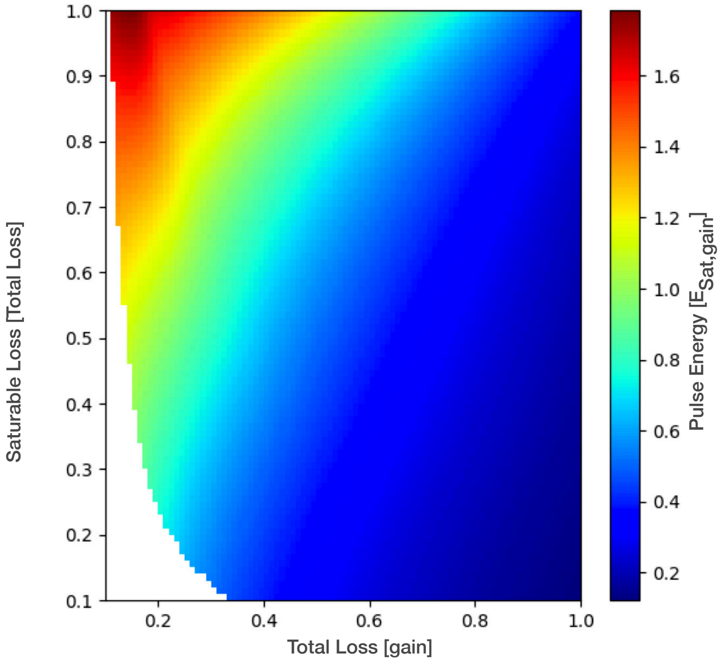

(b) Pulse energy expressed as a fraction of the gain saturation energy.

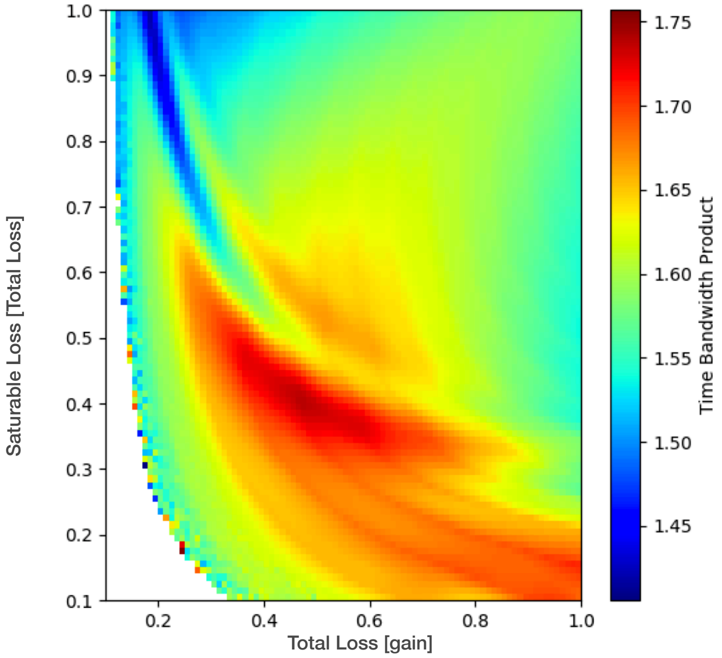

(c) The time bandwidth product of the steady state pulse. An additional mask has been applied on this figure only to remove points on the edge of the stability region with time bandwidth products greater than 1.8. This mask reduces the range of values that the colour scale represents and improves contrast for the unmasked parts of the plot.

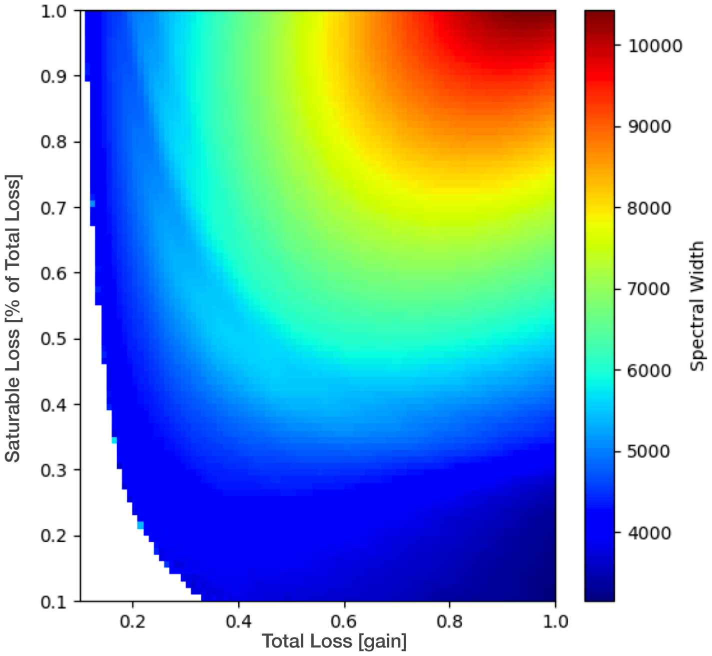

(d) The spectral width of the steady state pulse. The units are the reciprocal of normalised time which is measured in relation to the gain recovery time.

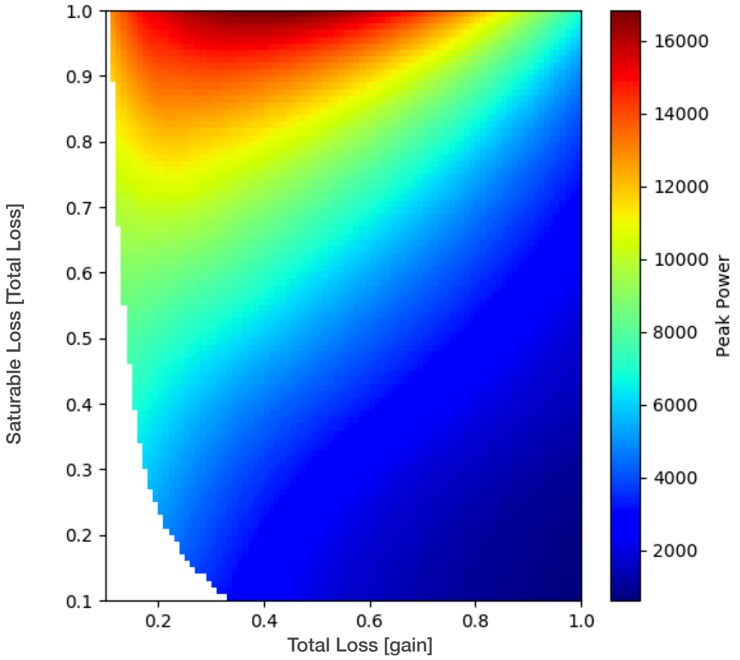

(e) Peak power in normalised units relating to the fraction of the gain saturation energy emitted in the gain recovey time.

Figure 5.8: Parameter maps showing the variation of the pulse duration, pulse energy, time bandwidth product, spectral width and peak power as a function of the loss as a fraction of the gain of which a proportion is saturable. The white regions on the plots correspond to parameters for which a steady state solution was not found.

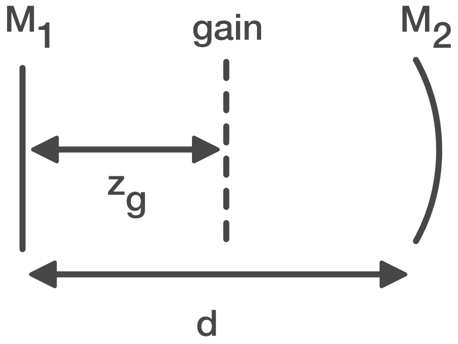

Figure 5.9: Formalism for mathematically describing a V-cavity. The position of the gain is specified in relation to the overall cavity length, d. The total length of the cavity must be less than the radius of curvature of the curved mirror (M_2) for the cavity to be stable.

5.5 Nonlinear Lensing

For simplicity of implementation we assume that the non-linear lensing acts like a Kerr lens, with an instantaneous intensity dependent change in the refractive index. We calculate the perturbations to the intracavity beam of a OPSL for a Kerr lens at the position of the gain chip, z_g using ray transform matrices.

We will consider first the simplest case of a hard aperture in front of the curved mirror in a V-cavity. We ignore the effect of the change in beam radius at the gain and SESAM keeping the saturation energies for both gain and absorption constant throughout the simulation.

The focal length of a Kerr lens is given by

$$f_{\text{Kerr}} = \frac{\pi w^4}{4 n_2 P l} \tag{5.19}$$

where l is the thickness of the Kerr medium, n_2 is the non-linear refractive index of the material, w is the $1/e^2$ radius of the beam at the Kerr medium. The radius of the non-linear cavity mode is both a function of the intracavity position z and the intracavity power, P:

$$w(z, P).$$

We define the V-cavity according to the length of the cavity, d, the position of the gain in relation to the flat end mirror, z_g, and the radius of curvature of the curved mirror, R, as shown in fig. 5.9.

A single round trip of the cavity is represented by the matrix

$$\begin{bmatrix} A & B \\ C & D \end{bmatrix} = \begin{bmatrix} 1 & d \\ 0 & 1 \end{bmatrix} \begin{bmatrix} 1 & 0 \\ -\frac{2}{R} & 1 \end{bmatrix} \begin{bmatrix} 1 & d \\ 0 & 1 \end{bmatrix}.$$

From this matrix we can determine the Rayleigh range of the cavity for $P = 0$:

$$z_0 = \sqrt{d\,(R-d)}. \tag{5.20}$$

To describe the cavity for a non-zero power we must include a lens at the gain chip. The ABCD matrix describing a single round trip of the cavity is then

$$\begin{bmatrix} A & B \\ C & D \end{bmatrix} = \begin{bmatrix} 1 & z_g \\ 0 & 1 \end{bmatrix} \begin{bmatrix} 1 & 0 \\ -\frac{1}{f_k} & 1 \end{bmatrix} \begin{bmatrix} 1 & d-z_g \\ 0 & 1 \end{bmatrix} \begin{bmatrix} 1 & 0 \\ -\frac{2}{R} & 1 \end{bmatrix} \begin{bmatrix} 1 & d-z_g \\ 0 & 1 \end{bmatrix} \begin{bmatrix} 1 & 0 \\ -\frac{1}{f_k} & 1 \end{bmatrix} \begin{bmatrix} 1 & z_g \\ 0 & 1 \end{bmatrix}.$$

To determine the radius of the stable intracavity mode, this matrix must be solved iteratively for the Rayleigh range of the cavity. Using the Rayleigh range given by eq. (5.20) the beam radius at the gain chip is calculated. This nominal beam radius is then used to calculate the intensity at the gain chip and the strength of the lens. The lens strength is then inserted into the cavity matrix giving a new Rayleigh range and an new beam radius at the gain which in turn changes the lens strength. This calculation is repeated until the change in the Rayleigh range between subsequent iterations of the calculation is small. An example convergence is shown in fig. 5.10 calculated for a V-cavity with R = 150 mm, d = 0.9994R, $z_g = 1.5z_0$ (eq. (5.20)) and power, P = 10 kW. A power of 10 kW is chosen, as it is the peak power of a 1 ps pulse in a 1 GHz cavity emitting 100 mW average output power with a 1 % output coupler. The non-linear refractive index used in the calculations is taken to be $-1 \times 10^{-12}\,\mathrm{cm^2\,W^{-1}}$ with

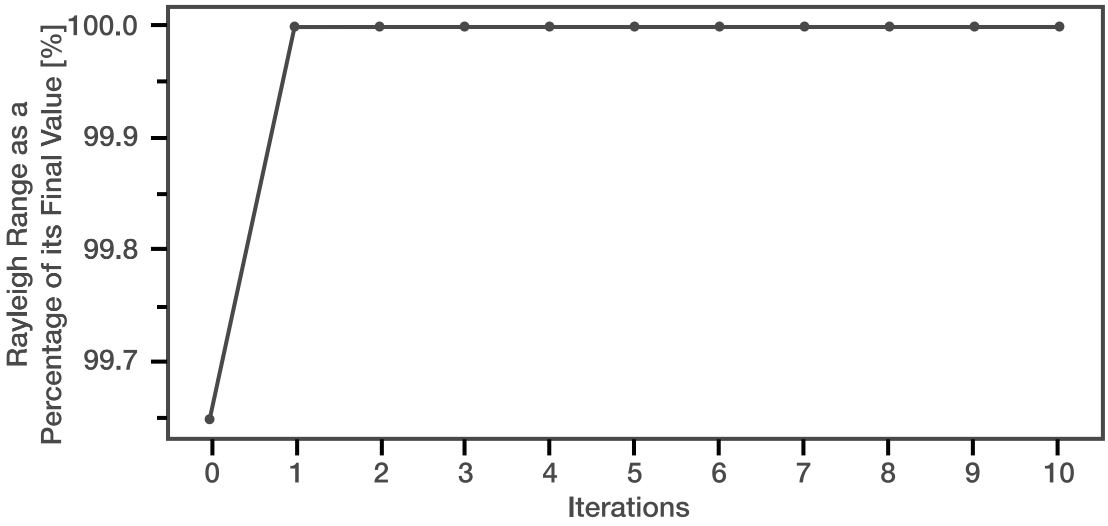

Figure 5.10: The Rayleigh range of a V-cavity with a non-linear lens in the gain sample. The adjusted Rayleigh range is calculated iteratively and converges to a steady value which represents a stable intracavity mode. 1 iteration is sufficient to calculate the adjusted Rayleigh range to within one thousandth of a percent of the steady state value. In subsequent calculations, 2 iterations are used to balance computational accuracy and computational efficiency.

a sample thickness of 4 µm. This is the same power and non-linear refractive index considered in the published work of Albrecht *et al* [56]. We note that the analysis here does not agree with the equations for the change in beam radius reported in reference 56. Only a partial derivation has been published in reference 56 and we are unable to follow their formalism.

The fraction of the power of a Gaussian beam with radius w transmitted through a circular aperture of radius r_a, is given by

$$S = 1 - \exp\left[\frac{-2r_a^2}{w^2}\right]. \tag{5.21}$$

We shall specify an intra cavity aperture in terms of the occlusion to the cavity mode when the focal length of the non-linear lens $f_{\mathrm{NL}} = \inf$, occlusion, $\mathrm{O} = 1 - S$.

The fraction of the power that is initially lost due to the aperture is given by:

$$O = \exp\left[\frac{-2r_a^2}{w(z,0)^2}\right]. \tag{5.22}$$

The small signal gain imposes an upper limit on the aperture-induced loss that can be tolerated by the laser. Although the aperture can be further reduced in size once the laser is running it would not be self-starting as the total loss would be greater than the gain and for this reason it is not considered in this analysis.

The change in beam radius for a given intracavity power and position within the cavity,

$$\Delta w(z, P) = \frac{w(z, P) - w(z, 0)}{w(z, 0)}. \tag{5.23}$$

$\Delta w(d, 10\,\mathrm{kW})$ is plotted as a function of cavity length, d, and the position of the gain within the cavity, z_g (as defined in fig. 5.9) in figs. 5.11 and 5.12. The loss as a function of power for a V-cavity with an initial aperture loss of 4 % is shown in fig. 5.13. The radius of curvature is 150 mm, d = 149.9 mm and $z_g = 1.25 z_0$. The loss is only modulated by 0.15% for a 10 kW peak power which suggests that this cavity is a poor candidate for self-modelocking. When simulating this cavity using the small pulse-centred window model, starting with a pulse with a peak power of 10 kW, the pulse was unstable and collapsed.

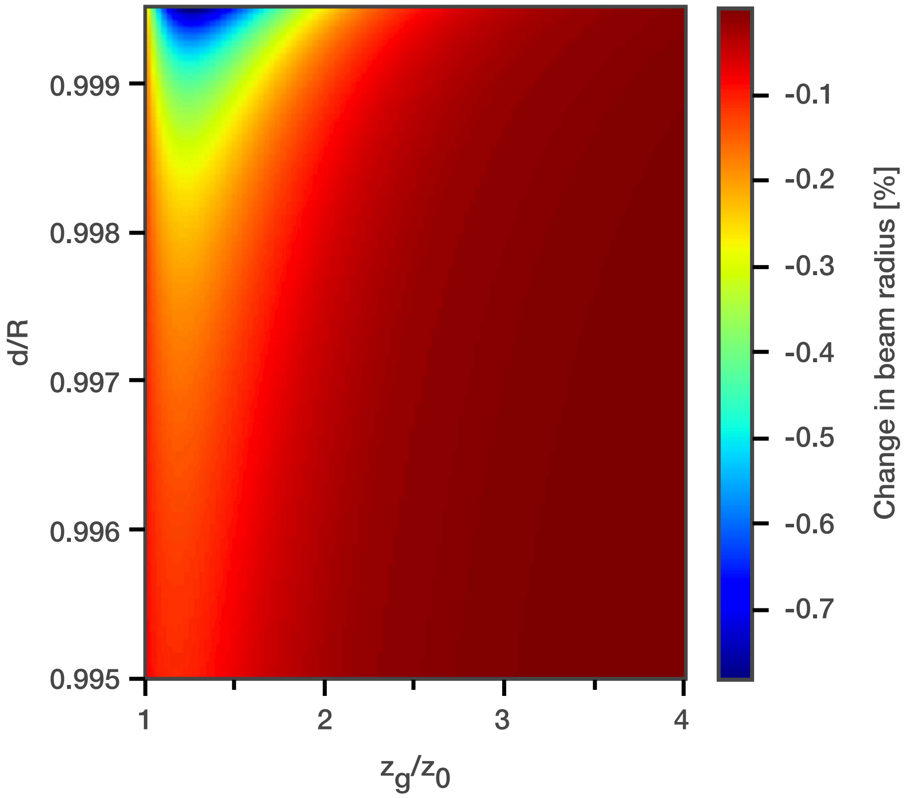

Figure 5.11: The change in beam radius Δw at an aperture placed in front of the curved end mirror of a V-cavity. A negative change in beam radius indicates that the radius of the cavity-mode is reduced. Δw is plotted as a function of the relative cavity length and the position of the gain relative to the Rayleigh range. The radius of curvature of the end mirror R = 150 mm. The peak change in beam radius for a given cavity length occurs when the gain chip is placed at $1.25z_0$.

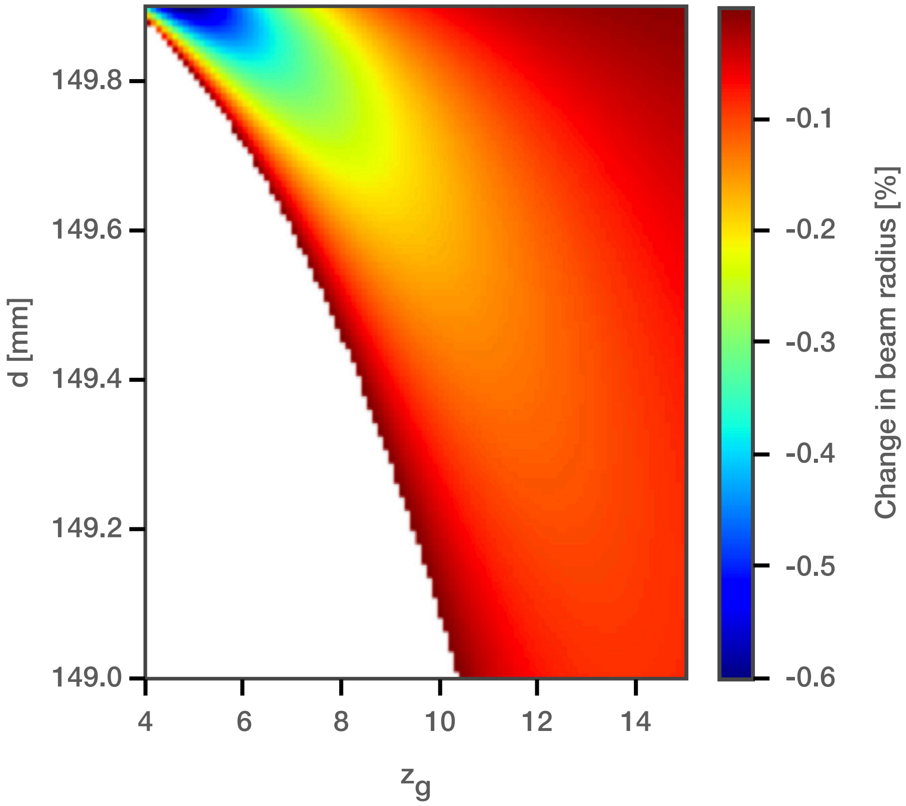

Figure 5.12: The change in beam radius at an aperture placed in front of the curved end mirror of a V-cavity. A negative change in beam radius indicates that the radius of the cavity-mode is reduced. The radius of curvature of the end mirror, R = 150 mm. The position of the gain sample and the length of the cavity are varied. The area for which there was a positive change in beam radius was masked off as it is not compatible with modelocking.

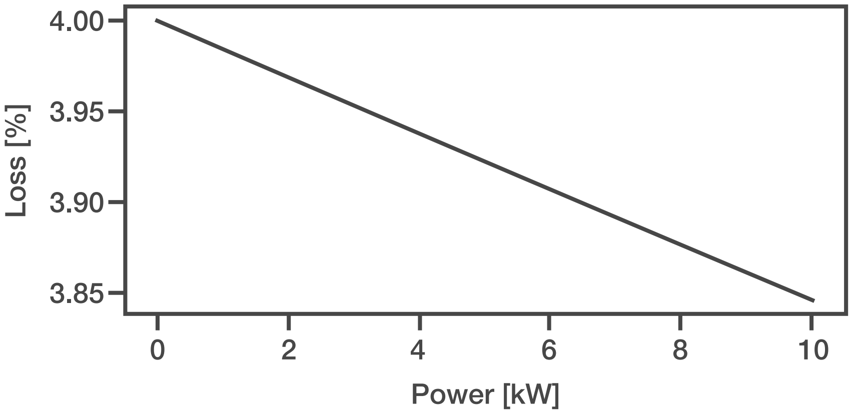

Figure 5.13: Loss as a function of power for an aperture placed in front of the curved mirror of a V-cavity where R = 150 mm, d = 149.9 mm and $z_g = 1.25 z_0$.

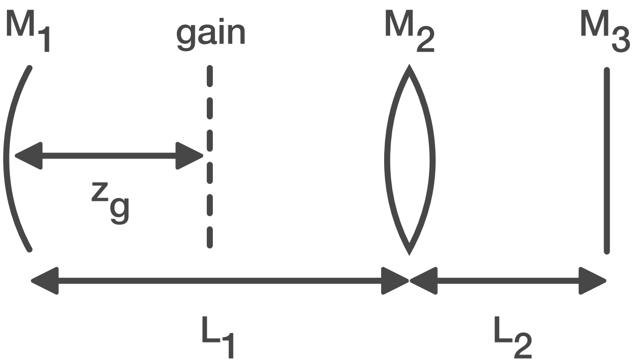

Figure 5.14: Formalism for defining a z-cavity. M_1 and M_2 are curved mirrors with radii of curvature R_1 and R_2 respectively. M_3 is a flat cavity mirror or a SESAM.

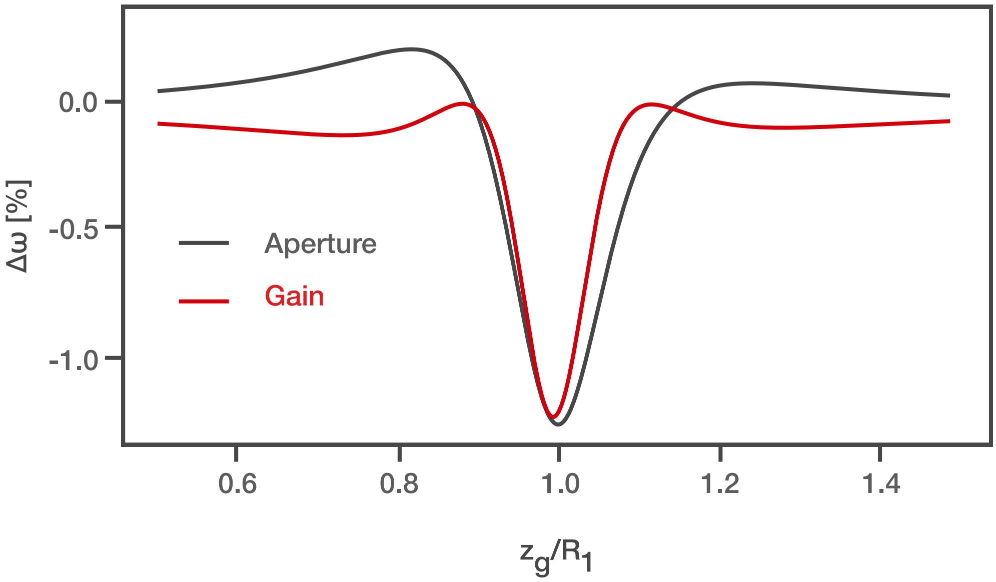

Figure 5.15: Change in beam radius (Δw) at the flat end mirror of a z-cavity where: $L_1 = 74\,\mathrm{mm}$; $L_2 = 20\,\mathrm{mm}$; M_1 and M_2 are mirrors with a radius of curvature of 50 mm. As the cavity tends towards the stability limit, the gain position that gives the peak change in beam radius tends towards $z_g = R_1$.

5.5.1 Non-Linear Lensing in a Z-Cavity

We define a z-cavity with three mirrors: M_1, M_2 and M_3 as shown in fig. 5.14. M_1 and M_2 are curved mirrors with radii of curvature R_1 and R_2 respectively. M_3 is a flat cavity mirror or a SESAM. Two cavity arms of length L_1 and L_2 separate the three mirrors. The gain is positioned at a distance z_g from M_1 within the cavity.

Change in beam radius (Δw) at the flat end mirror of a z-cavity, where: $L_1 = 74\,\mathrm{mm}$; $L_2 = 20\,\mathrm{mm}$; M_1 and M_2 are 50 mm radius of curvature mirrors, is shown in fig. 5.15.

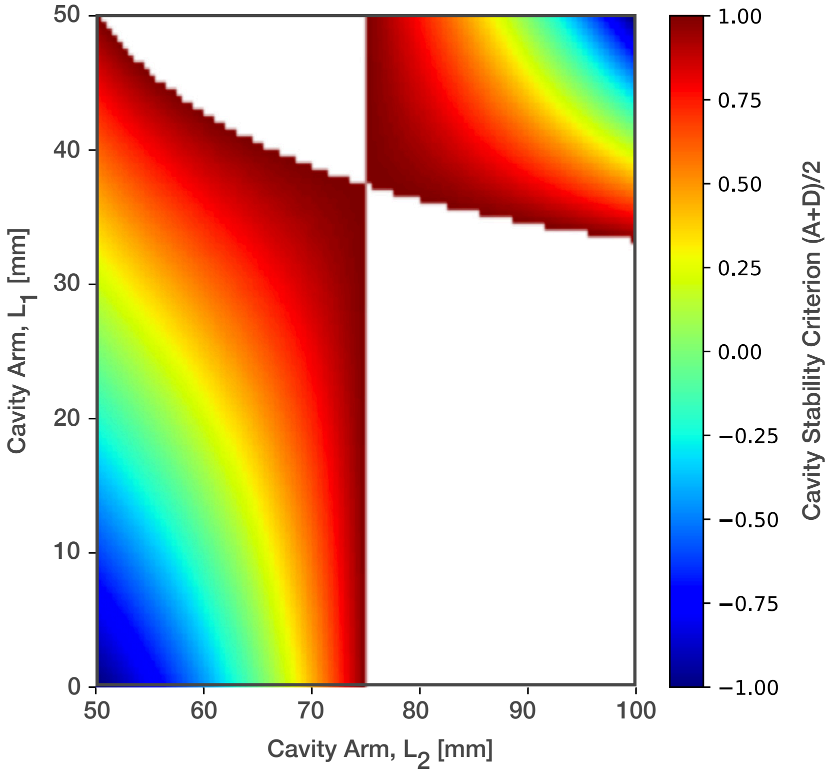

Figure 5.16: Variation in the cavity stability parameter for a z-cavity as defined in fig. 5.14 as a function of the lengths of the two cavity arms, L_1 and L_2. The radii of curvature of both of the cavity mirrors R_1 and R_2 is 50 mm.

As the cavity tends towards the stability limit, the gain position that produces the peak change in beam radius tends towards $z_g = R_1$. z_g will be set equal to R_1 for all subsequent calculations.

The ABCD matrix representing a cavity round trip for $P = 0$ is

$$\begin{bmatrix} 1 & L_2 \\ 0 & 1 \end{bmatrix} \begin{bmatrix} 1 & 0 \\ -\frac{2}{R_2} & 1 \end{bmatrix} \begin{bmatrix} 1 & L_1 \\ 0 & 1 \end{bmatrix} \begin{bmatrix} 1 & 0 \\ -\frac{2}{R_1} & 1 \end{bmatrix} \begin{bmatrix} 1 & L_1 \\ 0 & 1 \end{bmatrix} \begin{bmatrix} 1 & 0 \\ -\frac{2}{R_2} & 1 \end{bmatrix} \begin{bmatrix} 1 & L_2 \\ 0 & 1 \end{bmatrix}$$

Using eq. (2.4), the stability regions can be calculated. Figures 5.16 and 5.17 show the stability criteria for z-cavities with $R_1 = 50$ mm and $R_2 = 50$ mm and 25 mm respectively. We consider the regions in the lower left-hand quadrants of the stability plots as the stability criteria tends towards 1.

The change in beam radius as a function of the cavity geometry is calculated using the same iterative method that was applied to the V-cavity. Figure 5.18 shows the change

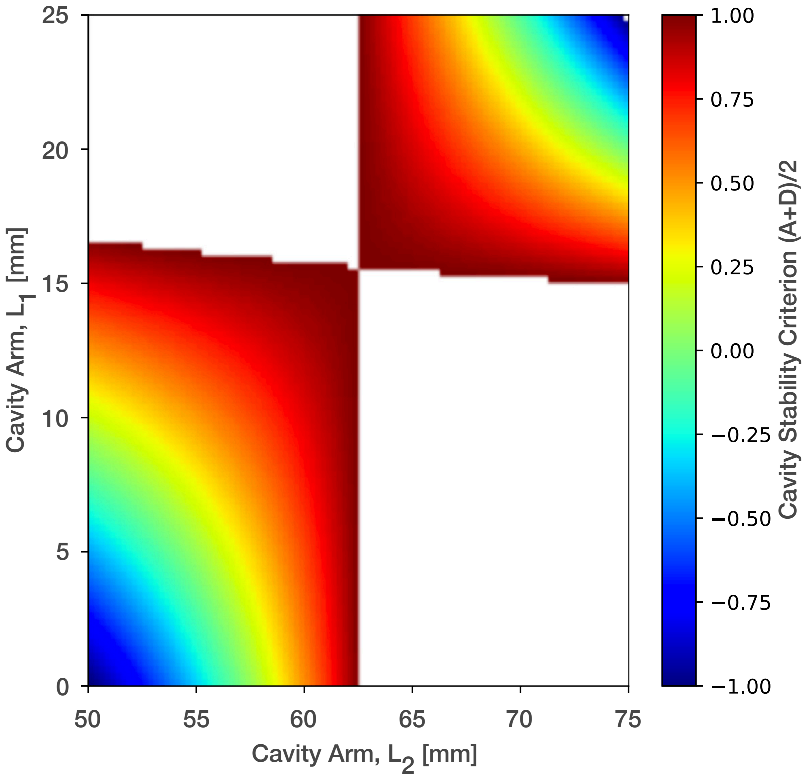

Figure 5.17: Variation in the cavity stability parameter for a z-cavity as defined in fig. 5.14 as a function of the lengths of the two cavity arms, L_1 and L_2. The radius of curvature of the cavity mirror $R_1 = 50$ mm and $R_2 = 25$ mm.

in beam radius as a function of the cavity lengths L_1 and L_1 for a Z-cavity in which $R_1 = R_2 = 50$ mm for a power of 10 kW. Over a 1 mm change in the length of L_1, Δw changes from ∼1 % to 16 %. This is a change of more than an order of magnitude greater than the same translation range at the edge of stability in a V-cavity.

It can be seen from fig. 5.18 that Δw is independent of the length L_2. Taking an arbitrary value for L_2 we can compare Δw measuring from the edge of stability of L_1 for $R_2 = 50$ mm and $R_2 = 25$ mm, shown in fig. 5.19. The change in the beam radius as a function of the distance from the edge of the cavity stability is remarkably similar for both the 25 mm and the 50 mm radius of curvature mirrors. This has important practical implications when considering the possible effect a non-linear lens could have on a SESAM modelocked OPSL as the ratio of the radii of the intracavity mode on the gain and the absorber can be varied by changing the cavity mirror R_1 without changing the susceptibility of the cavity to a non-linear lens.

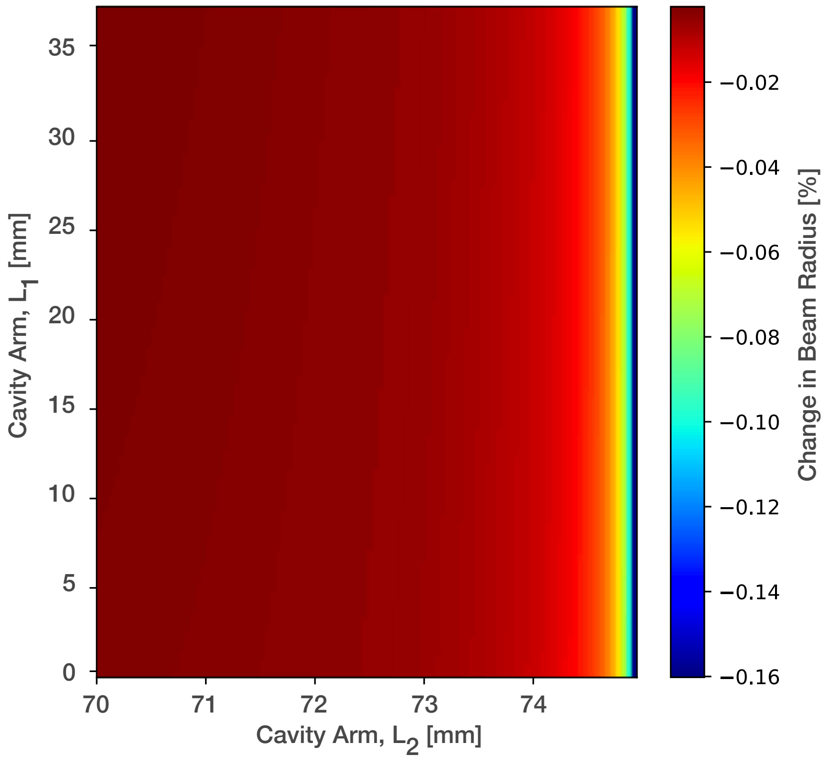

Figure 5.18: Change in beam radius at the aperture in front of the flat cavity mirror M_3 in a z-cavity (fig. 5.14) as a function of the lengths of the two cavity arms, L_1 and L_2. Both cavity mirrors have a radius of curvature of 50 mm.

5.5.2 Simulation Results

Non-linear lensing is first added to a model with a small pulse-centred window, initialised with a pulse of duration 1 ps and peak power of 1 W. The simulation parameters used were based on those listed in table 5.1 but with the losses changed. Saturable absorption was removed and the total non-saturable losses, including the output coupling, were reduced to 0.5 %. The occlusion due to the aperture was set at 3 % whilst the gain remained at 5 %.

The cavity being modelled was a Z-cavity with the radius of curvature of the cavity mirrors R_1=R_2=50 mm. The cavity arm L_1=74 mm and the cavity arm L_2=30 mm. The gain was placed at the focus of R_1.

The temporal evolution of the pulse is shown in a series of plots shown in fig. 5.20. The first plot shows the pulse profile after 4000 round trips have been simulated. The

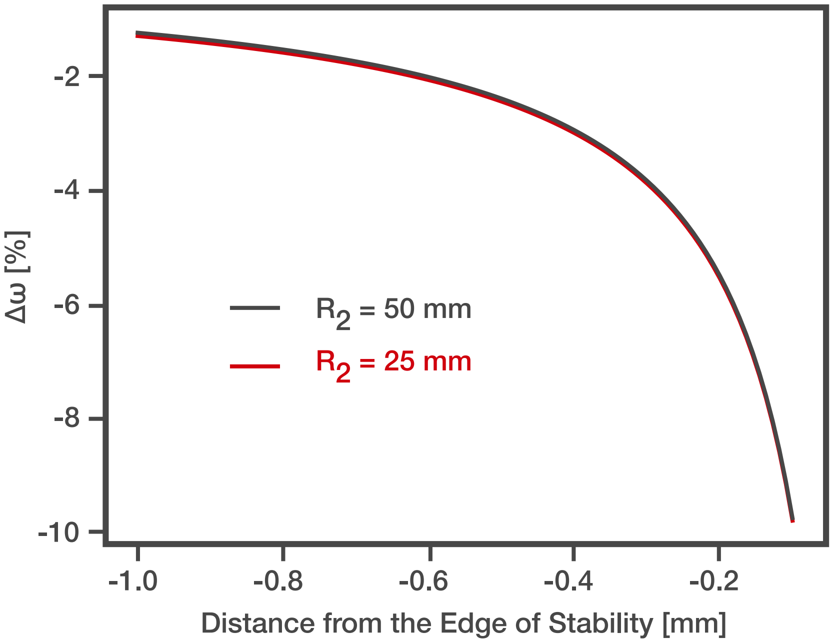

Figure 5.19: The change in beam radius at the aperture of two Z-cavities are compared. In both cases the radius of curvature of cavity mirror $M_1 = 50\,\mathrm{mm}$. As shown by fig. 5.18, the change in beam radius is insensitive to the length of the cavity arm L_2. The length used is chosen arbitrarily to explore the lower left-hand stability region in fig. 5.16 and fig. 5.17. Δw is plotted with respect to the distance in mm from the value of L_1 at the edge of cavity stability.

action of the non-linear lens has shortened the pulse to less than 300 fs and the pulse has been amplified to a peak power of greater than 10 kW. A small pulse has also started to split off from the trailing edge of the pulse. This sub-pulse forms a second pulse in the cavity but at a lower power than the initial pulse. As the second pulse grows in power the primary pulse loses energy and power and its pulse duration increases. In turn the secondary pulse splits and a third pulse forms before both the second and third pulses are subdivided. The temporal instability shown in figure fig. 5.20 is typical of all simulations run from a 1 ps pulse in a small temporal window. Extending the cavity arm L_1 towards the edge of stability delays the formation of sub-pulses but does not prevent them from forming.

In fig. 5.21 the same laser is modelled in the manner described above but with the addition of 1 % of saturable absorption. The saturable absorption reduces the net gain in the time period following the pulse, preventing sub-pulses from forming.

The same simulation with the occlusion reduced to 0 % produced a pulse of duration

220 fs but with a lower peak power of 7 kW. The non-linear lens acts to lengthen 220 fs pulses but does lead to increased peak power and pulse energy.

All three simulations were run again, with a time window equal to a cavity round trip. After 30 000 round trips a pulse had not formed in either cavity with 3 % occlusion with or without saturable absorption. With 0 % occlusion and 1 % saturable absorption a pulse formed within the cavity after 12 000 round trips.

5.5.3 Conclusions

The examples presented here do not represent an exhaustive exploration of the parameter space. The susceptibility of an SML OPSL to temporal pulse instabilities even in the absence of simulated noise suggests that engineering an SML cavity would be challenging. SESAM stabilised SML OPSLs are a promising avenue for exploration. It is not clear whether adding a hard aperture to a SESAM-ML-OPSL at the edge of the cavity stability could enable the formation of pulses with record low pulse durations. However, a non-linear lens could help maintain sub-picosecond pulses whilst requiring less power to be absorbed by the SESAM. As post-processing of surface recombination SESAMs to improve their thermal handling is a technical challenge, reducing the thermal load by utilising a secondary pulse shortening effect could be beneficial and presents a possible avenue for power scaling sub-picosecond OPSLs.

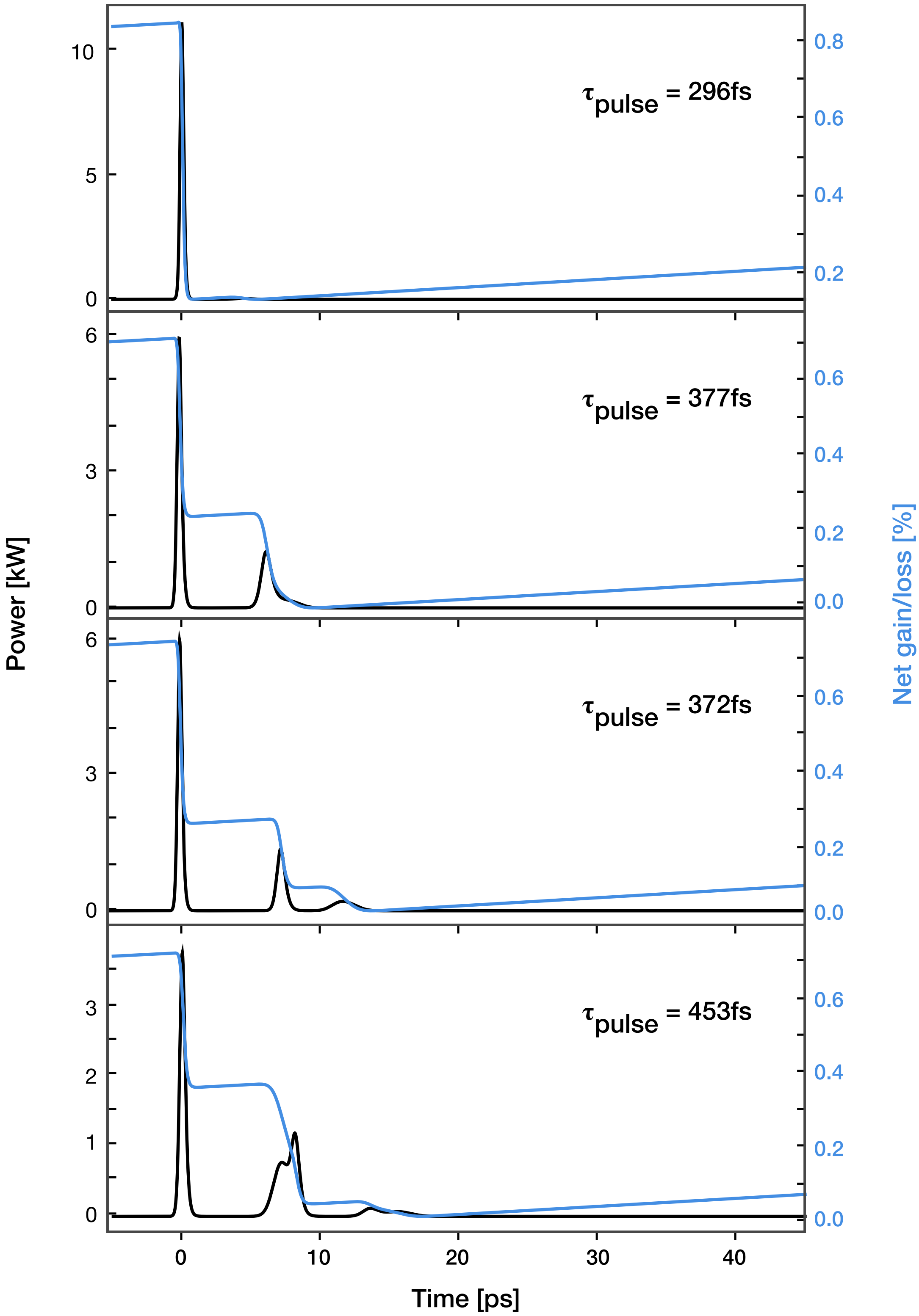

Figure 5.20: Temporal profile of the intra-cavity power of a z-cavity with 5 % gain, 0.5 % non-saturable loss and 3 % occlusion from an aperture in front of cavity mirror M_3. The simulation was initialised in a 50 ps time window with a 1 ps pulse with a peak power of 1 W. The temporal profile of the intracavity power is shown after 4000, 8000, 12 000 and 16 000 round trips respectively.

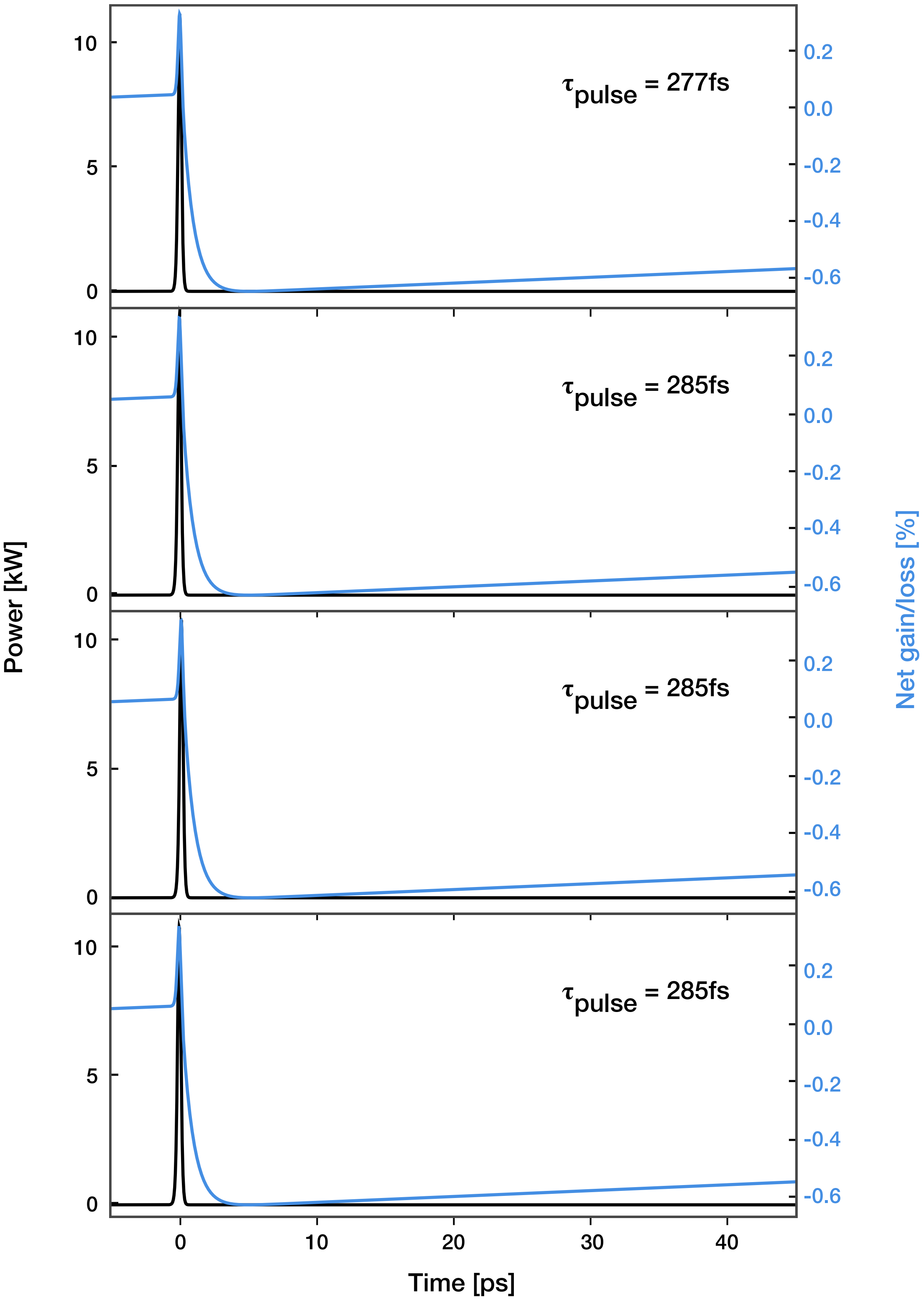

Figure 5.21: Temporal profile of the intra-cavity power of a z-cavity with 5 % gain, 0.5 % non-saturable loss, 1 % saturable loss and 3 % occlusion from an aperture in front of cavity mirror M3. The simulation was initialised in a 50 ps time window with a 1 ps pulse with a peak power of 1 W. The temporal profile of the intracavity power is shown after 4000, 8000, 12 000 and 16 000 respectively.

5.6 Conclusions

The modelling work presented in this chapter has been shown to be consistent with the experimentally verified model published by Sieber *et al.* The model has then been developed to simulate the full cavity round trip of the laser, including a physically realistic implementation of intracavity noise and modal spectral resolution. This provides a platform with which to rigorously test the self-starting and temporal stability of modelocked OPSLs.

The modelling of a small pulse-centred time window has been normalised to enable the efficient simulation of large parameter scans.

The action of a non-linear lens in the gain chip has been simulated in a small pulse-centred window and shown to be temporally unstable for the test parameters. However, the inclusion of a SESAM within the cavity can act to stabilise the pulse in time. When modelling a full cavity round trip of a SESAM stabilised SML OPSL, a set of parameters that produces stable self-starting modelocking has yet to be discovered.

Chapter 6

Conclusions and Future Work

The work presented in this thesis demonstrates the first measurements of the non-linear lens in an OPSL gain structure, on resonance with the QW emission. While the combination of the experimental and computational research strands does not yet definitively show that non-linear lensing can be utilised to improve laser performance, the tools developed through this research have the potential to provide new avenues for this research.

The experimental technique has been developed to be capable of measuring the lens as a function of wavelength. It could be adapted to measure the dependence of the lens strength on the pulse energy and the peak power of the probe beam independently by varying the pulse duration. A lens that was strongly dependent on the pulse energy of the probe beam would indicate that a large component of the lensing effect relates to carrier dynamics in the gain structure. Varying responses from pulses of the same energy, but with different pulse durations, would indicate the time dependence of the lensing effect.

Modelling of modelocked OPSLs has been developed to simulate the full cavity round trip of a laser. This model provides a robust test of self-starting from noise as well as measuring the temporal stability of a modelocked pulse and the laser's susceptibility to multi-pulsing.

Whilst fundamental self-modelocking of an OPSL has not been demonstrated with the model, Kerr-lens modelocking started and stabilised by a SESAM or other saturable absorber appears possible. This represents a promising avenue of research that may be capable of pushing output powers up and pulse durations down.

Ultimately, both the measurements of the lensing and the computational modelling of a SESAM stabilised self-modelocked OPSL could be combined to experimentally verify the implementation of the lens in the model and to then use the model to help optimise laser performance.

Further developments can be made to the model to decrease computation time. Currently the computer model runs on a single computer processing unit (CPU) of a desktop computer. Writing the code for execution on the CPU is simpler to implement and therefore faster to test new ideas and implement improvements. With code acceleration using Cython, the CPU implementation is acceptably fast for single simulations, taking 3 to 10 s to model a single build-up to a steady state. Scans do not take a prohibitively long time to run with a scan over 5 parameters, simulation of over 750 000 parameter sets was completed in about 3 weeks.

Further speed increases in run time could be improved by utilising parallelism on graphics processing units (GPUs). Many of the operators used in the model could be implemented parallel using well established GPU algorithms. The gain and absorption operators cannot be entirely computed in parallel due to the fact that they are inherently causal. Preliminary calculations can be computed in parallel and the final value can be calculated on a GPU by serialising the access to the memory containing the gain or absorption parameter. We have been awarded a grant from NVIDIA of the latest graphics card available, a TITAN XP graphics card with 3840 cores with which to fully optimise this model.

Improving run time would enable us to fully utilise the full window model. Montecarlo simulations could be used to statistically analyse the properties of the transient build up from noise. Longer scans could be performed to test long term stability of the pulse within the cavity.

Therefore, the work conducted in this thesis shows the value of continuing research into non-linear lensing in an OPSL gain structure. While it has not proved possible to show stable, self-starting modelocking build up from noise, the influence of changes caused by a non-linear lens in combination with a hard aperture in the laser cavity suggests that this avenue of research has the potential to expand the use of OPSLs in the future.

Chapter 7

List of Publications

Ed A. Shaw, C. Robin Head, Oliver J. Morris, Andrew P. Turnbull, Keith G. Wilcox, and Anne C. Tropper; “modelocked VeCSELs: High Repetition Rate Pulse Sources for Nonlinear Optics”; 2nd European Workshop on VeCSELs, October 2013 (Poster Presentation).

C. Robin Head, Alexander Heine, Ed A. Shaw (Presenting Author), Andrew P. Turnbull, Peter Unger and Anne C. Tropper; “Femtosecond modelocked VECSEL from Widely CW-Tunable Gain Chips”, Conference on Lasers and Electro-Optics (CLEO) 2014 (Poster presentation).

Ed A. Shaw, Adrian H. Quarterman, Lucy E. Hooper, Peter J. Mosely, and Keith G. Wilcox; “Coherent Spectral Broadening and Compression of the Output of a modelocked VECSEL”, SPIE Photonics West; 2015.

Andrew P. Turnbull, C. Robin Head, Ed A. Shaw, Theo Chen-Sverre, and Anne C. Tropper; “Spectrally Resolved Pulse Evolution in a modelocked Vertical-External-Cavity Surface-Emitting Laser from Lasing Onset Measurements”; SPIE Photonics West; Feb 2015.

Adrian H. Quarterman, Ed A. Shaw, and Keith G. Wilcox; “Carrier-Dependent Nonlinear Lens in a VECSEL Gain Medium”; CLEO Europe, Jun 2015.

Ed A. Shaw, Adrian H. Quarterman, Andrew P. Turnbull, Theo Chen-Sverre; C. Robin Head, Anne C. Tropper, Keith G. Wilcox; “Reflection Z-Scan Measurements of the Nonlinear Lens in VECSEL Gain Structures”; SPIE Photonics West; Feb 2016.

C. Robin Head, Alexander Hein, Andrew P. Turnbull, Markus Polanik, Ed A. Shaw, Theo Chen-Sverre, Peter Unger, Anne C. Tropper; “High-order Dispersion in sub-200-fs Pulsed VECSELs”; SPIE Photonics West; Feb 2016.

Theo Chen-Sverre, C. Robin Head, Andrew P. Turnbull, Ed A. Shaw, Anne C. Tropper, Otto L. Muskens; “Tunable Repetition Rate VECSEL for Resonant Acoustic-Excitation of Nanostructures”; SPIE Photonics West (2016) (Poster Presentation).

Ed A. Shaw, Adrian H. Quarterman, Andrew P. Turnbull, Theo Chen-Sverre, C. Robin Head, Anne C. Tropper, and Keith G. Wilcox; “Nonlinear Lensing in an Unpumped Antiresonant Semiconductor Disk Laser Gain Structure”; IEEE Photonics Technology Letters, Vol. 28, No. 13, (July 2016).

Appendix A

Derivation of the Lens Strength Formula

We start with the known complex beam parameter at the focus, q_0, from characterising the probe beam, where

$$\frac{1}{q_0} = \frac{-i}{z_0}.$$

The complex beam parameter q' at the detection plane is given generally by

$$\frac{1}{q'} = \frac{1}{R'} - i\frac{1}{z'}.$$

Applying eq. (2.3):

$$\frac{z_0 C - iD}{z_0 A - iB} = \frac{1}{R'} - i\frac{1}{z'}$$

To find z' and therefore w' we need to take the imaginary part of the LHS. Multiplying the top and bottom by the complex conjugate of the denominator we get

$$\frac{(z_0 C - iD)(z_0 A + iB)}{(z_0 A - iB)(z_0 A + iB)} = \frac{\ldots\ + iz_0 BC - iz_0 AD + \ldots}{z_0^2 A^2 + B^2}$$

Therefore

$$z' = A^2 z_0 + \frac{B^2}{z_0}.$$

In order to calculate the relative beam change we consider the propagation to the aperture/object plane of the lensing system with and without a lens present.

Without the lens the ABCD matrix simply represents a propagation over a distance, d:

$$\begin{bmatrix} A & B \\ C & D \end{bmatrix} = \begin{bmatrix} 1 & d \\ 0 & 1 \end{bmatrix}.$$

To include the lens, we require ray transform matrices representing: a propagation distance z from the focus to the lens; lensing by a lens of unknown strength $K = -\frac{1}{f}$ and propagating a distance d-z to the aperture/object plane.

The ABCD matrix from the focus to the aperture is

$$\begin{bmatrix} A & B \\ C & D \end{bmatrix} = \begin{bmatrix} 1 & d-z \\ 0 & 1 \end{bmatrix} \begin{bmatrix} 1 & 0 \\ K & 1 \end{bmatrix} \begin{bmatrix} 1 & z \\ 0 & 1 \end{bmatrix}.$$

Multiplying through

$$\begin{bmatrix} A & B \\ C & D \end{bmatrix} = \begin{bmatrix} 1 & d-z \\ 0 & 1 \end{bmatrix} \begin{bmatrix} 1 & z \\ K & zK+1 \end{bmatrix},$$

$$\begin{bmatrix} A & B \\ C & D \end{bmatrix} = \begin{bmatrix} 1+K(d-z) & z+(d-z)(zK+1) \\ K & zK+1 \end{bmatrix}.$$

We define the relative change in beam diameter $\Delta z = z_a(z)/z_d$ where $z_a(z)$ is the beam radius at the aperture plane after interacting with the non-linear lens at position z and

z_d is the beam size without the lens.

$$\Delta z = \frac{(K(d-z)+1)^2 z_0^2 + (zK+d)^2}{z_0^2 + d^2} \tag{A.1}$$

To obtain a function for K we must rearrange this equation and apply the quadratic formula:

$$K = \frac{-zd - z_0^2 \pm \sqrt{(zd + z_0^2)^2 + (z^2 + z_0^2)(d^2 + z_0^2)(\Delta z - 1)}}{(d-z)(z^2 + z_0^2)}$$

We consider a closed loop representing the extraction of the lens strength for a z-scan measurement. Taking an array of z values and a focussed spot size of w_0 we calculate the strength of the non-linear lens strength K using eq. (5.19). The change in beam radius at a distance d from the focus is then calculated. The lens strength is then calculated using eq. (4.1). The calculated values for $K(z)$ and $dw(z)$ are shown in fig. 4.1.

We then apply eq. (4.1) to the calculated change in beam radius to obtain the extracted lens strength, shown in fig. 4.2. Due to the ± in eq. (4.1), there are two possible values for K for each value of dw. We define the two possible variations of eq. (4.1) as K_{minus} and K_{plus} denoting the use of a minus or a plus respectively. We must switch from K_{minus} to K_{plus} at the position in z where $K_{\text{minus}} = K_{\text{plus}}$, when

$$\sqrt{(zd + z_0^2)^2 + (z^2 + z_0^2)(d^2 + z_0^2)(\Delta z - 1)} = 0,$$

here

$$\Delta z = \frac{1 - (zd + z_0^2)^2}{(d^2 + z_0^2)(z^2 + z_0^2)}.$$

The z dependence of the critical value of Δz, $\Delta z_{\text{critical}}$, must be compared to the measured change in the beam radius as shown in fig. 4.2 to determine the interface between the region of the z-scan curve to apply K_{minus} and K_{plus}.

To determine the uncertainty in the extracted lens strengths we must take the first derivative of eq. (4.1) with respect to Δz and z. The uncertainty in Δz will relate to the numerical fitting of the intensity profile of the beam. The uncertainty in z will relate to the repeatability limit of the translation stage ±4 µm, this uncertainty will be constant across all values of z and will become more significant as $|z|$ aproaches 0.

$$\begin{aligned}\frac{d}{dz}\left(\frac{-zd - z_0^2 + \sqrt{(zd + z_0^2)^2 + (z^2 + z_0^2)(d^2 + z_0^2)(\Delta z - 1)}}{(d-z)(z^2 + z_0^2)}\right) &= \frac{1}{(z_0^2 + z^2)^2(d-z)^2} \\ &\left[(z_0^2 + z^2)(d-z)\left(\frac{z_0^2((\Delta z - 1)z + d) + bd^2z}{\sqrt{((\Delta z - 1)(z_0^2 + d^2)(z_0^2 + z^2) + (z_0^2 + dz)^2}} - d\right)\right. \\ &+2z(d-z)(-\sqrt{((\Delta z - 1)(z_0^2 + d^2)(z_0^2 + z^2) + (z_0^2 + dz)^2)} + z_0^2 + dz) \\ &\left. - (z_0^2 + z^2)(-\sqrt{((\Delta z - 1)(z_0^2 + d^2)(z_0^2 + z^2) + (z_0^2 + dz)^2)} + z_0^2 + dz)\right]\end{aligned} \tag{A.2}$$

$$\begin{aligned}\frac{d}{d\Delta z}\left(\frac{-zd - z_0^2 + \sqrt{(zd + z_0^2)^2 + (z^2 + z_0^2)(d^2 + z_0^2)(\Delta z - 1)}}{(d-z)(z^2 + z_0^2)}\right) = \\ \frac{z^2 + d^2}{2(-z_0 + d)\sqrt{[(z^2 + z_0 d)^2 + (z_0^2 + z^2)(z^2 + d^2)(-1 + \Delta z)}}\end{aligned} \tag{A.3}$$

References

[1] B. Rudin, A. Rutz, M. Hoffmann, D. J. H. C. Maas, A.-R. Bellancourt, E. Gini, T. Südmeyer, and U. Keller, "Highly efficient optically pumped vertical-emitting semiconductor laser with more than 20 W average output power in a fundamental transverse mode," *Optics Letters*, vol. 33, p. 2719, nov 2008.

[2] O. G. Okhotnikov and Wiley InterScience (Online service), *Semiconductor disk lasers : physics and technology.* Wiley-VCH, 2010.

[3] L. Fan, M. Fallahi, A. R. Zakharian, J. Hader, J. V. Moloney, R. Bedford, J. T. Murray, W. Stolz, and S. W. Koch, "Extended Tunability in a Two-Chip VECSEL," *IEEE Photonics Technology Letters*, vol. 19, no. 8, pp. 544–546, 2007.

[4] T. D. Raymond, W. J. Alford, M. H. Crawford, and A. A. Allerman, "Intracavity frequency doubling of a diode-pumped external-cavity surface-emitting semiconductor laser," *Optics Letters*, vol. 24, p. 1127, aug 1999.

[5] U. Keller, D. A. B. Miller, G. D. Boyd, T. H. Chiu, J. F. Ferguson, and M. T. Asom, "Solid-state low-loss intracavity saturable absorber for Nd:YLF lasers: an antiresonant semiconductor FabryPerot saturable absorber," *Optics Letters*, vol. 17, p. 505, apr 1992.

[6] U. Keller, K. Weingarten, F. Kartner, D. Kopf, B. Braun, I. Jung, R. Fluck, C. Honninger, N. Matuschek, and J. Aus der Au, "Semiconductor saturable absorber mirrors (SESAM's) for femtosecond to nanosecond pulse generation in solid-state lasers," *IEEE Journal of Selected Topics in Quantum Electronics*, vol. 2, no. 3, pp. 435–453, 1996.

[7] T. Wunderer, J. E. Northrup, Z. Yang, M. Teepe, A. Strittmatter, N. M. Johnson, P. Rotella, and M. Wraback, “In-well pumping of InGaN/GaN vertical-external-cavity surface-emitting lasers,” *Applied Physics Letters*, vol. 99, p. 201109, nov 2011.

[8] M. Rahim, F. Felder, M. Fill, and H. Zogg, “Optically pumped 5 μm IV-VI VECSEL with Al-heat spreader,” *Optics Letters*, vol. 33, p. 3010, dec 2008.

[9] K. G. Wilcox, A. C. Tropper, H. E. Beere, D. A. Ritchie, B. Kunert, B. Heinen, and W. Stolz, “4.35 kW peak power femtosecond pulse mode-locked VECSEL for supercontinuum generation,” *Optics Express*, vol. 21, no. 2, pp. 1599–605, 2013.

[10] M. Scheller, T.-L. Wang, B. Kunert, and W. Stolz, “Passively modelocked VECSEL emitting 682 fs pulses with 5.1 W of average output power,” *Electronics letters*, vol. 48, no. 10, p. 588, 2012.

[11] B. Heinen, T.-L. Wang, M. Sparenberg, a. Weber, B. Kunert, J. Hader, S. Koch, J. Moloney, M. Koch, and W. Stolz, “106 W continuous-wave output power from vertical-external-cavity surface-emitting laser,” *Electronics Letters*, vol. 48, no. 9, p. 516, 2012.

[12] S. Hoogland, S. Dhanjal, A. C. Tropper, J. S. Roberts, R. Häring, R. Paschotta, F. Morier-Genoud, and U. Keller, “Passively mode-locked diode-pumped surface-emitting semiconductor laser,” *IEEE Photonics Technology Letters*, vol. 12, no. 9, pp. 1135–1137, 2000.

[13] D. J. H. C. Maas, A. R. Bellancourt, M. Hoffmann, B. Rudin, Y. Barbarin, M. Golling, T. Südmeyer, and U. Keller, “Growth parameter optimization for fast quantum dot SESAMs,” *Optics Express*, vol. 16, p. 18646, nov 2008.

[14] C. A. Zaugg, Z. Sun, D. Popa, S. Milana, T. Kulmala, R. S. Sundaram, V. J. Wittwer, M. Mangold, O. D. Sieber, M. Golling, Y. Lee, J.-H. Ahn, A. C. Ferrari, and U. Keller, “Wavelength Tunable Graphene Modelocked VECSEL,” in *CLEO: 2013*, (Washington, D.C.), p. CW1G.4, OSA, 2013.

[15] D. Maas, U. Keller, T. Südmeyer, A.-R. Bellancourt, M. Golling, and B. Rudin, "Modelocked integrated external-cavity surface emitting laser," *IET Optoelectronics*, vol. 3, pp. 61–72, apr 2009.

[16] Y. F. Chen, Y. C. Lee, H. C. Liang, K. Y. Lin, K. W. Su, and K. F. Huang, "Femtosecond high-power spontaneous mode-locked operation in vertical-external cavity surface-emitting laser with gigahertz oscillation," *Optics Letters*, vol. 36, no. 23, p. 4581, 2011.

[17] L. Kornaszewski, G. Maker, G. Malcolm, M. Butkus, E. Rafailov, and C. Hamilton, "SESAM-free mode-locked semiconductor disk laser," *Laser & Photonics Reviews*, vol. 6, pp. L20–L23, nov 2012.

[18] A. R. Albrecht, D. V. Seletskiy, Y. Wang, J. G. Cederberg, and M. Sheik-Bahae, "Exploring ultrafast negative Kerr Effect for self-mode-locking vertical external-cavity surface-emitting lasers," *SPIE Photonics West 2014-LASE: Lasers and Sources*, vol. 8966, p. 896604, nov 2014.

[19] M. Gaafar, P. Richter, and H. Keskin, "Self-mode-locking semiconductor disk laser," *Optics* {...}, vol. 22, pp. 28390–28399, nov 2014.

[20] L. Kornaszewski, G. Maker, G. Malcolm, M. Butkus, E. U. Rafailov, and C. Hamilton, "Reply to comment on SESAM-free mode-locked semiconductor disk laser," *Laser & Photonics Reviews*, vol. 7, pp. 555–556, jul 2013.

[21] H.-C. Liang, Y.-C. Lee, J.-C. Tung, K.-W. Su, K.-F. Huang, and Y.-F. Chen, "Exploring the spatio-temporal dynamics of an optically pumped semiconductor laser with intracavity second harmonic generation," *Optics Letters*, vol. 37, p. 4609, nov 2012.

[22] B. Heinen, M. Wichmann, M. Koch, W. Stolz, C. Möller, M. Gaafar, A. Rahimi-Iman, and B. Kunert, "Harmonic self-mode-locking of optically pumped semiconductor disc laser," *Electronics Letters*, vol. 50, pp. 542–543, mar 2014.

[23] M. Gaafar, D. A. Nakdali, C. Möller, K. A. Fedorova, M. Wichmann, M. K. Shakfa, F. Zhang, A. Rahimi-Iman, E. U. Rafailov, and M. Koch, "Self-mode-locked quantum-dot vertical-external-cavity surface-emitting laser.," *Optics letters*, vol. 39, pp. 4623–4626, aug 2014.

[24] J. V. Moloney, I. Kilen, and A. Bäumner, "Nonequilibrium and thermal effects in mode-locked VECSELs," *Optics* {…}, vol. 22, pp. 6422–6427, mar 2014.

[25] T. Brabec, C. Spielmann, P. F. Curley, and F. Krausz, "Kerr lens mode locking," *Optics Letters*, vol. 17, p. 1292, sep 1992.

[26] D. H. Sutter, G. Steinmeyer, L. Gallmann, N. Matuschek, F. Morier-Genoud, U. Keller, V. Scheuer, G. Angelow, and T. Tschudi, "Semiconductor saturable-absorber mirrorassisted Kerr-lens mode-locked Ti:sapphire laser producing pulses in the two-cycle regime," *Optics Letters*, vol. 24, p. 631, may 1999.

[27] U. Morgner, F. X. Kärtner, S. H. Cho, Y. Chen, H. A. Haus, J. G. Fujimoto, E. P. Ippen, V. Scheuer, G. Angelow, and T. Tschudi, "Sub-two-cycle pulses from a Kerr-lens mode-locked Ti:sapphire laser," *Optics Letters*, vol. 24, p. 411, mar 1999.

[28] A. E. Siegman, *Lasers.* University Science Books, 1986.

[29] C. J. Saraceno, F. Emaury, C. Schriber, M. Hoffmann, M. Golling, T. Südmeyer, and U. Keller, "Ultrafast thin-disk laser with 80μJ pulse energy and 242W of average power," *Optics Letters*, vol. 39, p. 9, jan 2014.

[30] M. Guina, A. Rantamäki, and A. Härkönen, "Optically pumped VECSELs: review of technology and progress," *Journal of Physics D: Applied Physics*, vol. 50, p. 383001, sep 2017.

[31] P. Klopp, U. Griebner, M. Zorn, and M. Weyers, "Pulse repetition rate up to 92 GHz or pulse duration shorter than 110 fs from a mode-locked semiconductor disk laser," *Applied Physics Letters*, vol. 98, no. 7, 2011.

[32] D. Waldburger, S. M. Link, M. Mangold, C. G. E. Alfieri, E. Gini, M. Golling, B. W. Tilma, and U. Keller, "High-power 100 fs semiconductor disk lasers,"

[33] M. Kuznetsov, F. Hakimi, R. Sprague, and a. Mooradian, "Design and Characteristics of High-Power (0 . 5-W Surface-Emitting Semiconductor Lasers with Circular TEM Beams," *IEEE Journal of Selected Topics in Quantum Electronics*, vol. 5, no. 3, pp. 561–573, 1999.

[34] C. Borgentun, J. Bengtsson, A. Larsson, F. Demaria, A. Hein, and P. Unger, "Optimization of a Broadband Gain Element for a Widely Tunable High-Power Semiconductor Disk Laser," *IEEE Photonics Technology Letters*, vol. 22, pp. 978–980, jul 2010.

[35] S. Hoogland, *Optically pumped vertical external cavity surface emitting semiconductor lasers.* Doctoral thesis, University of Southampton, 2003.

[36] A. Tropper and S. Hoogland, "Extended cavity surface-emitting semiconductor lasers," *Progress in Quantum Electronics*, vol. 30, pp. 1–43, jan 2006.

[37] C. Borgentun, J. Bengtsson, and A. Larsson, "Direct measurement of the spectral reflectance of OP-SDL gain elements under optical pumping.," *Optics express*, vol. 19, no. 18, pp. 16890–7, 2011.

[38] A. Gosteva, M. Haiml, R. Paschotta, and U. Keller, "Noise-related resolution limit of dispersion measurements with white-light interferometers," *Journal of the Optical Society of America B*, vol. 22, p. 1868, sep 2005.

[39] D. J. H. C. Maas, B. Rudin, a. R. Bellancourt, D. Iwaniuk, T. Südmeyer, and U. Keller, "High precision optical characterization of semiconductor saturable absorber mirrors (SESAMs)," *2008 Conference on Quantum Electronics and Laser Science Conference on Lasers and Electro-Optics, CLEO/QELS*, vol. 16, no. 10, pp. 16966–16971, 2008.

[40] M. Mangold, V. J. Wittwer, O. D. Sieber, M. Hoffmann, I. L. Krestnikov, D. A. Livshits, M. Golling, T. Südmeyer, and U. Keller, "VECSEL gain characterization," *Optics Express*, vol. 20, p. 4136, feb 2012.

[41] O. Sieber, M. Hoffmann, and V. Wittwer, "Experimentally verified pulse formation model for high-power femtosecond VECSELs," *Applied Physics B*, vol. 113, pp. 133–145, apr 2013.

[42] C. N. Böttge, J. Hader, I. Kilen, J. V. Moloney, and S. W. Koch, "Ultrafast pulse amplification in mode-locked vertical external-cavity surface-emitting lasers," *Applied Physics Letters*, vol. 105, p. 261105, dec 2014.

[43] R. Fleischhaker, N. Krauß, F. Schättiger, and T. Dekorsy, "Consistent characterization of semiconductor saturable absorber mirrors with single-pulse and pump-probe spectroscopy," *Optics Express*, vol. 21, p. 6764, mar 2013.

[44] C. Baker, M. Scheller, S. W. Koch, A. R. Perez, W. Stolz, R. Jason Jones, and J. V. Moloney, "In situ probing of mode-locked vertical-external-cavity-surface-emitting lasers," *Optics Letters*, vol. 40, no. 23, p. 5459, 2015.

[45] A. Yariv and P. Yeh, *Optical waves in crystals : propagation and control of laser radiation.* John Wiley and Sons, 2003.

[46] M. Sheik-Bahae, A. Said, T.-H. Wei, D. Hagan, and E. W. Van Stryland, "Sensitive measurement of optical nonlinearities using a single beam," *IEEE Journal of Quantum Electronics*, vol. 26, no. 4, pp. 760–769, 1990.

[47] L. Palfalvi, B. C. Toth, G. Almasi, J. A. Fulop, and J. Hebling, "A general Z-scan theory," in *CLEO/Europe - EQEC 2009 - European Conference on Lasers and Electro-Optics and the European Quantum Electronics Conference*, pp. 1–1, IEEE, jun 2009.

[48] A. Major, F. Yoshino, I. Nikolakakos, J. S. Aitchison, and P. W. E. Smith, "Dispersion of the nonlinear refractive index in sapphire," *Optics Letters*, vol. 29, p. 602, mar 2004.

[49] M. Martinelli, L. Gomes, and R. J. Horowicz, "Measurement of Refractive Nonlinearities in GaAs Above Bandgap Energy," *Applied Optics*, vol. 39, p. 6193, nov 2000.

[50] C. T. Hultgren and E. P. Ippen, "Ultrafast refractive index dynamics in AlGaAs diode laser amplifiers," *Applied Physics Letters*, vol. 59, p. 635, aug 1991.

[51] K. L. Hall, A. M. Darwish, E. P. Ippen, U. Koren, and G. Raybon, "Femtosecond index nonlinearities in InGaAsP optical amplifiers," *Applied Physics Letters*, vol. 62, p. 1320, mar 1993.

[52] M. Sheik-Bahae, D. Hutchings, D. Hagan, and E. Van Stryland, "Dispersion of bound electron nonlinear refraction in solids," *IEEE Journal of Quantum Electronics*, vol. 27, pp. 1296–1309, jun 1991.

[53] A. H. Quarterman, M. A. Tyrk, and K. G. Wilcox, "Z-scan measurements of the nonlinear refractive index of a pumped semiconductor disk laser gain medium," *Applied Physics Letters*, vol. 106, p. 11105, jan 2015.

[54] E. A. Shaw, A. H. Quarterman, L. E. Hooper, P. J. Mosley, and K. G. Wilcox, "Coherent spectral broadening and compression of the output of a mode-locked VECSEL," p. 93490R, International Society for Optics and Photonics, mar 2015.

[55] E. W. V. Stryland and M. Sheik-Bahae, "Z-Scan Measurements of Optical Nonlinearities," *Characterization Techniques and Tabulations for Organic Nonlinear Materials*, no. 3, pp. 655–692, 1998.

[56] A. R. Albrecht, Y. Wang, M. Ghasemkhani, D. V. Seletskiy, J. G. Cederberg, and M. Sheik-Bahae, "Exploring ultrafast negative Kerr effect for mode-locking vertical external-cavity surface-emitting lasers.," *Optics express*, vol. 21, pp. 28801–8, nov 2013.

[57] M. J. LaGasse, K. K. Anderson, C. A. Wang, H. A. Haus, and J. G. Fujimoto, "Femtosecond measurements of the nonresonant nonlinear index in AlGaAs," *Applied Physics Letters*, vol. 56, p. 417, jan 1990.

[58] M. Sheik-Bahae and E. W. Van Stryland, "Ultrafast nonlinearities in semiconductor laser amplifiers," *Physical Review B*, vol. 50, pp. 14171–14178, nov 1994.

[59] I. Kumar and A. Khare, "Modified Z-scan set-up using CCD for measurement of optical nonlinearity in PLD carbon thin film," *Optics and Laser Technology*, vol. 77, pp. 51–54, 2016.

[60] R. Paschotta, R. Häring, A. Garnache, S. Hoogland, A. Tropper, and U. Keller, "Soliton-like pulse-shaping mechanism in passively mode-locked surface-emitting semiconductor lasers," *Applied Physics B: Lasers and Optics*, vol. 75, pp. 445–451, oct 2002.

[61] R. Paschotta, "Noise of mode-locked lasers (Part I): numerical model," *Applied Physics B*, vol. 79, pp. 153–162, jul 2004.

[62] J. Hader, G. Hardesty, Tsuei-Lian Wang, M. Yarborough, Y. Kaneda, J. Moloney, B. Kunert, W. Stolz, and S. Koch, "Predictive Microscopic Modeling of VECSELs," *IEEE Journal of Quantum Electronics*, vol. 46, pp. 810–817, may 2010.

[63] I. Kilen, S. W. Koch, J. Hader, and J. V. Moloney, "Non-equilibrium ultrashort pulse generation strategies in VECSELs," *Optica*, vol. 4, p. 412, apr 2017.

[64] H. Haus, "Mode-locking of lasers," *IEEE Journal of Selected Topics in Quantum Electronics*, vol. 6, pp. 1173–1185, nov 2000.

[65] M. Mangold, V. J. Wittwer, O. D. Sieber, M. Hoffmann, I. L. Krestnikov, D. A. Livshits, M. Golling, T. Südmeyer, and U. Keller, "VECSEL gain characterization.," *Optics express*, vol. 20, pp. 4136–48, feb 2012.

[66] G. Herink, B. Jalali, C. Ropers, and D. R. Solli, "Resolving the build-up of femtosecond mode-locking with single-shot spectroscopy at 90 MHz frame rate," 2016.

[67] A. P. Turnbull, C. R. Head, E. A. Shaw, T. Chen-Sverre, and A. C. Tropper, "Spectrally resolved pulse evolution in a mode-locked vertical-external-cavity surface-emitting laser from lasing onset measurements," p. 93490I, International Society for Optics and Photonics, mar 2015.